UiO : University of Oslo

Stian Thomas Heimdal Hartman

Cosmology of Scalar Field Dark Matter with Self-Interactions

Thesis submitted for the degree of Philosophiae Doctor

Institute of Theoretical Astrophysics
Faculty of Mathematics and Natural Sciences

2022

Series of dissertations submitted to the
Faculty of Mathematics and Natural Sciences, University of Oslo
No. 2539

ISSN 1501-7710

Cover: Hanne Baadsgaard Utigard.
Print production: Graphics Center, University of Oslo.

To Lyra, my lockdown buddy

Preface

This thesis is submitted in partial fulfillment of the requirements for the degree of *Philosophiae Doctor* at the University of Oslo. The research presented here was conducted at the Institute of Theoretical Astrophysics (ITA) under the supervision of professor David F. Mota and associate professor Hans A. Winther. This thesis represents an effort to further our understanding of self-interacting scalar field models of dark matter. There exists a multitude of realizations for this kind of dark matter, most of which propose to explain observations that are not yet fully accounted for in the standard model of our universe. In this work we have investigated some of the unique aspects of these models in order to better understand how they impact the formation of structure in our universe, as well as how observational probes that can be used to constrain the model parameters are affected.

In Chapter 1 we review the basic theoretical framework of the standard cosmological model, from the smooth and homogeneous background universe, to the initial tiny deviations described by linear perturbation theory, and finally the non-linear structures that we observe today that require large-scale cosmological simulations to study. We also briefly review the timeline of the universe, as well as some of the open questions in this standard model of the universe.

In Chapter 2 we go through the basic theory and phenomenology of ultra-light scalar fields in cosmology, and how they might help explain observations that are not fully understood within the standard model.

In Chapter 3 we provide brief summaries of the four papers produced during this PhD and their main findings.

Acknowledgements

I would like to express my sincere gratitude to my supervisors, David Mota and Hans Winther. They let me explore topics I found exciting while providing invaluable guidance and support. I am eternally grateful for the opportunity they gave me in pursuing a PhD at ITA, and for their part in my scientific education. Thank you for everything, David and Hans!

I am also grateful to the IT department at ITA for keeping the institute computers running smoothly, as well as for their patience with me when I mercilessly crashed these with my simulations.

I would like to give a shout out to my office mates throughout my years at ITA; Robert, Mattia, Renate, Sladana, Isabel, and Tim—thanks for the great company!

Finally, I would like to thank my family and my amazing wife for their continual love and support. I love you all!

Stian Thomas Heimdal Hartman
Oslo, July 2022

List of Papers

Paper I

Stian T. H. Hartman, Hans A. Winther, and David F. Mota "Collapse of spherical overdensities in superfluid models of dark matter". In: *Astronomy and Astrophysics*, July 2020, vol. 639, A90. DOI: 10.1051/0004-6361/201937263. arXiv: 1911.11498.

Paper II

Stian T. H. Hartman, Hans A. Winther, and David F. Mota "Dynamical friction in Bose-Einstein condensed self-interacting dark matter at finite temperatures, and the Fornax dwarf spheroidal". In: *Astronomy & Astrophysics*, March 2021, vol. 647, A70. DOI: 10.1051/0004-6361/202039865. arXiv: 2011.00116.

Paper III

Stian T. H. Hartman, Hans A. Winther, and David F. Mota "Constraints on self-interacting Bose-Einstein condensate dark matter using large-scale observables". In: *Journal of Cosmology and Astroparticle Physics*, February 2022, vol. 2022, 2. DOI: 10.1088/1475-7516/2022/02/005. arXiv: 2108.07496.

Paper IV

Stian T. H. Hartman, Hans A. Winther, and David F. Mota "Cosmological simulations of self-interacting Bose-Einstein condensate dark matter". Submitted for publication in: *Astronomy & Astrophysics*. arXiv: 2203.03946.

Contents

List of Figures

Chapter 1

The Standard Model of the Universe

1.1 Introduction

The cosmos is a place of wonder and mystery that has fueled the human imagination for millennia. We have since the dawn of our specie populated the star-speckled void with stories of gods and monsters, great triumphs and tragedies, in an effort to understand our physical world. There was a time when it was believed the sun rose in the east and set in the west because a great being carried it across the sky. In Greek mythology it was Helios who rode above the horizon with the sun harnessed to his chariot, while in Norse and Vedic lore it was Sól and Surya. The stories did not just extend to the machinations of the heavens. The Greeks also believed the Earth became cold and barren in winter because the Olympian god Demeter refused to let anything grow and flourish during the months her daughter Persephone was forced to return to Hades in the underworld each year. In Japanese mythology, the tides were controlled by the dragon god Ryūjin through the use of magical gems. But as time passed these stories were replaced with another kind of myth. One of mathematics and physical laws, which has proven successful in explaining nearly every facet of our world. We now know that the sun rises and sets on the horizon, and that the seasons change, because of the tilted rotation of the Earth and its orbit around the Sun. We also know that the ebb and flow of the tides are due to the gravitational pull of the moon—not the divine influence of magic jewelry. Equipped with the principles and tools of physics and mathematics, mankind has returned it gaze towards the skies, beyond the Solar system, even our own Milky Way, to the largest structures of the universe, in order to further understand our physical world—the realm of *cosmology*.

1.2 A Short History of Cosmology

Cosmology is, broadly speaking, the study of the matter and energy content of our universe and the structures that form in it. Gravity is the dominant force on the scales relevant for cosmology, since the other fundamental forces of nature are either too short ranged (the weak and

strong force), or the universe has zero net charge associated with the force (electromagnetism). For over 200 years the accepted theory of celestial motion was Newton's universal law of gravitation, which he formulated in 1687 [94]. Within Newton's framework the universe was static and eternal, forever unchanging in the grand scheme of things. It was not until Einstein proposed his general theory of relativity in 1915 [39, 38], providing the theoretical foundation for describing gravity in a way consistent with relativity, that it was realized the universe is far from unchanging.

In Einstein's theory of General Relativity (GR), gravity is not a force, but motion along geodesics in a 4-dimensional spacetime that is curved by matter and energy. In systems like the Solar system, or even galaxies, the geodesics that planets and stars trace through spacetime are nearly indistinguishable from those predicted by Newton's inverse square law. On scales much larger than galaxies, on the other hand, the universe starts to deviate from the Newtonian paradigm. Edwin Hubble discovered in 1929 that the recessional velocity v of galaxies increases with their distance d from us [59];

$$v = H_0 d, \tag{1.1}$$

where the parameter $H_0 \approx 70 \mathrm{kms}^{-1}\mathrm{Mpc}^{-1}$ is known as Hubble's constant, and quantifies the observed increase in the recessional velocity with distance. This constant is also often written as $H_0 = 100h\,\mathrm{kms}^{-1}\mathrm{Mpc}^{-1}$, where $h \approx 0.7$. Newtonian cosmology fails to provide a satisfactory explanation for this observation, but GR provides an elegant solution; that the overall fabric of spacetime of our universe is expanding. Distant galaxies appear to be moving away from us at increasing velocities because the intervening space is continually being filled with more space.

Hubble's discovery of cosmic expansion had several far-reaching consequences for our understanding of the past history of the universe. Since the universe is currently expanding, it stands to reason that the universe used to be smaller, and therefore denser and hotter. So much so, in fact, that in the distant past everything we see around us was part of a nearly formless primordial plasma. Only when the universe became sufficiently cold and diluted did structures like galaxies, stars, and planets form. If we extrapolate the expansion far enough back in time, the universe might have sprung into existence from a seemingly infinitely small and dense state—a singularity. Such a universe can, for all intents and purposes, be considered to have existed for a finite time, currently estimated to 13.8 billion years. This scenario is called the *Big Bang*, and an incredible achievement of astronomy is the confirmation of

a number of predictions of Big Bang theory, such as the relic abundances of nuclear elements produced in the first few minutes of the universe, known as Big Bang Nucleosythesis (BBN), and the afterglow of the primordial plasma when photons and baryons decoupled as electrons and protons recombined into neutral hydrogen, which left a faint imprint of the universe on the sky of when it was just 380,000 years old.[1] This signal is the cosmic microwave background radiation (CMB), and was first observed as a constant background temperature of around 3K in 1965 by Arno Penzias and Robert Wilson [102], who were awarded the 1978 Nobel prize in physics for their discovery. The CMB has since been measured with incredible precision [130, 132, 73, 6, 27, 140, 19, 133], as shown in figure 1.1, and found to be a nearly perfect blackbody radiation at 2.7K with tiny anisotropies—the imprint of the initial inhomogeneities that gave rise to all cosmic structures we see today. The near homogeneity of the CMB, and the nearly scale-invariant spectrum of perturbations in it, has provided strong support for inflationary theory—that the universe underwent an initial period of extreme and accelerated expansion, bringing tiny quantum fluctuations into the classical realm which became the initial conditions for our universe.

It eventually became clear that GR and the observed matter in our universe is not enough to provide a consistent picture of the cosmos. In 1998, studies of supernova distances and redshifts showed that the universe is not just expanding, but it is doing so at an accelerated pace [112, 103]. No known substance can cause such accelerated expansion—all standard matter is gravitationally attractive—which means there must exist an additional unknown component in our universe that is somehow gravitationally *repulsive*, present even in the seemingly empty regions between galaxies and clusters of galaxies. There exists many hypothetical realizations for this so-called dark energy (DE), including vacuum energy, modified gravity, or a cosmological constant.

Observations have for nearly a century hinted at the existence of a second unseen component in our universe. In the 1930s Jan Oort and Fritz Zwicky observed that galaxies in galaxy clusters are moving too fast to be consistent with the observed matter and virial equilibrium [152, 153]. Vera Rubin and Kent Ford made similar observations in the 1970s in the rotation curves of galaxies: The circular velocities of stars and gas clouds are much too fast to be orbiting just the visible mass inside the galaxies [116]. It became clear that a large amount of matter is missing in order for galaxies and galaxy clusters to be gravitationally bound,

[1] The term "recombination" for when electrons and protons formed neutral atoms is a bit of a misnomer, since it is seemingly the first time stable neutral hydrogen existed in our universe.

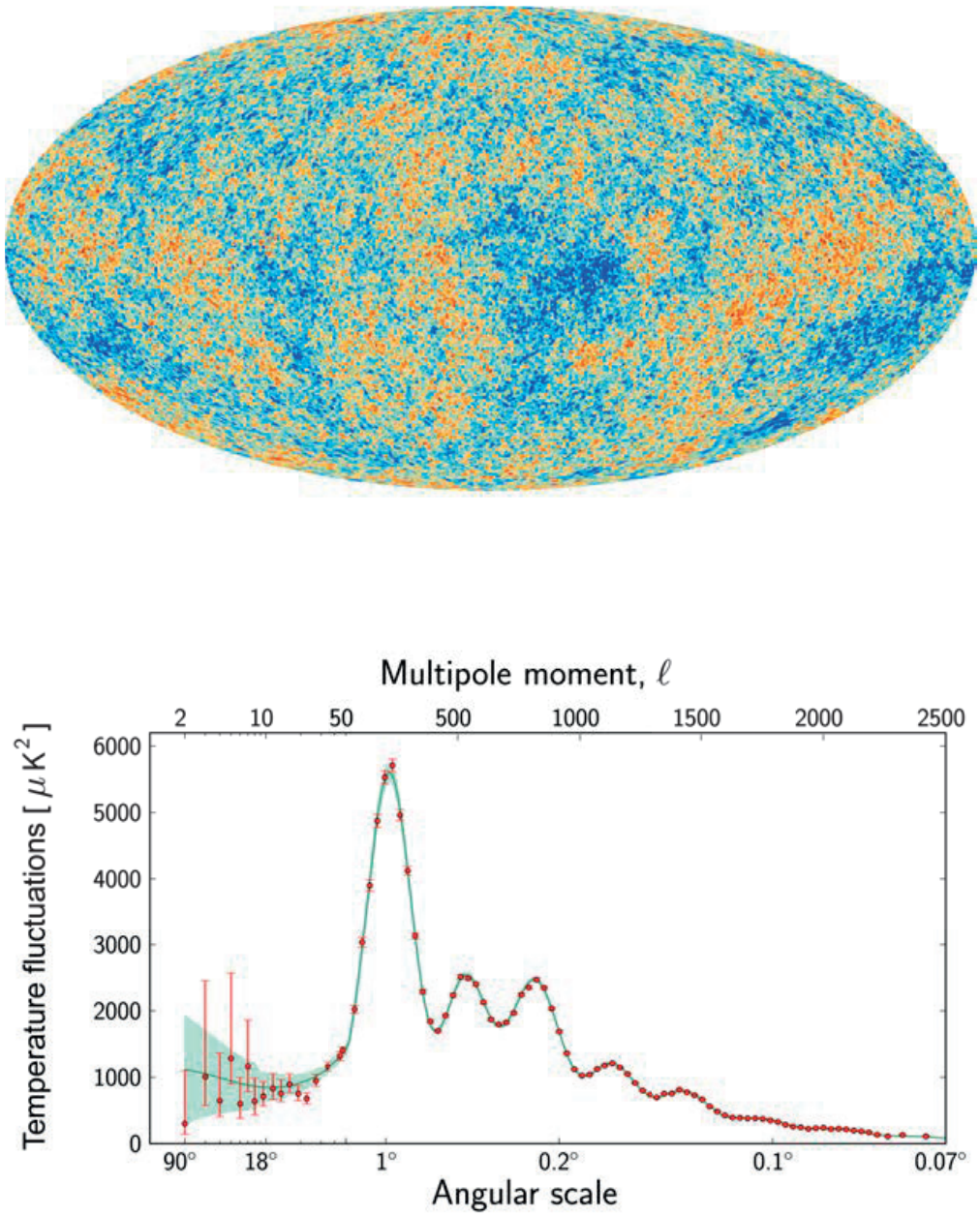

Figure 1.1: The CMB signal (*upper*) as seen by the Planck satellite after removing foreground signals and subtracting the dipole, and (*lower*) the power spectrum of the temperature fluctuations from (*red dots*) observations compared against (*green line*) the theoretical spectrum and (*shaded green*) cosmic variance. The temperature fluctuations are the imprint of the universe in the moments before it became transparent to photons during recombination, and are of order $\pm 200\mu$K, compared to the CMB mean blackbody temperature of 2.7K. Credit: ESA, Planck Collaboration.

otherwise they would break apart due to the large orbital velocities. It was initially thought this missing *dark matter* (DM) could be hidden baryonic matter, such as cool stars, gases, and solid bodies, but BBN and the CMB tells us this is not the case. For instance, the rate of nuclear reactions during BBN depend strongly on the baryon density, and the relic abundances of light elements are consistent with only a small amount of baryonic matter [139]. Furthermore, the anisotropies of the CMB are too small to seed the structures we see in the universe today. Simply put, not enough time has passed for the perturbations observed in the CMB to grow into galaxies if all of matter is baryonic. If, on the other hand, DM was cold and decoupled from the hot photon-baryon plasma, it could have begun clustering earlier, creating potential wells for baryons to fall into after recombination, hence speeding up the growth of visible structures. There are further features in the CMB that indicate the existence of a cold DM (CDM) component decoupled from visible matter, such as the relative height of the acoustic peaks and their characteristic scale on the sky. Additionally, weak lensing measurements of colliding clusters show that the majority of the mass is offset from the visible gas and stars [55], the most famous example of this being the Bullet Cluster shown in figure 1.2, providing further strong evidence for a dark and as-of-yet unidentified matter component in our universe.

Although little is known about DM and DE, a cold and collisionless DM component (i.e. CDM), and a cosmological constant (Λ) for DE, combined with GR and the standard model of particle physics, provides a very successful model for describing the universe we live in. This standard model for cosmology is called the ΛCDM model, named so after its two largest unknowns that make up around 95% of the cosmic energy content today. In the next few sections we will review the basic concepts of cosmology and ΛCDM before taking a closer look at the topic of this thesis—exploring light scalar field models of DM beyond CDM.

1.3 General Relativity

An action is often considered the most fundamental object for the dynamical behaviour of a system, which in GR is the *Einstein–Hilbert* action [56];

$$\mathcal{S} = \int \left[\frac{1}{16\pi G}(R - 2\Lambda) + \mathcal{L}_m \right] \sqrt{-g}\, \mathrm{d}^4x. \tag{1.2}$$

This describes a universe with; a spacetime metric $g_{\mu\nu}$, which has a determinant $g = \det(g_{\mu\nu})$ and a local curvature given by the Ricci scalar R; a cosmological constant Λ; and matter, which is encoded in the matter

Figure 1.2: A composite image of a pair of galaxy clusters that have collided head on, known as the Bullet Cluster. Galaxies are seen in the optical as orange and white, while the hot intracluster gas as seen in X-ray is shown in pink. The mass distribution in the cluster is shown in blue, obtained from the distortion of the background galaxies due to gravitational lensing. The Bullet Cluster reveals that the majority of the mass is not in the visible stars or gas, but in the form of an unknown form of cold and collisionless matter, i.e. dark matter. Credit: X-ray: NASA/CXC/CfA/M.Markevitch et al.; Optical: NASA/STScI; Magellan/U.Arizona/D.Clowe et al.; Lensing Map: NASA/STScI; ESO WFI; Magellan/U.Arizona/D.Clowe et al.

Lagrangian $\mathcal{L}_m$. In GR, the metric tensor—the very fabric of space and time—is dynamical, and variation of the action $\delta\mathcal{S} = 0$ with respect to $g_{\mu\nu}$ gives the Einstein field equations;

$$R_{\mu\nu} - \frac{1}{2}g_{\mu\nu}R = 8\pi G T_{\mu\nu} - \Lambda g_{\mu\nu}. \tag{1.3}$$

The Einstein field equations form a set of 10 coupled non-linear differential equations for the 10 independent components of the symmetric metric tensor $g_{\mu\nu}$, and describe how spacetime is curved by matter and energy, given by energy-momentum tensor,

$$T_{\mu\nu} = -2\frac{\delta\mathcal{L}_m}{\delta g^{\mu\nu}} + g_{\mu\nu}\mathcal{L}_m. \tag{1.4}$$

For a perfect fluid the energy-momentum tensor assumes the simple form

$$T_{\mu\nu} = (\rho + P)u_\mu u_\nu + P g_{\mu\nu}, \tag{1.5}$$

where ρ is the energy density, P the pressure, and $u^\mu = \mathrm{d}x^\mu/\mathrm{d}\tau$ the four-velocity of the fluid. The Ricci curvature tensor $R_{\mu\nu}$ provides a measure of the curvature of the spacetime manifold, and is the contraction $R_{\mu\nu} = R^\alpha{}_{\mu\alpha\nu}$ of the Riemann tensor,

$$R^\mu{}_{\nu\rho\sigma} = \frac{\partial\Gamma^\mu_{\nu\sigma}}{\partial x^\rho} - \frac{\partial\Gamma^\mu_{\nu\rho}}{\partial x^\sigma} + \Gamma^\mu_{\eta\rho}\Gamma^\eta_{\nu\sigma} - \Gamma^\mu_{\eta\sigma}\Gamma^\eta_{\nu\rho}, \tag{1.6}$$

where the Christoffel symbols $\Gamma^\mu_{\alpha\beta}$ are given by

$$\Gamma^\mu_{\alpha\beta} = \frac{1}{2}g^{\mu\rho}\left(\frac{\partial g_{\beta\rho}}{\partial x^\alpha} + \frac{\partial g_{\alpha\rho}}{\partial x^\beta} - \frac{\partial g_{\alpha\beta}}{\partial x^\rho}\right), \tag{1.7}$$

while the Ricci scalar is the contraction of the Ricci curvature tensor, $R = R^\mu{}_\mu$.

The Einstein field equations are only one side of a geometric theory of gravitation. We also need to know how particles move through curved spacetime. The equations of motion can once again be derived from the variation of an action. This time, the action is the length of the curve through spacetime

$$\mathcal{I} = \int \mathrm{d}s, \tag{1.8}$$

where $\mathrm{d}s = \sqrt{-g_{\mu\nu}\mathrm{d}x^\mu\mathrm{d}x^\nu}$ is the line-element. We define an affine parameter λ that parameterizes the curve, $x^\mu(\lambda)$, such that

$$I = \int \mathrm{d}s = \int \sqrt{-g_{\mu\nu}\frac{\mathrm{d}x^\mu}{\mathrm{d}\lambda}\frac{\mathrm{d}x^\nu}{\mathrm{d}\lambda}}\mathrm{d}\lambda. \tag{1.9}$$

The variation $\delta\mathcal{I} = 0$ with respect to λ gives the "straight path" through curved spacetime, i.e. the geodesic, as

$$\frac{\mathrm{d}^2 x^\mu}{\mathrm{d}\tau^2} + \Gamma^\mu_{\alpha\beta}\frac{\mathrm{d}x^\alpha}{\mathrm{d}\tau}\frac{\mathrm{d}x^\beta}{\mathrm{d}\tau} = 0. \tag{1.10}$$

where we have used the proper time τ as the affine parameter. The motion of free-falling bodies in GR is therefore encoded in the Christoffel symbols, quantifying the curvature of the local spacetime in a particular choice of coordinates.

1.4 The Smooth Universe

An important assumption in physical cosmology is the Copernican principle, which states there is nothing singular about our position in the universe. Furthermore, the universe appears to be isotropic, i.e. on sufficiently large scales it looks the same in all directions, which combined with the Copernican principle implies the universe is homogeneous. As a result, the matter and energy content of the universe, as well as the metric tensor, is only dependent on time on very large scales. Observations indicate that our universe does not have an overall curvature, so lets consider the line-element of a homogeneous universe, given by the Friedmann-Robertson-Walker (FRW) metric, in the spatially flat case;

$$\mathrm{d}s^2 = -\mathrm{d}t^2 + a^2 \mathrm{d}r^i \mathrm{d}r^i. \tag{1.11}$$

Here, the Cartesian coordinates r^i are *comoving* coordinates, which are defined such that an object at rest with respect to the homogeneous average background has fixed comoving coordinates. The physical *proper* coordinates x^i are related to the comoving ones by $x^i = ar^i$, where a is the scale factor. All time dependence of the line-element is assumed to be encoded in a, and the solutions of the Einstein field equations in such a flat and homogeneous universe are

$$H^2 = \left(\frac{1}{a}\frac{\mathrm{d}a}{\mathrm{d}t}\right)^2 = \frac{8\pi G}{3}\bar{\rho}, \tag{1.12}$$

$$\frac{1}{a}\frac{\mathrm{d}^2 a}{\mathrm{d}t^2} = -\frac{4\pi G}{3}(\bar{\rho} + 3\bar{P}), \tag{1.13}$$

where $\bar{\rho}$ and $\bar{P}$ are the total energy density and pressure of the homogeneous background. These are known as the Friedmann equations [44, 45], and describe the expansion of the universe, though we will usually refer to eq. (1.12) as *the* Friedmann equation. H is the Hubble

parameter, and gives the relative expansion rate of the universe. It is easy now to see how Hubble's law is a consequence of cosmic expansion;

$$v = \frac{\mathrm{d}x}{\mathrm{d}t} = \frac{\mathrm{d}(ar)}{\mathrm{d}t} = \frac{\mathrm{d}a}{\mathrm{d}t}r = H_0 x, \tag{1.14}$$

where Hubble's constant is just the Hubble parameter at the present time. The recessional velocities of distant galaxies can be interpreted as not actually *moving* away from us in the usual sense, but instead that the intervening space is continually expanding. The observed redshift of a distant receding object can therefore be regarded as not being due to the Doppler effect, but the influence of expansion on the light emitted by the object as it propagates through the universe. As the universe expands and stretches, the electromagnetic radiation moving through it is stretched as well. A wave of light emitted with wavelength λ_e at a time t_e when the scale factor was a_e, will at a later time t_o when $a(t_o) = a_o > a_e$ be observed to have a wavelength λ_o of

$$\lambda_o = \lambda_e \frac{a_0}{a_e} > \lambda_e. \tag{1.15}$$

The light has therefore been *redshifted* in the time between being emitted and observed, and, given a specific cosmology, a number of things can be characterized by the amount of cosmic redshift we observe in an object, such as its distance from us, the time that has passed since the light was emitted, and the amount of cosmic expansion during that time. It is therefore very useful to define a measure of cosmic redshift, given by the relative change in the observed wavelength due to cosmic expansion;

$$z = \frac{\lambda_o - \lambda_e}{\lambda_e} = \frac{a_o}{a_e} - 1. \tag{1.16}$$

For context, our closest galactic neighbor, the Andromeda galaxy, is at $z \approx 2 \times 10^{-4}$ [110], although its observed redshift is actually $z \approx -10^{-3}$, i.e. blueshifted, because it is moving towards us. The most distant galaxy observed to date is GN-z11 at redshift $z = 11.02$ [97], and recombination and the formation of the CMB happened at $z \approx 1100$ [27], i.e. when the universe was around a thousand times smaller than it is today. While we cannot observe BBN directly, since all the light from that era has been absorbed and re-scattered before reaching us, we can still specify at which redshift we would have observed that light, which is $z \sim 10^9$ [139].

As the universe changes with time, so does the matter and energy in it. Their evolution is described by local conservation laws, which in GR are given by the covariant derivative of the energy-momentum tensor;

$$\nabla_\mu T^{\mu\nu} = \partial_\mu T^{\mu\nu} + \Gamma^\mu_{\mu\alpha} T^{\alpha\nu} + \Gamma^\nu_{\mu\alpha} T^{\mu\alpha} = 0. \tag{1.17}$$

For a perfect fluid at the homogeneous level, or the *background* level of universe, we simply get

$$\frac{\mathrm{d}\bar{\rho}}{\mathrm{d}a} = -3\frac{\bar{\rho}+\bar{P}}{a} = -3\bar{\rho}\frac{1+\omega}{a}, \tag{1.18}$$

where we have defined the equation of state $\omega = \bar{P}/\bar{\rho}$. This equation is also valid for the individual components of the universe that satisfy eq. (1.17) at the background level separately. If, for instance, two or more components were coupled in such a way that energy is transferred between them, then eq. (1.17) would contain extra source terms that would modify eq. (1.18), making the evolution of these components codependent. For the most part, however, the principle components of our universe do not appear to have such interactions. The background evolution can now be derived for the various forms of energy. Nearly pressureless matter, also referred to as dust, has $\omega \approx 0$, and therefore evolves as

$$\bar{\rho}_m = \bar{\rho}_{m0}a^{-3}, \tag{1.19}$$

where subscripts "0" indicate the value today. This is readily interpreted as the rest energy of a conserved number of particles becoming diluted as the universe expands. Relativistic matter and radiation, on the other hand, are dominated by their relativistic kinetic energy and have $\omega = 1/3$, hence

$$\bar{\rho}_r = \bar{\rho}_{r0}a^{-4}. \tag{1.20}$$

This can be understood as the decrease in energy density due to both the a^{-3} decrease in particle density, as well as a reduction in the relativistic energy of the particles, which is inversely proportional to their wavelength, contributing with an extra factor of a^{-1}.

According to eq. (1.18), the cosmological constant, when interpreted as a constant form of energy $\bar{\rho}_\Lambda = \Lambda/8\pi G$ on the right hand side of eq. (1.3), must have a constant negative pressure $\bar{P}_\Lambda = -\bar{\rho}_\Lambda$.

By inserting the equations for matter, radiation, and DE into the Friedmann equation, the evolution of the scale factor, and hence the expansion history of the universe, can derived. It is advantageous to define the fractional contributions to the critical energy density ρ_c of the universe of the various components,

$$\Omega_i = \frac{\bar{\rho}_i}{\rho_c}, \tag{1.21}$$

where

$$\rho_c = \frac{3H^2}{8\pi G}. \tag{1.22}$$

It is called the critical density because it is exactly the energy density needed for the universe to be flat, and therefore also corresponds to the total energy in our case, $\rho_c = \bar{\rho}_m + \bar{\rho}_r + \bar{\rho}_\Lambda$. With these definitions, the first Friedmann equation becomes

$$H^2 = H_0^2 \left[\Omega_{\mathrm{m}0} a^{-3} + \Omega_{\mathrm{r}0} a^{-4} + \Omega_{\Lambda 0}\right]. \tag{1.23}$$

Because the different forms of energy depend on the scale factor in different ways, they will each have dominated the total energy and expansion history at different epochs: First radiation dominated the total energy, followed by matter, until finally DE, as shown in figure 1.3. The scale factor in these different epoch evolve as

$$\begin{aligned} a(t) &\sim t^{1/2} \quad \text{during radiation-domination,} \\ a(t) &\sim t^{2/3} \quad \text{during matter-domination,} \\ a(t) &\sim e^{H_0\sqrt{\Omega_\Lambda}t} \quad \text{during DE-domination,} \end{aligned} \tag{1.24}$$

where the universe is decelerating during both radiation-and matter-domination, but is expanding at an exponentially accelerated rate during DE-domination. These three components form the backbone of the ΛCDM model, where the matter part includes both visible baryonic matter and CDM, $\Omega_{\mathrm{m}0} = \Omega_{\mathrm{b}0} + \Omega_{\mathrm{dm}0}$, while photons and relativistic neutrinos make up the radiation, $\Omega_{\mathrm{r}0} = \Omega_{\gamma 0} + \Omega_{\nu 0}$. The energy fractions today are constrained by observations, with [1]

$$\begin{aligned} \Omega_{\mathrm{dm}0} &= 0.26, \\ \Omega_{\mathrm{b}0} &= 0.049, \\ \Omega_{\Lambda 0} &= 0.69, \\ \Omega_{\gamma 0} &= 5.5 \times 10^{-5}, \\ \Omega_{\nu 0} &= 3.7 \times 10^{-5}. \end{aligned} \tag{1.25}$$

1.5 The Perturbed Universe

There is much more to the universe than just matter and energy. There is also structure, without which the cosmos would have been a very dull place. In the early universe, however, the seeds for all this structure were just tiny deviations from an otherwise nearly perfectly homogeneous cosmic soup. We can therefore use perturbation theory to accurately describe the growth of structure for a large portion of cosmic history. This generally requires the full machinery of Einstein's field equations and the Boltzmann equation for each particle component in order to

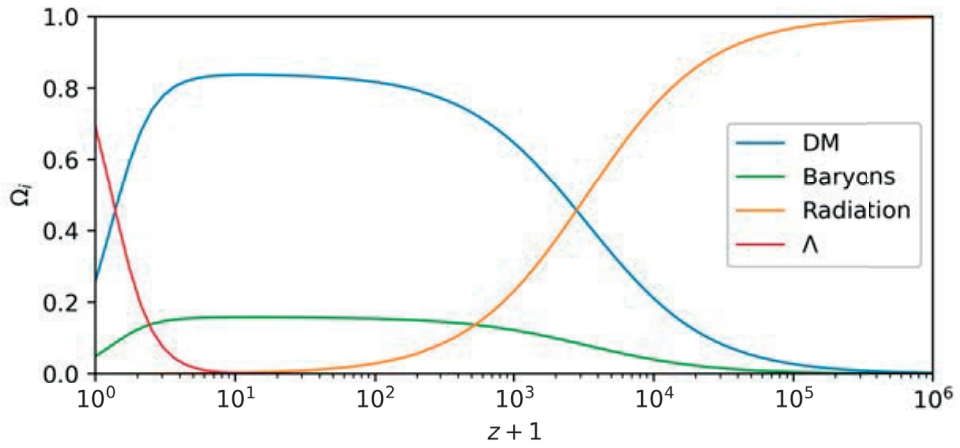

Figure 1.3: The composition of the cosmic energy budget through time, given by the energy fractions Ω_i for DM, baryons, total radiation, and a cosmological constant Λ, as functions of cosmic redshift z.

calculate e.g. the theoretical CMB temperature and polarization power spectra [72]. For the purposes of this discussion, which mainly focuses on the growth of matter inside the horizon, we will come a long way using a Newtonian fluid approximation.

The starting point in the Newtonian approximation are the hydrodynamic equations for the non-relativistic matter fluid with density ρ, pressure P, and velocity $\boldsymbol{v}$,

$$\frac{\partial \rho}{\partial t} + \nabla \cdot (\rho \boldsymbol{v}) = 0, \tag{1.26}$$

$$\frac{\partial \boldsymbol{v}}{\partial t} + (\boldsymbol{v} \cdot \nabla)\boldsymbol{v} = -\frac{1}{\rho}\nabla P - \nabla \Phi, \tag{1.27}$$

as well as the Poisson equation for the gravitational potential Φ sourced by the total overdensity $\rho_{\mathrm{tot}} - \bar{\rho}_{\mathrm{tot}}$,

$$\nabla^2 \Phi = 4\pi G(\rho_{\mathrm{tot}} - \bar{\rho}_{\mathrm{tot}}). \tag{1.28}$$

Lets consider the growth of perturbations during matter-domination, which lasted from radiation-matter equality at $z_{\mathrm{eq}} \approx 3400$ until very recently. The gravitational potential is largely sourced by matter, hence we can neglect the contribution from radiation during this time. The fluid variables and potential are split into a homogeneous background

and deviations from this background

$$\begin{aligned}\rho &= \bar{\rho} + \delta\rho,\\ P &= \bar{P} + \delta P = \bar{P} + c_s^2\delta\rho,\\ \boldsymbol{v} &= \bar{\boldsymbol{v}} + \delta\boldsymbol{v},\\ \Phi &= \delta\Phi,\end{aligned} \tag{1.29}$$

where we have assume that the pressure and density perturbations are related by the fluid sound speed c_s via $\delta P = c_s^2\delta\rho$. By changing to comoving coordinates $\boldsymbol{r} = \boldsymbol{x}/a$, we see that the velocity is actually split into the Hubble flow $H\boldsymbol{x}$, i.e. the velocity due to expansion, and the deviation from the Hubble flow,

$$\boldsymbol{v} = \frac{\partial \boldsymbol{x}}{\partial t} = \frac{\partial(a\boldsymbol{r})}{\partial t} = H\boldsymbol{x} + a\frac{\partial \boldsymbol{r}}{\partial t} = H\boldsymbol{x} + a\boldsymbol{u}, \tag{1.30}$$

where $\boldsymbol{u}$ is the comoving velocity, often called the peculiar velocity. Also, since the background density changes with time, it useful to define the density contrast $\delta = \delta\rho/\bar{\rho}$ and consider the evolution of this rather than $\delta\rho$. The linear fluid equations in the comoving frame, with the ∇-operator in comoving coordinates given by $\nabla_c = a\nabla$, are

$$\frac{\partial\delta}{\partial t} = -\nabla_c \cdot \boldsymbol{u}, \tag{1.31}$$

$$\frac{\partial \boldsymbol{u}}{\partial t} + 2H\boldsymbol{u} = -a^{-2}c_s^2\nabla\delta - a^{-2}\nabla_c\delta\Phi, \tag{1.32}$$

$$\nabla_c^2\delta\Phi = 4\pi G a^2\bar{\rho}\delta. \tag{1.33}$$

We can combine these into a single second-order differential equation for δ,

$$\frac{\partial^2\delta}{\partial t^2} + 2H\frac{\partial\delta}{\partial t} = -a^{-2}c_s^2\nabla^2\delta + 4\pi G\bar{\rho}\delta, \tag{1.34}$$

which, upon using the Fourier transformation

$$\delta(\boldsymbol{r}, t) = \sum_{\boldsymbol{k}} \delta_k(t) e^{i\boldsymbol{k}_c\cdot\boldsymbol{r}}, \tag{1.35}$$

where the physical wavenumber $\boldsymbol{k}$ is related to the comoving one $\boldsymbol{k}_c$ by $\boldsymbol{k}_c = a\boldsymbol{k}$, gives

$$\frac{\partial^2\delta_k}{\partial t^2} + 2H\frac{\partial\delta_k}{\partial t} = \left[4\pi G\bar{\rho} - c_s^2k^2\right]\delta_k. \tag{1.36}$$

As we can see from eq. (1.36), the different k-modes decouple in linear theory, and can therefore be treated separately. Several factors affect

the growth of structure: The expansion of the universe acts as a kind of friction, often called the Hubble friction, which slows down the growth rate. Gravity, as expected, causes tiny initial deviations to be unstable and became larger, whereas pressure slows down this process, even halting the gravitational collapse completely at sufficiently small scales by making the right hand side of eq. (1.36) negative. The critical scale below which structure is pressure-supported against gravity is called the Jeans' scale, given by

$$\lambda_{\mathrm{J}} = \frac{2\pi}{k_{\mathrm{J}}} = c_s \sqrt{\frac{\pi}{G\bar{\rho}}}. \tag{1.37}$$

At scales much larger than λ_{J}, it can be shown using eq. (1.36) and the Friedmann equation that during matter-domination the matter density-contrast evolves as $\delta \propto t^n$, with a decaying mode $n = -1$ and a growing mode $n = 2/3$. In fact, the growing mode is proportional to the scale factor, $\delta \propto a$, and is one of the reasons why all of matter cannot have been baryonic and originated from the order 10^{-4} deviations seen in the CMB at $z \sim 1000$. The density-contrast could only have grown by a factor 1000 and would have been $\delta \sim 10^{-1}$ today, which is in stark disagreement with the highly non-linear structure we see all around us. DM is therefore needed, since it was able to grow in the time before recombination, while the baryons were still tightly coupled to the photons and their perturbations stable against gravitational collapse due to the immense radiation pressure.

However, the DM perturbation modes did not grow much during radiation-domination once they entered the horizon. This can be seen by again considering the Newtonian fluid equations for DM with vanishing pressure. During radiation-domination the DM modes are still mostly affected by their own gravitational potential, since the oscillations of the dominant radiation cancel out on average, but the expansion rate is largely determined by the radiation. Lets reinstate the labels for the matter and radiation, and insert for the Hubble parameter using Friedmann's equation, $H^2 = 8\pi G(\bar{\rho}_r + \bar{\rho}_m)/3$. We can change the time-variable from t to $y = a/a_{\mathrm{eq}} = \bar{\rho}_m/\bar{\rho}_r$, which gives

$$\frac{\partial^2 \delta_k}{\partial y^2} + \frac{2+3y}{2y(1+y)}\frac{\partial \delta_k}{\partial y} - \frac{3\delta_k}{2y(1+y)} = 0. \tag{1.38}$$

The growing mode of this equation is $\delta_k \propto 1 + 3y/2$, i.e. it is nearly frozen. Sub-horizon matter density modes did not grown more than by a factor of 5/2 during all of radiation-domination. Simply put, the universe expands at a faster rate than density perturbations can collapse in this period, and is known as the Mészáros effect [81]. Perturbations on scales much larger than the horizon, on the other hand, have not

yet been affected by causal physics and are free to grow as if it obeyed the Friedmann equation. Recall that in a flat universe the Friedmann equation is

$$H^2 = \frac{8\pi G}{3}\rho. \tag{1.39}$$

An overdensity $\delta\rho$ on top of the critical mean density ρ_c induces a local positive curvature $k > 0$, which changes the Friedmann equation to

$$H^2 = \frac{8\pi G}{3}\left(\rho_c + \delta\rho\right) - \frac{k}{a^2}. \tag{1.40}$$

The evolution of the super-horizon density perturbation is therefore given by the evolution of the induced curvature;

$$\delta = \frac{\delta\rho}{\rho_c} = \frac{(k/a^2)}{8\pi G\rho_c/3} \propto \frac{1}{a^2\rho_c}. \tag{1.41}$$

Inserting $\rho_c = \bar{\rho}_r \propto a^{-4}$, since radiation makes up nearly all of the energy budget in the early universe, gives $\delta \propto a^2$ for super-horizon modes during radiation-domination, both for DM and the coupled baryon-photon fluid. The additional growth in the DM modes needed for non-linear structure to form in time for us to observe it today therefore happened in the period between shortly before matter-radiation equality at $z_{\rm eq} \approx 3400$ and recombination at $z_{\rm rec} \approx 1100$.

The growth of linear structure is not only stalled during radiation-domination. In the late universe, with DE-domination, we are again in a period in which the rate of expansion is larger than the linear growth rate. Let us, for a final time, consider the Newtonian equations for sub-horizon perturbations. At $z \approx 0.4$, matter ceased to be the dominant energy component in our universe, giving way to DE, which in the standard model is given by a cosmological constant. Since DE does not cluster (or at least, it does not seem to cluster very much), matter remains the leading contributor to the gravitational potential. Inserting $a(t)$ and H for a largely DE-dominated universe, and defining the time-variable $\tau = H_0\sqrt{\Omega_{\Lambda 0}}t$, therefore gives

$$\frac{\partial^2\delta_k}{\partial\tau^2} + 2\frac{\partial\delta_k}{\partial\tau} = \frac{3}{2}\frac{\Omega_{\rm m0}}{\Omega_{\lambda 0}}e^{-3(\tau-\tau_0)}\delta_k, \tag{1.42}$$

where τ_0 is a reference time. The right hand side of eq. (1.42) is quickly suppressed by the exponential, and the remaining gives $\delta_k =$ constant.

1.5.1 The Matter Power Spectrum

The amount of structure in the universe is effectively quantified by the *matter power spectrum*, which can be inferred from observations, such

as the CMB or galaxy surveys. The matter power spectrum provides a measure for the amount of clustering on a given scale, and can be compared with the theoretical predictions of various models in order to constrain them. Given the overdensity

$$\delta(\boldsymbol{x}) = \frac{\rho(\boldsymbol{x}) - \bar{\rho}}{\bar{\rho}}, \tag{1.43}$$

the matter power spectrum $P(k)$ is defined as the Fourier transform of the two-point correlation function $\xi(\boldsymbol{r})$,

$$\xi(\boldsymbol{r}) = \langle \delta(\boldsymbol{x})\delta(\boldsymbol{x}+\boldsymbol{r}) \rangle \,, \tag{1.44}$$

such that

$$P(\boldsymbol{k}) = \int \mathrm{d}^3x\, \xi(\boldsymbol{x}) e^{-i\boldsymbol{k}\cdot\boldsymbol{x}}. \tag{1.45}$$

In a homogeneous and isotropic universe, the two-point correlation function is independent of the direction of $\boldsymbol{r}$, so that $\xi(r) = \xi(\boldsymbol{r})|_{\boldsymbol{r}=r}$, i.e. the amount of correlation in the density field on a given scale is only dependent on the separation, not the direction. The power is then also independent of the direction, $P(k) = P(\boldsymbol{k})|_{\boldsymbol{k}=k}$. In terms of the overdensity k-modes $\delta_{\boldsymbol{k}}$, the power spectrum is alternatively given by

$$(2\pi)^3 P(k)\delta^3(\boldsymbol{k}-\boldsymbol{k}') = \langle \delta_{\boldsymbol{k}}\delta_{\boldsymbol{k}'} \rangle \,, \tag{1.46}$$

where δ^3 is the 3D Dirac delta function, and $\langle \ldots \rangle$ is an ensemble average.

In the linear regime we can evaluate the matter power spectrum mode-by-mode, since the k-modes are decoupled, and therefore readily use the results from perturbation theory to predict the properties of $P(k)$. For instance, superhorizon modes grow like $\delta_k \propto a^{-2}$ until they enter the horizon. However, the modes that enter during radiation-domination become nearly frozen until matter-domination. The matter power spectrum therefore has a turnover at the scale corresponding to when k-modes started entering the horizon during matter-domination instead of radiation-domination, i.e. the size of the horizon at matter-radiation equality, k_H. The power at $k > k_H$ is suppressed compared to $k < k_H$ due to these modes entering the horizon early during radiation-domination, which is exactly what is seen from observations, as shown in figure 1.4. The shape of the matter power spectrum on large scales, $P(k < k_H) \propto k^n$, is from the primordial perturbations produced by whatever physics operated in the very early universe, with $n \approx 0.96$ [1], close to the $n = 1$ scale-invariant Harrison-Zeldovich spectrum of fluctuations.

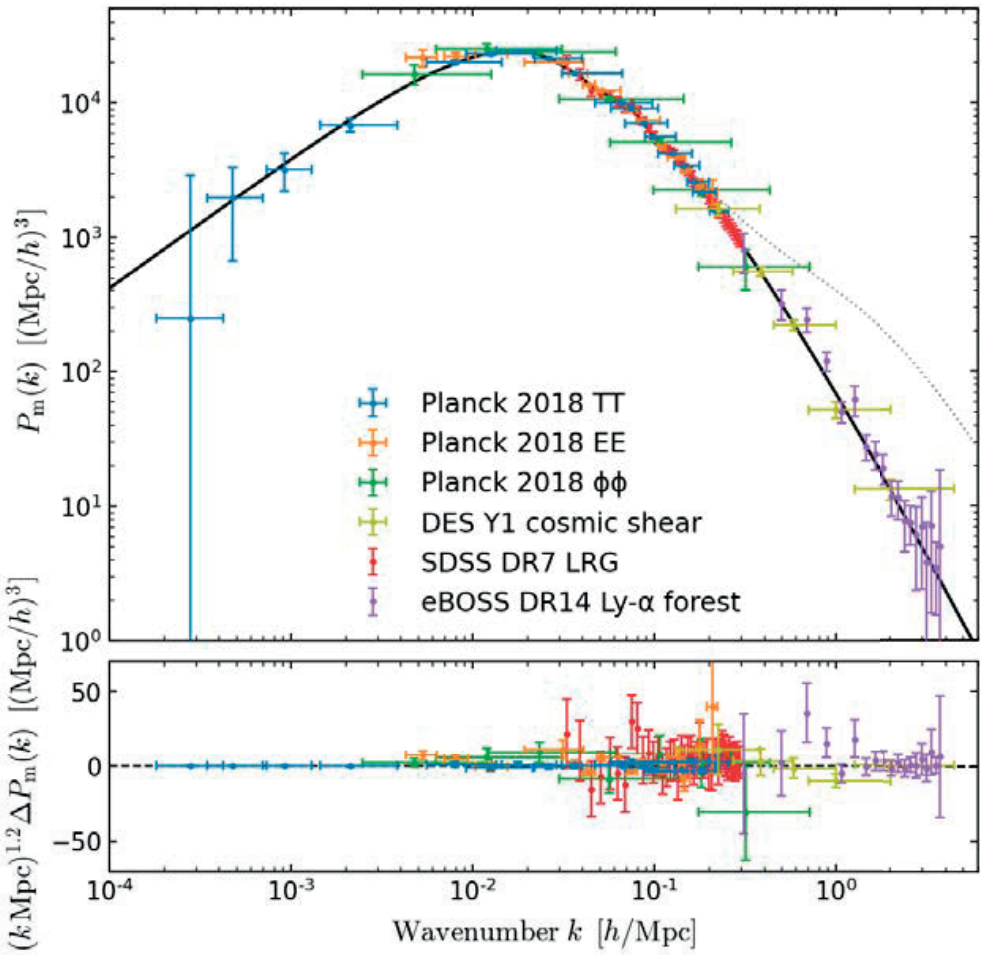

Figure 1.4: The theoretical linear matter power spectrum for the standard ΛCDM model (black) compared to observations, from ref. [20]. The dotted line is the non-linear power spectrum.

1.6 The Non-Linear Universe

Linear theory accurately describes the evolution of structure for a large portion of cosmic history, but when perturbations approach unity, $\delta \sim 1$, non-linear methods are needed. This usually involves large numerical simulations, but some initial insights can be obtained with a simple and analytic model called the *top-hat spherical collapse* model [51, 101].

1.6.1 Top-Hat Spherical Collapse

In the top-hat spherical collapse approximation, we consider the universe to be dominated by cold and collisionless matter with average density

$\bar{\rho}$. A spherical region of overdensity $\delta = 3M/(4\pi\bar{\rho}R^3) - 1$ with mass M and physical radius R obeys eq. (1.13),

$$\frac{\mathrm{d}^2R}{\mathrm{d}t^2} = -\frac{GM}{R^2} = -\frac{4\pi G}{3}\bar{\rho}(1+\delta)R, \tag{1.47}$$

effectively behaving as a closed universe with a "local" scale-factor R. Integrating once gives

$$\frac{1}{2}\left(\frac{\mathrm{d}R}{\mathrm{d}t}\right)^2 - \frac{GM}{R} = E, \tag{1.48}$$

where the constant E is the specific energy of the shell at radius R. The radius is initially $R(t_i) = R_i$, and is expanding with the background, $(\mathrm{d}R/\mathrm{d}t)_i = H_iR_i$. For $E > 0$ the spherical overdensity expands forever, i.e. it never completely decouples from the background expansion to undergo gravitational collapse. For $E < 0$, on the other hand, the overdensity is gravitationally bound, and eq. (1.47) has the solution

$$\begin{aligned} R &= A(1-\cos\theta), \\ t &= B(\theta - \sin\theta), \\ \delta &= \frac{9}{2}\frac{(\theta-\sin\theta)^2}{(1-\cos\theta)^3} - 1, \\ A^3 &= GMB^2 \end{aligned} \tag{1.49}$$

Initially, the shell at R expands with the background universe, but slows down and eventually comes to a halt before collapsing. The maximum radius is called the *turn-around* radius R_{ta}, and is reached at $\theta_{\mathrm{ta}} = \pi/2$, while the collapse happens at $\theta_c = 2\pi$. A realistic overdensity, however, is not perfectly symmetric and homogeneous, and will undergo processes that brings it to virial equilibrium rather than to $R \to 0$ and $\delta \to \infty$. For cold and collisionless matter, the virial theorem states that the gravitational potential and kinetic energy at virial equilibrium, U_{vir} and K_{vir}, satisfies

$$U_{\mathrm{vir}} = -2K_{\mathrm{vir}}. \tag{1.50}$$

Since at virial equilibrium $E = U + K = U_{\mathrm{vir}}/2 = -GM/R_{\mathrm{vir}}$, and at the turn-around radius $E = U_{\mathrm{ta}} = -GM/R_{\mathrm{ta}}$, we have $R_{\mathrm{vir}} = R_{\mathrm{ta}}/2$, i.e. the radius of the gravitationally bound object at virial equilibrium is half the turn-around radius, which is reached at $\theta_{\mathrm{vir}} = 3\pi/2$. The overdensity at this time is $\delta \approx 146$, although the virial overdensity is instead often defined as $\Delta_{\mathrm{vir}} = \rho(3\pi/2)/\bar{\rho}(2\pi) = 18\pi^2 \approx 178$, i.e. the overdensity of the *virialized* object at the time of collapse. Expanding eq. (1.49) to

lowest order in time gives the growth of the overdensity as

$$\delta(t) = \frac{3}{20}\left(\frac{6t}{B}\right)^{2/3}, \tag{1.51}$$

which is the same time-dependence as in the linear regime. Evaluating this linear overdensity at the collapse time $t_c = 2\pi B$ gives $\delta_c \approx 1.69$. This number turns out to be very useful in many applications, for instance the Press-Schechter formalism and its extensions for predicting the abundance of halos of a particular mass, where δ_c is used as a criterion for when modes in linear theory can be regarded as collapsed structures, i.e. as DM halos [109, 100, 15].

There are several important lessons to be learned from this exercise. Not all perturbations collapse and form halos. The initial overdensity needs to be gravitationally bound, otherwise it will never decouple from the background expansion. The overdensity of the final virialized object is independent of the initial halo mass and size. The characteristic density of DM halos as observed today therefore reflects the density of the universe at the time of collapse, $\rho_{\rm halo} \sim \Delta_{\rm vir}\rho_c$. An overdensity of order $\Delta_{\rm vir} \approx 178$ is often used in numerical simulations as a threshold for identifying and extracting information about halos from the density field.

Gravitational collapse and the subsequent formation of realistic halos is far from spherically symmetric, nor do they occur in isolation. Halos interact with one another gravitationally over large distances and merge into more massive structures, continually undergoing changes. Furthermore, the universe contains more than just dark and collisionless matter. Dark energy dominates the late universe, causing the universe to expand at an accelerated pace, and baryonic physics also contributes to the dynamical evolution of DM halos and galaxies. The analytic top-hat spherical collapse model presented above does not include any of this, and to properly model all of these effects, one must resort to numerical simulations.

1.6.2 Numerical Simulations of Structure Formation

Perturbations on scales much larger than 1Mpc are still in the linear regime today, but below a few Mpc matter has collapsed into highly non-linear halos and filaments, creating the vast and intricate structures of the *cosmic web*. Numerical simulations must be employed to study how the initial seeds of the universe evolved from their linear perturbations, through the quasi-linear regime, and finally into the non-linear structures we observe today. Since DM appears to be largely cold and collisionless,

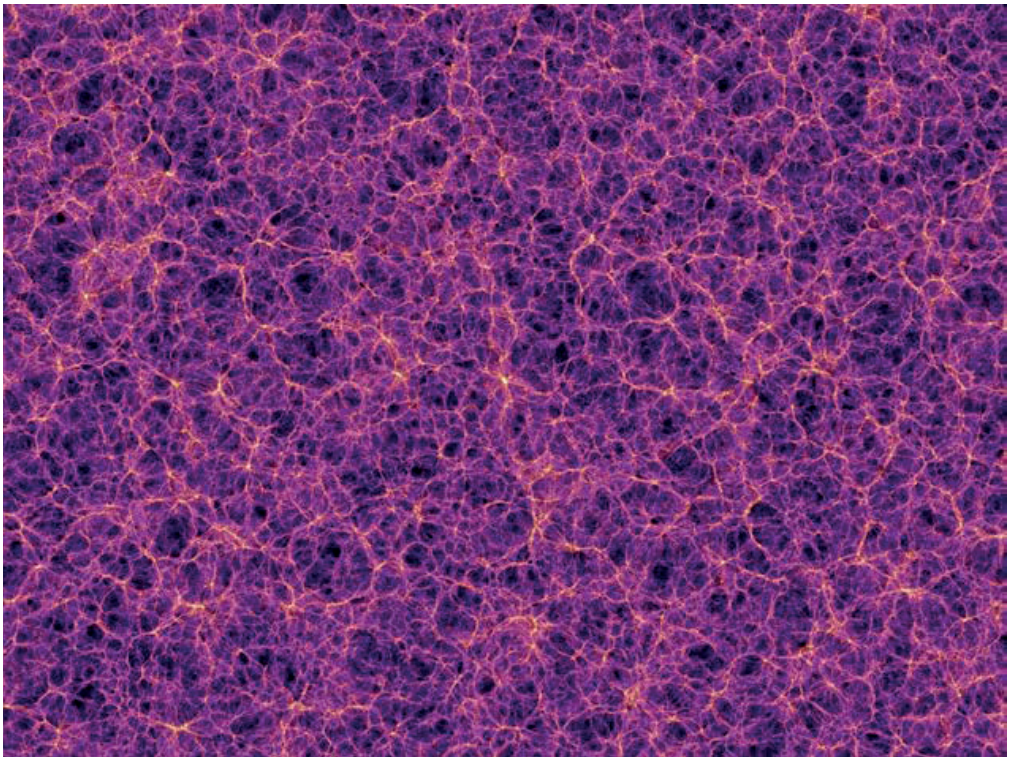

Figure 1.5: A 15Mpc/h thick slice of the DM density distribution in a large-scale cosmological simulation with boxsize 500Mpc/h at $z = 0$. Credit: The Millennium Simulation Project.

numerical methods usually use a generalization of the gravitational two-body problem—the *N-body* problem—to study the formation of DM structures. These simulations are, rather unsurprisingly, called N-body simulations, with the first application carried out using an *analogue* setup. In 1941, Erik Helmberg exploited the fact that the intensity of light decreases with distance r as $1/r^2$, just like Newton's law of gravitation [58]. He therefore used light bulbs to represent the gravitating bodies, and computed the total "gravitational force" on each object by measuring the total intensity of light at the position of the light bulb from all the other light bulbs. A direct summation of the gravitational forces requires $\mathcal{O}(N^2)$ operations for each time-step of the simulation, but Helmberg's light bulb analogue reduces this task to $\mathcal{O}(N)$ operations, or rather, measurements.

Computational astrophysics and cosmology has come a long way since Helmberg's analogue simulation, due to the advent of digital computers and the exponential growth in computing power, as well as advancements in numerical methods, in particular for computing the gravitational potential. Today, N-body simulations running in parallel on modern

supercomputers can use billions—even trillions [61, 108, 26]—of particles in order to trace the evolution of the universe on Mpc and Gpc scales, and the access to a large number of codes in the cosmological and astrophysical community, such as RAMSES [142], GADGET [135, 134, 136], PKDGRAV [138, 137, 108], Gasoline [147, 148], and CONCEPT [30], to name just a few, has made such simulations increasingly commonplace. These codes use a variety of methods for computing the gravitational forces acting on the N-body particles and integrating their paths through time, but they all aim to solve, in some form or another, the geodesic equation, which in the Newtonian limit is

$$\frac{\mathrm{d}^2\boldsymbol{x}}{\mathrm{d}t^2} + 2H\frac{\mathrm{d}\boldsymbol{x}}{\mathrm{d}t} = -a^{-2}\nabla\Phi, \tag{1.52}$$

where the Hubble rate acts as a friction term and takes into account the effect of cosmic expansion on the particles' motion. The most demanding part of an N-body code is accurately computing the total gravitational force on each particle, and there are many strategies for doing so efficiently, reducing the force calculation from the $\mathcal{O}(N^2)$ operations needed for direct summation to $\mathcal{O}(N\log N)$ or better. For instance, the GADGET code uses a tree algorithm, which groups particles together into layered nodes in a hierarchical way. Each node is subdivided into eight sub-nodes, representing a subdivision of the simulated volume into cells with half the cell-length of the parent cell, when the number of particles exceeds a threshold, creating an *oct-tree*. The force contribution of a distant group of particles is computed using their tree node rather than the individual particles, with the depth in the oct-tree used determined by the distance. RAMSES also uses an oct-tree to construct a grid that adaptively increases the grid resolution in areas of interest, called *adaptive mesh refinement* (AMR). However, instead of calculating the gravitational force between each particle using the nodes of the oct-tree, Ramses projects the particle masses onto the grid to get the density field, which it then uses to solve the Poisson equation using multigrid methods. Once the gravitational potential is computed, the gravitational force at the position of each particle is obtained as simply the gradient of the potential.

Cosmological N-body simulations show that DM halos are surprisingly regular in their shapes, and are well-described by a universal halo profile, called the Navarro-Frenk-White (NFW) profile [92, 91],

$$\rho(r) = \frac{\rho_s}{\frac{r}{r_s}\left(1+\frac{r}{r_s}\right)^2}, \tag{1.53}$$

where the parameters ρ_s and r_s are the characteristic density and radius of the halo. Alternatively, halos can be parameterized using a measure

of the halo mass, such as M_{200} (defined as the total mass at r_{200}, inside of which the average density is 200 times the critical density of the universe), and the concentration $C_{200} = r_{200}/r_s$. Simulations also show that cosmic structure is consistent with a hierarchical formation history in which low-mass objects collapsed first, which eventually merged to form increasingly larger structures, such as groups of galaxies, galaxy clusters, and superclusters. As we saw from the analytic top-hat spherical collapse model considered in section 1.6.1, halos that collapse early are expected to be denser than those that form later, since the average density of the universe was higher, a feature that is confirmed by N-body simulations.

Many codes also include methods to account for gas dynamics. The standard hydrodynamic equations describe mass continuity, conservation of momentum, and conservation of energy;

$$\frac{\partial \rho}{\partial t} + \nabla \cdot (\rho \boldsymbol{v}) = 0, \tag{1.54}$$

$$\frac{\partial \boldsymbol{v}}{\partial t} + (\boldsymbol{v} \cdot \nabla)\boldsymbol{v} = -\frac{1}{\rho}\nabla P - \nabla \Phi, \tag{1.55}$$

$$\frac{\partial E}{\partial t} + \nabla \cdot [(E + P)\boldsymbol{v}] = -\rho \boldsymbol{v} \cdot \nabla \Phi, \tag{1.56}$$

which gives the evolution of a fluid with density ρ, velocity field $\boldsymbol{v}$, total energy $E = \rho v^2/2 + U$, and pressure P, under the influence of the gravitational potential. These can be expanded to include radiative transfer and electrically conductive properties to produce the equations for radiation hydrodynamics and magnetohydrodynamics, which are used for e.g. describing the baryonic gases around galaxies or the hot plasma of the Sun.

Numerical simulations of hydrodynamics are more computationally demanding to solve than pure N-body simulations, since the equations of motion are more complex and prone to instabilities unless extra care is taken. Fortunately, after many decades of development, there is a multitude of reliable numerical methods available today, many of which can be categorised into two main types: The first is a Lagrangian-type method called *smoothed particle hydrodynamics* (SPH) [46, 71], which uses moving particles to represent the flow of fluid elements and to carry information about the hydrodynamic and thermal properties of the fluid. SPH methods are therefore a mesh-free way to simulate hydrodynamics that naturally increases the local resolution in high-density regions dynamically, since high mass densities simply corresponds to high number densities of SPH-particles. Additionally, SPH essentially reduces to an N-body scheme in the pressureless limit, making it a

powerful tool for studying the evolution of gas in and around galaxies, and is used in codes such as GADGET and Gasoline.

The second is an Eulerian approach that uses a grid, with the fluid properties stored at each grid position, representing the average local fluid element within a cell of finite volume. The change in the local fluid quantities in each cell is usually obtained by evaluating the flux at each inter-cell boundary, then applying the change due to these fluxes through the interfaces at each time-step. This is called *Godunov's* scheme [47], and preserves the conservative properties of conservative equations, such as the hydrodynamic equations, by passing the outputted flux of a cell as the input flux to its neighboring cells, thereby yielding a net flux of the whole domain that is determined solely by the boundary conditions. For periodic boundary conditions, which is often used in cosmological simulations, the overall flux is therefore zero. Source terms due to e.g. gravity, however, break the conservative properties of the hydrodynamic equations exploited by Godunov's scheme, and must therefore be treated separately, although they can usually be integrated in such a way as to satisfy e.g. the conservation of total fluid energy and potential energy to within some desired limit. Although grid-based methods do not reduce to N-body simulations in the collisionless limit, the grid representing the fluid can more easily be adaptively refined using more general criteria—not just the fluid density—once AMR has been implemented. In this thesis, scalar field models of DM is explored with hydrodynamics, using, among other things, the RAMSES code, a grid-based code for performing cosmological simulations with an implementation of Godunov's scheme and AMR.

1.7 Timeline of the Universe

We have so far considered some of the fundamentals of cosmology, working our way through increasingly more structure and complexity—from the smooth background universe to linear and non-linear structures. We have also briefly mentioned a few important events that have taken place in the early universe, such as the production of light elements during BBN, or the formation of the CMB radiation. However, we have failed to present a simple and clear overview of the most important epochs and milestones of our universe, and their chronological order—a cosmic biography, so to speak. In this section we aim to remedy this.

1.7.1 The Big Bang and the Very Early Universe

Presumably, the universe started at some point (either as a genuine beginning of all time and space, or as some kind of rebirth and start of a

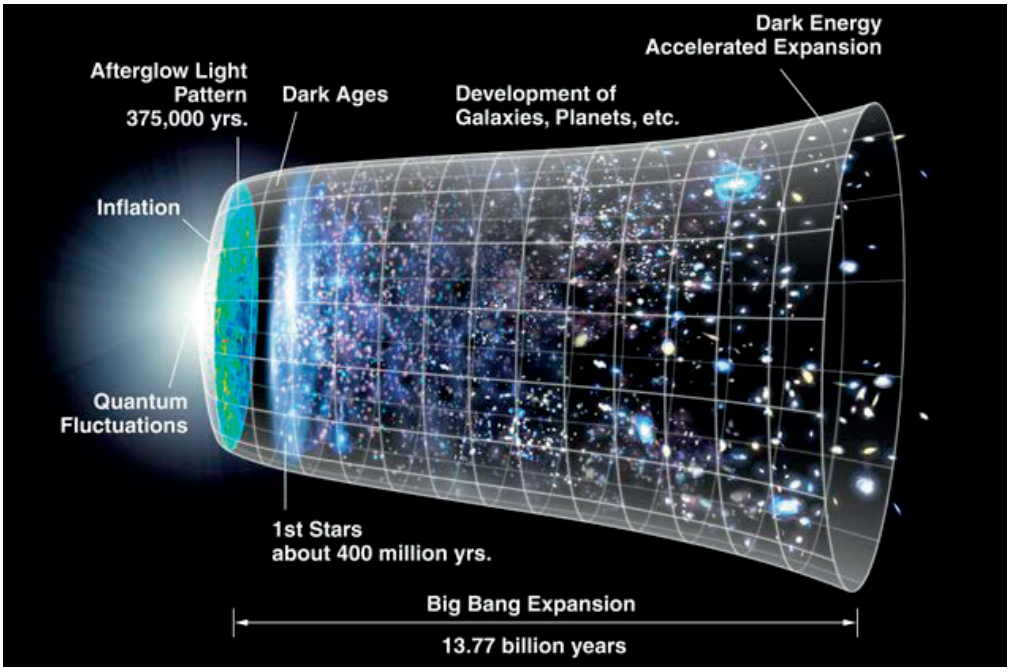

Figure 1.6: A timeline of our universe, from the Big Bang to today. Credit: Original version: NASA/WMAP Science Team; modified by Cherkash.

new cosmic cycle), seemingly expanding from a spacetime singularity—a Big Bang—for which no known physical laws apply. We believe that the birth of our universe was followed by a very short period of extreme expansion, lasting only about 10^{-32}s, but during which the universe expanded by more than 26 orders of magnitude and the initial perturbations in our universe were established [35]. After this period of cosmic inflation, the universe was filled with a hot, relativistic, cosmic soup of particles that began to coalesce into heavier particles as the universe cooled; free quarks and antiquarks ceased being pair-created and annihilated, and an excess of quarks combined to form protons and neutrons, i.e. baryons [64].

1.7.2 Neutrino Decoupling

When cosmic time reached around 1s, or redshift $z \sim 10^{10}$, neutrinos ceased to effectively interact with the cosmic soup, becoming decoupled and no longer in thermal equilibrium with the rest of the universe [64]. The neutrinos therefore became a kind of background of particles that were largely "blind" to the rest of the universe.

1.7.3 Electron-Positron Annihilation

Shortly after neutrino decoupling, at 1s − 10s, or $z \sim 10^{10} - 10^9$, the temperature of the cosmic plasma cooled to below the electron and positron rest mass, and they started to become non-relativistic, no longer being pair-created [64]. Just like the quarks, electrons and positrons annihilated, but a small excess of electrons remained in equal number to the protons, so the universe remained electrically neutral. The energy released from the annihilated particles caused the cosmic plasma to heat up slightly, so that after electron-positron annihilation, the temperature T of the remaining particles is slightly larger than the temperature T_ν of the neutrino background that decoupled earlier and hence received none of this energy. This temperature difference can be found by considering the conservation of entropy before and after electron-positron annihilation;

$$T_\nu = \left(\frac{4}{11}\right)^{1/3} T. \tag{1.57}$$

1.7.4 Big Bang Nucleosynthesis

At around 10s, $z \sim 10^9$, protons and neutrons became able to combine into heavier elements without immediately being disintegrated by high-energy photons. BBN—Big Bang Nucleosynthesis—began to proceed, and produced a significant amount of helium-4, but also trace amounts of deuterium, helium-3, and lithium-7, until about 10^3s, $z \sim 10^7$, when the rate of interactions became too low for the nuclear processes to continue [139], as shown in figure 1.7.

1.7.5 Matter-Radiation Equality

Radiation dominated the energy content of the universe after inflation (or whatever physics operated at those early times). After electron-positron annihilation, photons were the dominant particle specie in terms of energy, followed by relativistic neutrinos. However, the energy density of radiation decreases faster than non-relativistic matter, and at some point matter (baryons and dark matter) began to dominate instead. This cosmic milestone is called matter-radiation equality, and happened at redshift $z \sim 3400$, about 50, 000 years after the Big Bang.

1.7.6 Recombination and the Formation of The Cosmic Microwave Background

After electron-positron annihilation and BBN, the particles that remained in thermal equilibrium were photons, protons (and some heavier elements),

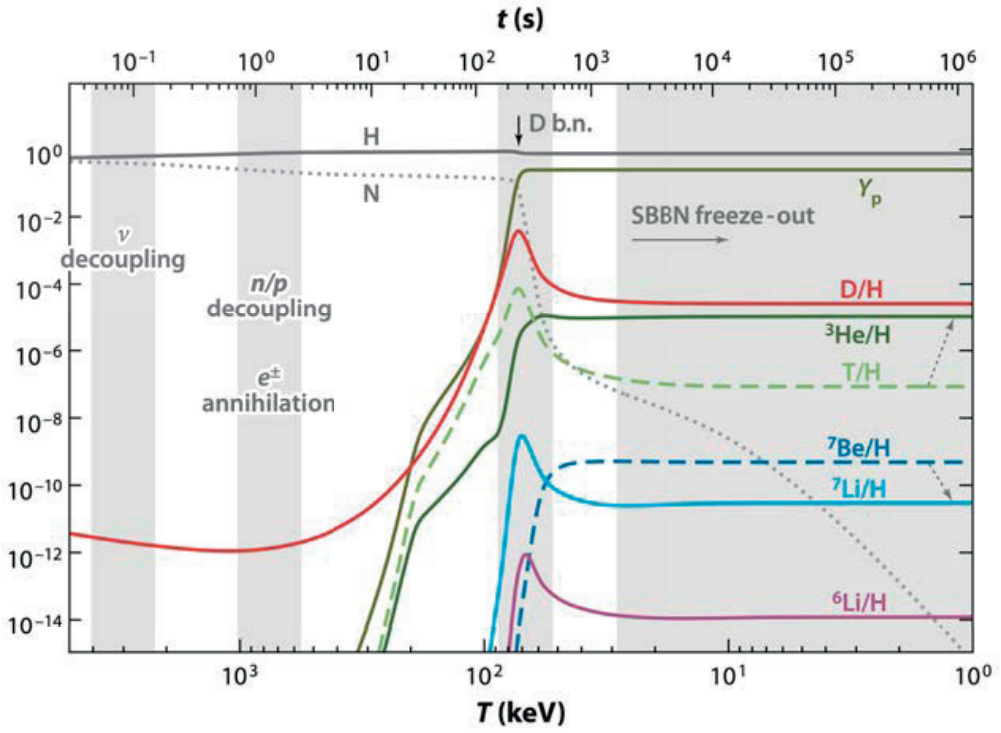

Figure 1.7: The relic abundances of light nuclear elements during standard Big Bang nucleosynthesis (SBBN) until the freeze-out of all nuclear reactions. The helium-4 mass fraction is denoted by Y_p. The figure is from ref. [107].

and electrons. These formed a tightly coupled fluid called the baryon-photon fluid, since the photons could effectively scatter off the free electrons and protons, and therefore had a very small mean free path. At this time, the universe was opaque to photons, and the baryon-photon fluid oscillated due to the high radiation pressure of the photons. Eventually, at $z \approx 1100$, roughly 380,000 years after the Big Bang, the universe cooled sufficiently for electrons and protons to combine to form neutral hydrogen, called recombination [35]. The resulting neutral atoms could no longer interact freely with photons due to their excited states being limited to quantized energy levels, causing photons to decouple and their mean free path to become very large in a short amount of time, essentially making the universe suddenly transparent. These free-streaming photons became the CMB that we observe today, and the imprint of the perturbations of the baryon-photon plasma at the time of recombination has remained in the temperature and polarization anisotropies of the CMB, which has been been—and continues to be—used with much success to obtain valuable knowledge about our universe.

1.7.7 The Dark Ages, Structure Formation, and Reionization

After recombination, the baryonic matter was no longer subject to the high radiation pressure of the photons, and could therefore start to collapse. Since DM decoupled long before baryons (presumably sometime in the very early universe), it started collapsing earlier and established potential wells that the baryons fell into, speeding up the formation of visible structures. However, for a long time the universe was devoid of visible light, since the CMB signal became redshifted to the infrared and no stars and galaxies had yet formed. This period is called the *dark ages*. Eventually, during $z \sim 20 - 6$, between 150 million to one billion years after the Big Bang, matter became sufficiently collapsed and dense to create stars, which became a source of new high-energy photons that reverted the neutral hydrogen gas from recombination into an ionized plasma, a so-called *reionization* of the universe [90], although, due to the low matter density at this time, the universe remained largely transparent.

1.7.8 Dark Energy Domination and Accelerated Cosmic Expansion

Matter dominated the energy content of our universe, and hence cosmic expansion, from matter-radiation equality until very recently. Since $z \approx 0.4$, or around 10 billion years after the Big Bang, a new form of energy has become the dominant component and is causing an accelerated cosmic expansion. This unknown form of energy is what we call DE—dark energy—which is well-described by a cosmological constant, and remains the dominant energy component in our universe today, 13.8 billion years after the Big Bang.

1.8 Open Questions

Although the current standard model of our universe—the ΛCDM model—has proven to be extremely successful in explaining phenomena over a vast range of scales throughout most of cosmic history, there are aspects of the model that are either not entirely in agreement with observations, seemingly internally inconsistent, or that lacks a fundamental theoretical description. Some to these issues might be resolved within ΛCDM through a deeper understanding of the model, while others will likely require a more complete theory of gravity and particle physics. In the following we summarize some of the open questions in the standard model of the universe.

1.8.1 Dark Matter

DM is the dominant matter component in our universe, making up about 85% of all matter, and 25% of the total energy budget in our universe today. Although the simplest model for DM—the cold and collisionless CDM model—provides excellent agreement with observables on nearly all scales, it does not tell us *what* DM is, and is therefore a phenomenological model rather than a microphysical one. An enormous effort is currently being carried out by the astrophysical and cosmological communities in observational, experimental, and theoretical physics to further our understanding of the universe, and one of the central aims of this effort is to find probes for DM. These include probes for DM interactions with standard model particles in particle colliders and scattering experiments, indirect detections from DM annihilation and decays, and the gravitational influence of DM on galactic and cosmological structures. A particularly promising and popular class of DM candidates are weakly interacting massive particles (WIMPs), which have masses in the range $m_{\text{weak}} \sim 10\text{GeV} - \text{TeV}$ and are coupled to standard model particles via the weak interaction. WIMPs are found in many particle theories beyond the standard model, for instance the lightest neutralino in supersymmetry, and fulfill most of the observed requirements for DM, including the correct relic abundance via thermal production. However, no reliable signature of a WIMP has yet been observed, and limits on the parameter space are approaching the neutrino floor, below which any potential WIMP signal will be difficult to distinguish from neutrinos from e.g. the Sun, the atmosphere, and supernovae [115]. It is therefore still an open question what kind of particle DM is, or if it even *is* a new, unknown elementary particle. In fact, our ignorance about the fundamental nature of DM can be illustrated by the sheer scale of the possible mass range for DM, from 10^{-22}eV for ultra-light DM, to primordial black hole DM with masses up to hundreds, or even thousands, of solar masses $M_\odot \sim 10^{66}$eV [42, 146]. Today, what we know with reasonable certainty is that DM

- makes up around 85% of the all matter, and 25% of the total energy in our universe today,
- clusters largely as though it is cold and pressureless,
- is very weakly coupled to the visible sector,
- is unlikely to have been baryonic in nature during BBN or the time leading up to the CMB[2].

[2]It is possible that all or some fraction of DM is made up of primordial black holes, which might have been produced from baryonic matter in the early universe, which would technically make DM "baryonic".

1.8.2 Dark Energy and the Fine-Tuning Problem

DE is the dominant form of energy in our universe today, making up around 70% of the total energy budget, and is the driving force behind the late-time accelerated cosmic expansion. However, like DM, its fundamental nature is a complete mystery. In the standard ΛCDM model, DE is a cosmological constant, which is allowed for in Einstein's field equations. In fact, there is nothing wrong about a cosmological constant being a fundamental quantity of nature, but it might also be a signature of new physics. There are many possible mechanisms that can produce DE, such as modified theories gravity, vacuum energy, or even exotic DM models, but these suggestions usually give rise to a fine-tuning problem. For instance, vacuum energy in quantum field theory has the same properties as a cosmological constant, but the expected contribution from known physics, such as the zero-point energy of quantum fields or the Higgs condensate, gives a value for DE that is many orders of magnitude larger than observed [7]. New physics should therefore somehow provides a cancellation of many orders of magnitude in vacuum energy, leaving only a small amount of energy that we observe as a cosmological constant, but this requires a high degree of fine-tuning of the model parameters.

1.8.3 Cosmological Initial Conditions

All structure we observe today must have been seeded by some mechanism around the time of the Big Bang, providing the initial conditions of our universe, but we do not know what this mechanism was. The currently accepted picture is inflationary theory, which proposes that shortly after the Big Bang, the universe experienced an incredible burst of expansion in an extremely short period of time, expanding by at least a factor of 10^{26} in a period of 10^{-32} seconds [35]. Such a scenario provides a unified solution to several puzzling observations, for instance, that the universe appears to be nearly flat, and that the whole of the CMB is in nearly perfect thermal equilibrium, despite the fact that regions separated by more than around 1° on the sky cannot have been in causal contact in the standard Big Bang scenario. Inflationary theory also provides a mechanism for generating the initial perturbations in our universe by quickly stretching tiny quantum fluctuations to classical scales, which remained after inflation ended. The driving force behind the inflationary epoch is postulated to be one or more co-called *inflaton* fields, although no traces of any such field has been observed.

1.8.4 The Hubble Tension

The Hubble constant H_0 describes the current rate of cosmic expansion, and there are two principle ways of measuring it to a high level of precision. The first is to observe the redshift and luminosity of so-called *standard candles*—astronomical objects of known luminosities, such as Cepheid variables and type Ia supernovae. A *distance ladder* is constructed by calibrating increasingly more distant standard candles, starting with e.g. parallax as the first "rung" of the ladder, to map the apparent distances to objects as a function of their redshifts, which can then be used to trace the expansion history, and gives $H_0 = (73.0 \pm 1.0)$km/s/Mpc [111]. However, this kind of *direct* measurement is limited to relatively low redshifts, around $z \lesssim 2$. The other principle way to find H_0 is to match the theoretical predictions for the CMB within the standard ΛCDM model to the observed CMB signal, from which the Hubble constant is inferred to be $H_0 = (67.4 \pm 0.4)$km/s/Mpc [1]. This *indirect* measurement of H_0 depend crucially on the physics at high redshifts when the CMB was formed, $z > 1000$. The discrepancy between these direct and indirect probes (corresponding to *late*-and *early*-time probes in the context of the CMB signal, and the distance ladder and standard candles) is more than 5σ, and might be due to systematic errors in their respective measurements. If, on the other hand, the tension is real, it might instead hint at physics beyond the standard model. Many models of both DE and DM are in fact motivated by trying to alleviate this interesting tension, although the models considered in this thesis are not.

1.8.5 Small-Scale Structure

While ΛCDM provides an accurate description of the structures in our universe over a large range of scales, there appears to be a possible tension between the theoretical predictions of the model and observations on the scale of low-mass halos [149, 34, 18]. N-body simulations predict NFW density profiles for DM halos, which diverge near the center as r^{-1}, whereas observations instead favor a flatter central slope, i.e. halo cores rather than cusps [98], as shown in figure 1.8. Additionally, simulations predict a high abundance of low-mass halos in our universe, in contrast to the limited number observed in the Local Group. CDM therefore seems to produce too much small-scale structures, and although including baryonic physics in simulations has been found to alleviate these discrepancies somewhat, it is still an area of debate whether or not they are indications of a real underlying issue of the ΛCDM model. An intriguing possibility is for these discrepancy to be due to properties of DM beyond the standard cold and collisionless model. After all, DM is the dominant matter

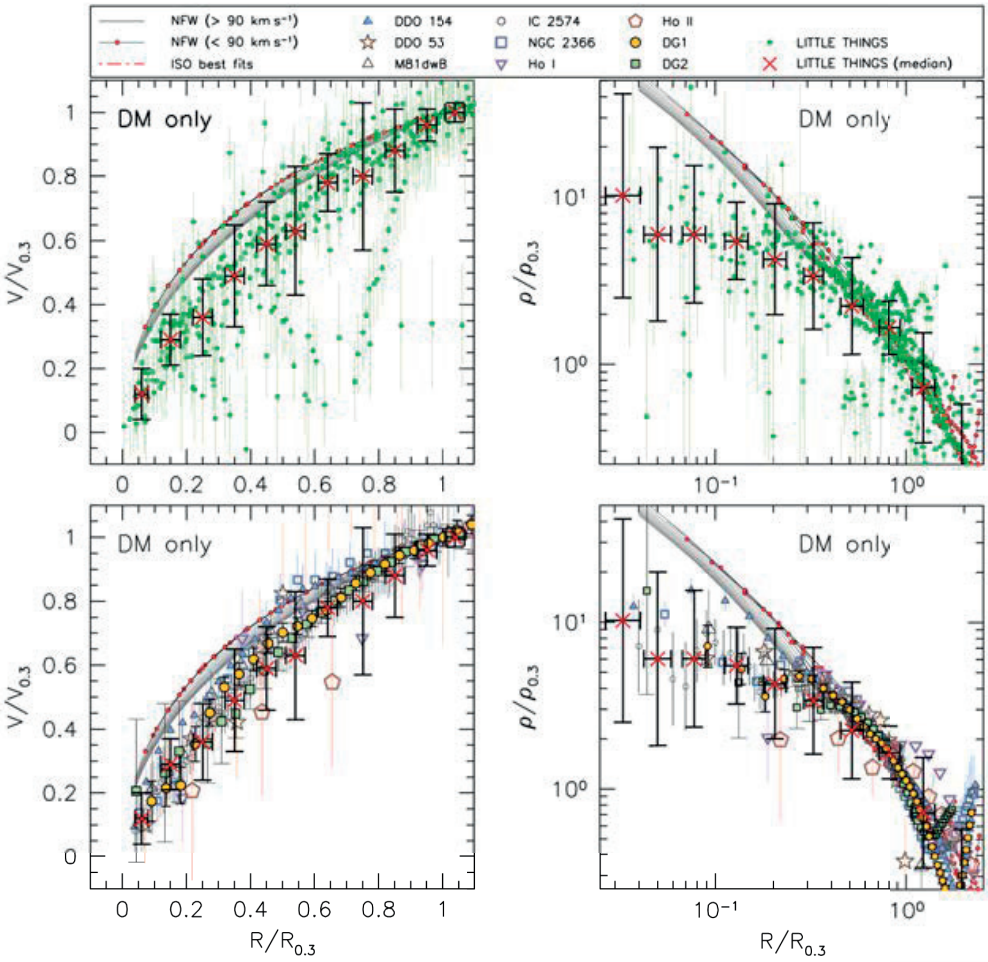

Figure 1.8: Scaled DM rotation curves and density profiles from observations, indicating the presence of DM cores, compared to the cuspy NFW profiles predicted by DM-only simulations. The figure is from ref. [98].

component in the universe, hence DM properties such as warmness, self-interactions, and even wavelike dynamics might affect the distribution of matter in halos that can be observed.

1.8.6 Matter-Antimatter Asymmetry

In the first few moment after the Big Bang, the universe was filled with a hot plasma with pairs of matter and antimatter particles continually being created and annihilated. As the universe expanded and cooled down, the various species of matter (and antimatter) became non-relativistic and ceased to be pair-created. Nearly all of matter and

antimatter then annihilated, except for a small fraction of matter due to an imbalance between matter and antimatter in our universe, which makes up everything we observe around us today. However, our current standard model of physics provides no clear explanation for why our universe had such an imbalance.

1.8.7 Quantum Gravity

Our most fundamental theory of particle physics—describing the nature of particles and their interactions—is formulated within the framework of quantum field theory. Our best theory of gravitation—Einstein's general theory of relativity—on the other hand, is a classical theory, which is incomplete in regions where the effects of gravity are very strong, such as in the vicinity of black holes or in the very early universe. It is therefore desirable to promote the classical theory of gravity to a quantum theory, which in turn might lead to a unified quantum theory of all four fundamental forces of nature. However, current efforts to formulate gravity using the principles of quantum field theory have thus far failed, suggesting that quantum gravity might need to be formulated within a new framework, such as loop quantum gravity or string theory.

Many of these open questions may be related to one another. For instance, a quantum theory of gravity might help us better understand the origin of the structure in our universe, while a theory beyond the standard model of particles might explain both the asymmetry of matter and antimatter, and the nature of DE and DM. In this thesis, we are instead largely concerned with the description of DM beyond the CDM paradigm, specifically scalar field DM, and how that affects the growth and distribution of matter in the universe, including small-scale structures.

Chapter 2

Ultra-light Dark Matter

The continued non-detection of a WIMP candidate for DM increasingly opens up the possibility that DM is another kind of particle entirely, and that other lines of investigation should be considered. Ultra-light scalar and pseudo-scalar fields are an intriguing alternative in this regard, since at least one fundamental scalar field is known to exist—the Higgs field—and others arise in theories beyond the standard model, such as the axion as a solution to the strong-CP problem in quantum chromodynamics, or as a generic prediction of string theory [75]. For masses in the range 10^{-22}eV to 1eV, ultra-light DM (ULDM) exhibit wave-like behaviour at astrophysical scales, and might therefore also offer a solution to the small-scale issues of ΛCDM that CDM-like candidates such as WIMPs struggle to explain, as well as give rise to a rich phenomenology (depending on the mass and interactions of the field) that can affect DM structures on large and small scales. In this section we review some of the basic theoretical framework and features of ULDM that are relevant for the work carried out during this PhD.

2.1 Condensation and the Non-Linear Schrödinger Equation

The wave-like dynamics of ULDM become important when the de Broglie wavelength $\lambda_{\rm dB}$ is larger than the inter-particle distance l of DM particles [43],

$$\lambda_{\rm dB} \sim \frac{1}{mv} > l = \left(\frac{m}{\rho}\right)^{1/3}, \tag{2.1}$$

which in terms of the mass is

$$m < \left(\frac{\rho}{v^4}\right)^{1/3}. \tag{2.2}$$

If we insert the characteristic density and velocity of DM in halos of mass M at redshift $z_{\rm vir}$,

$$\rho_{200} = 200\rho_c \sim 1.95 \times 10^{-27}(1+z_{\rm vir})^3\,{\rm g/cm^3}, \tag{2.3}$$

$$v_{200} \sim 85\Big(\frac{M}{10^{12}M_\odot}\Big)^{1/3}\sqrt{1+z_{\rm vir}}\,{\rm km/s}, \tag{2.4}$$

we get

$$m < 2.3(1+z_{\rm vir})^{3/8}\Big(\frac{M}{10^{12}M_\odot}\Big)^{-1/4}\,\text{eV}. \tag{2.5}$$

Below this mass, a DM scalar field is hypothesised to transition into a phase in which the occupation number of a coherent state described by a single wavefunction becomes very large. A more illustrative description of this phase can be obtained by considering the grand canonical ensemble for a homogeneous gas of bosons. Below a critical temperature T_c, a macroscopic fraction of particles will start to aggregate in the quantum state of minimum energy, undergoing a phase transition until at $T = 0$ the whole system shares the same quantum state and wavefunction [104, 106]. This phenomenon is called Bose-Einstein condensation (BEC) [16, 37], and is a unique phase of matter in which the quantum mechanical effects of the system become apparent in the macroscopic realm. In fact, BECs have been an active active area of research in condensed matter physics—both theoretically and experimentally—for decades. For a homogeneous and ideal bosons gas, the fraction of particles in the BEC is

$$\frac{n_0}{n} = 1 - \left(\frac{T}{T_c}\right)^{3/2}, \tag{2.6}$$

where the critical temperature T_c is

$$T_c = \frac{2\pi}{m}\left(\frac{n}{\zeta(3/2)}\right)^{2/3}, \tag{2.7}$$

and n is the total particle number density, n_0 is the number density of the condensate, and $\zeta(x)$ is the Riemann zeta function. Following a procedure familiar from condensed matter physics, the equations of motion for a BEC can be derived from the many-body quantum Hamiltonian of the system

$$\hat{H} = \int \mathrm{d}^3 r\, \hat{\Psi}^\dagger \Big[-\frac{\nabla^2}{2m} + V \Big]\hat{\Psi} + \frac{g}{2}\int \mathrm{d}^3 r\, \hat{\Psi}^\dagger\hat{\Psi}^\dagger\hat{\Psi}\hat{\Psi}, \tag{2.8}$$

where $\hat{\Psi}$ is the second quantized boson field operator, V is an external potential, and g is the coupling strength of an effective two-body contact interaction. In the Heisenberg picture, the equation of motion for the field operator is given by

$$i\frac{\partial\hat{\Psi}}{\partial t} = [\hat{\Psi}, \hat{H}] = \Big(-\frac{\nabla^2}{2m} + V \Big)\hat{\Psi} + g\hat{\Psi}^\dagger\hat{\Psi}\hat{\Psi}. \tag{2.9}$$

Solving the full many-body problem is challenging, but in the BEC phase, where the majority of particles are in the condensate, a *mean-field*

approximation due to Bogoliubov can be used [13]. The field operator is separated into a classical field ψ and quantum perturbations $\delta\hat{\psi}$,

$$\hat{\Psi} = \psi + \delta\hat{\psi}, \tag{2.10}$$

where the classical component satisfies $\psi = \langle\hat{\Psi}\rangle$ and is the wavefunction of the condensate, while the perturbations have $\langle\delta\hat{\psi}\rangle = 0$ and describe excitations on top of the BEC, i.e. the ground state. Furthermore, $n_0 = |\psi|^2$, and as $T \to 0$ we have $n_0 \approx n$, where the approximate sign is due to an effect called *quantum depletion* when interactions are present, which forces a small fraction of particles out of the condensate even at absolute zero [104, 70]. For our purposes, however, this effect is negligible. In weakly interacting and dilute bose gases well below the critical temperature, the mean-field approximation for the equation of motion of the condensate wavefunction is therefore

$$i\frac{\partial\psi}{\partial t} = \left(-\frac{\nabla^2}{2m} + V + g|\psi|^2 \right)\psi, \tag{2.11}$$

and is known as the Gross-Pitaevskii equation [50, 105], or the non-linear Schrödinger equation (NLSE).

For a DM scalar field to be described by a macroscopic shared wavefunction, it must presumably have been produced in the early universe in such a way that the field was either initially in the coherent state, for instance via the misalignment mechanism; or the field thermalized and underwent a phase transition, possibly through gravitational interactions or self-couplings. There is, however, no consensus on the precise nature of Bose-Einstein condensation in scalar field DM, and under what circumstances scalar DM particles can form a BEC with long-range order, described by a single (classical) wavefunction [76, 144, 126, 125, 40, 32, 52, 10, 75]. In the following, we simply assume that such a description is valid for scalar field DM.

2.2 Ultra-light Scalar Fields in Cosmology

In cosmology the potential of interest is the gravitational potential, hence we replace $V = \Phi$. The NLSE can alternatively be derived from the action of a minimally coupled scalar field, for instance a complex scalar field with the Lagrangian

$$\mathcal{L} = \frac{1}{2}g_{\mu\nu}\partial^\mu\Psi^*\partial^\nu\Psi - \frac{1}{2}m^2|\Psi|^2 - \frac{1}{2}gm^2|\Psi|^4, \tag{2.12}$$

which, upon defining $\Psi = \psi e^{-imt}/\sqrt{m}$ and taking the non-relativistic limit, also yields the NLSE. A real scalar field, with $\Psi = \Psi^*$, is also

often considered, for which the NLSE is instead obtained by the field redefinition $\Psi = (\psi e^{-imt} + \psi^* e^{imt})/\sqrt{2m}$. The relativistic Lagrangian provides a description of ULDM in the regime where the non-relativistic NLSE is invalid, and is necessary for studying ULDM at early-times. The background evolution of the scalar field Ψ in an expanding universe is

$$\frac{\partial^2 \Psi}{\partial t^2} + 3H\frac{\partial \Psi}{\partial t} + m^2\Psi + 2gm^2|\Psi|^2\Psi = 0. \tag{2.13}$$

In the free-field limit of a real scalar field, in a universe with scale factor $a \propto t^p$, the above admits the solution [75]

$$\Psi = a^{-3/2}(t/t_i)^{1/2}[C_1 J_n(mt) + C_2 Y_n(mt)], \tag{2.14}$$

where J_n and Y_n are Bessel functions of the first and second kind, respectively, t_i is the initial time, and $n = (3p-1)/2$. At early times when $H \gg m$, the scalar field is overdamped and frozen due to the large Hubble friction. Such a field has equation of state $w = -1$, and hence behaves as DE. In the complex case, we instead find a stiff era with $w = 1$ [69]. The energy density of this phase goes like $\rho \sim a^{-6}$, such that the universe is dominated by the self-interacting scalar field during this time.

Eventually the expansion rate slows such that $H \ll m$, whereupon the field instead becomes underdamped and begins to oscillate. In the free-field limit the frequency of the oscillations is $\omega = m$, and the equation of state oscillates between $-1 < w < 1$, but sufficiently fast that it averages to $\langle w \rangle = 0$, and therefore evolves as matter. The interacting case is a bit more complicated, since then the field oscillations also depend on the self-interaction and the field itself [77, 69],

$$\omega = m\sqrt{1 + \frac{2g}{m}|\Psi|^2}. \tag{2.15}$$

The interaction energy dominates initially, causing the scalar field to behave as radiation, $w = 1/3$. Only once the field is sufficiently diluted and the interaction energy becomes subdominant does the self-interacting ULDM behave as matter, although with some remaining interaction pressure. This can be seen quantitatively by evaluating the equation of motion and averaging over oscillations [69];

$$\langle |\partial_t \Psi|^2 \rangle = m^2 \langle |\Psi|^2 \rangle + 2gm^2 \langle |\Psi|^4 \rangle . \tag{2.16}$$

The resulting averaged background energy density and pressure is

$$\langle \bar{\rho} \rangle = m \langle |\Psi|^2 \rangle + \frac{3}{2} g \langle |\Psi|^2 \rangle^2 , \tag{2.17}$$

$$\langle \bar{P} \rangle = \frac{1}{2} g \left\langle |\Psi|^2 \right\rangle^2 = \frac{m^2}{18g} \left(\sqrt{1 + \frac{6g \langle \bar{\rho} \rangle}{m^2}} - 1 \right)^2. \tag{2.18}$$

The interaction-dominated limit $g \langle \bar{\rho} \rangle / m^2 \gg 1$ gives the radiation-like pressure $\langle \bar{P} \rangle = \langle \bar{\rho} \rangle / 3$, while $g \langle \bar{\rho} \rangle / m^2 \ll 1$ gives the non-relativistic pressure $\langle \bar{P} \rangle = g \langle \bar{\rho} \rangle^2 / 2m^2$. A very simple approximation for the equation of state in these two regimes, accurate to within $20\% - 30\%$, is [53]

$$w_0 = \frac{\bar{P}}{\bar{\rho}} = \frac{1}{3} \frac{1}{1 + a^3/3w_0}, \tag{2.19}$$

where w_0 is the non-relativistic equation of state today.

Returning to the non-relativistic regime, the NLSE can be recast in a hydrodynamical form by substituting for the wavefunction

$$\psi = \sqrt{n} e^{iS} = \sqrt{\frac{\rho}{m}} e^{iS}, \tag{2.20}$$

where $\rho = mn$ is the mass density, and the velocity field is defined by $\boldsymbol{v} = \nabla S / m$, which gives the Madelung equations [74],

$$\frac{\partial \rho}{\partial t} + \nabla \cdot (\rho \boldsymbol{v}) = 0, \tag{2.21}$$

$$\frac{\partial \boldsymbol{v}}{\partial t} + (\boldsymbol{v} \cdot \nabla) \boldsymbol{v} + \nabla \left(\frac{g\rho}{m^2} - \frac{1}{2m^2} \frac{\nabla^2 \sqrt{\rho}}{\sqrt{\rho}} + \phi \right) = \mathbf{0}. \tag{2.22}$$

These equations describe the conservation of mass and momentum of the condensate fluid, but differs from standard hydrodynamics by the absence of an energy equation, the presence of a self-interaction pressure (the same as we found in the non-relativistic limit above),

$$P_{\rm SI} = \frac{g\rho^2}{2m^2}, \tag{2.23}$$

and a so-called quantum potential

$$Q = -\frac{1}{2m^2} \frac{\nabla^2 \sqrt{\rho}}{\sqrt{\rho}}. \tag{2.24}$$

Both the NLSE and the Madelung equations have been widely used in cosmology to study the formation of structure in models of ULDM, such as the properties of low-mass halos and galaxies [80, 48, 14, 24, 25, 113, 60, 151, 8, 29, 65] to simulations [119, 120, 121, 87, 88, 145, 95, 85, 86, 96, 78]. At large scales they reproduce the successes of CDM, behaving as a dark, cold, and collisionless matter component, while at small scales the

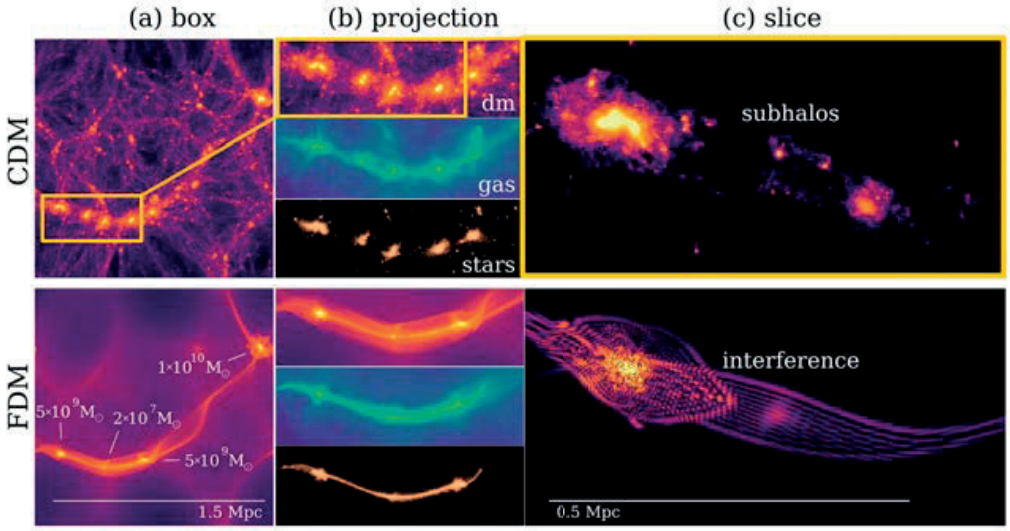

Figure 2.1: Snapshots from CDM (*upper*) and FDM (*lower*) simulations at $z = 5.5$ and FDM mass $m = 2.5 \times 10^{-22}$eV. Shown are (a) projection plots of the simulated domain, (b) projections of the DM, gas and star components in a filament, and (c) a slice through a filament. The figure is from ref. [88].

wave-like behaviour, as well as interactions if present, become important. In the free-field limit, where $g = 0$, only the quantum potential remains as a dispersive term in the Madelung equations, and can be regarded as an expression of the Heisenberg uncertainty principle, i.e. the reluctance of the wavefunction to become localized at any given position, which is why this kind of DM is often called Fuzzy DM (FDM). The quantum potential allows the FDM field to resist gravitational collapse at the scale of the particles' de Broglie wavelength. In the center of FDM halos, the density profile transitions to a soliton solution, which is cored rather than cuspy. Furthermore, FDM produces interference patterns in halos and filaments due to its wave-like nature, a feature that is very distinct from CDM, as seen in figure 2.1.

In an expanding universe, the linear equation for the self-gravitating FDM overdensity in Fourier space is [75]

$$\frac{\partial^2 \delta_k}{\partial t^2} + 2H\frac{\partial \delta_k}{\partial t} = \left[4\pi G\bar{\rho} - \frac{k^4}{4m^2a^2}\right]\delta_k, \tag{2.25}$$

from which we identify a k-dependent effective sound speed due to the quantum potential that is solely given by the mass of the ULDM particle,

$$c_s^2 = \frac{k^2}{4m^2a^2}, \tag{2.26}$$

which suppresses the growth of small-scale structures. At hydrostatic equilibrium, halos of mass M have core radii of order [80]

$$R_{\rm FDM} = \frac{10}{GMm^2}. \tag{2.27}$$

i.e. more massive halos produce smaller solitonic cores, a feature that has been confirmed by large scale simulations [21]. FDM is therefore a DM candidate that might provide a dark-sector solution for some of the small-scale issues of ΛCDM, although recent bounds from the Lyman-alpha forest seem to rule out the canonical mass range needed to do so [114].

ULDM with self-interactions, usually in the limit where the quantum potential can be largely neglected, called the Thomas-Fermi limit, is also an interesting DM alternative that might help explain the small-scale discrepancies of ΛCDM. We refer to this kind of DM as self-interacting Bose-Einstein condensate (SIBEC) DM, and a useful relation can be obtained by considering SIBEC-DM halos at hydrostatic equilibrium, which gives the density profile [48]

$$\rho(r) = \rho_0 \frac{\sin(Ar)}{Ar}, \tag{2.28}$$

where $A = \sqrt{4\pi G m^2/g}$, and vanishes at

$$r = R_c = \sqrt{\frac{g\pi}{4Gm^2}}. \tag{2.29}$$

SIBEC-DM halos are therefore also naturally cored due to the self-interaction pressure, although realistic halos do not vanish completely at R_c, but instead transition to a NFW envelope [54]. Unlike FDM, the hydrostatic core radii of SIBEC-DM halos are independent of the halo masses and central densities, and are instead only given by the model parameters, g/m^2. The universal core radius R_c is therefore an alternative way to parameterize SIBEC-DM in the Thomas-Fermi limit, and is related to the equation of state today in eq. (2.19) by

$$w_0 \approx 10^{-15} \left(\frac{R_c}{1\text{kpc}}\right)^2. \tag{2.30}$$

2.3 Superfluidity

A pressure solely dependent on the model parameters and local density (i.e. no thermal dependence) is not the only special feature of SIBEC-DM.

BECs with self-interactions are superfluids, which at finite temperatures behave in very peculiar ways, unlike anything we expect from conventional fluids.

To see why interactions are necessary for BEC superfluids, lets recount one of their unique properties; that they can flow past obstacles without dissipating energy. If we imagine a heavy obstacle moving at constant velocity $\boldsymbol{v}$ through a condensate in its ground state, it can be shown that in the frame of the obstacle the energy needed to produce an excitation in the condensate is $\epsilon_p - \boldsymbol{p}\cdot\boldsymbol{v}$, where $\boldsymbol{p}$ and ϵ_p are the momentum and energy of the excitation. However, in the frame of the obstacle, its potential is static, hence it cannot transfer energy to the condensate, making it impossible for excitations to spontaneously appear for velocities smaller than

$$v < v_c = \min\left(\frac{\epsilon_p}{p}\right). \tag{2.31}$$

Only for $v > v_c$ can excitations be produced in the BEC fluid that can contribute to dissipation. The quantity v_c is therefore called the critical velocity, and eq. (2.31) is known as the *Landau criterion* for superfluidity [66]. The excitations in an ideal BEC are just free particles with $\epsilon_p = p^2/2m$, which gives $v_c = 0$. Ideal BECs are therefore not superfluid, as any motion of an obstacle can cause dissipation. In an interacting BEC, on the other hand, the elementary excitations of the condensate are no longer free particles, but collective modes, or *quasi-particles*. For the system given by the Hamiltonian in eq. (2.8), the energy spectrum of the quasi-particles is

$$\epsilon_p = \sqrt{\frac{p^2}{2m}\left(\frac{p^2}{2m} + 2gn\right)}, \tag{2.32}$$

whose long-wavelength excitations are sound modes with $\epsilon_p = c_s p$, where the sound speed is $c_s = \sqrt{gn/m}$. The critical velocity is in this case $v_c = c_s > 0$, hence interacting BECs are superfluids.

At $T = 0$, a SIBEC is entirely superfluid and well-described by the NLSE for the condensate. At finite temperatures, on the other hand, the system is not entirely superfluid. There is a thermal component, composed of thermal excitations that carries thermal energy and entropy, and can experience dissipation, just like a regular fluid. In fact, a finite-temperature superfluid is perhaps best described as a two-fluid system; one component is superfluid (in the usual sense); the other component behaves as a conventional, or *normal*, fluid. In many systems, the superfluid and non-superfluid components correspond roughly to the condensate and non-condensate fractions, but not exactly. For instance, at $T \to 0$, quantum depletion of the condensate due to interactions

causes the bose gas to not be entirely Bose-Einstein condensed, i.e. share a single coherent wavefunction, but it can still be entirely superfluid. In strongly interacting liquids, such as superfluid ^{4}He, the depletion is even stronger and the condensate fraction never exceeds 10%, while the superfluid fraction approaches unity. In weakly interacting fluids the distinction between the condensate and superfluid fraction is small, and the two terms are often used interchangeably.

The two-fluid hydrodynamic equations for a finite-temperature superfluid, in the Thomas-Fermi limit, are [141, 23]

$$\frac{\partial \rho}{\partial t} + \nabla \cdot \boldsymbol{j} = 0, \tag{2.33}$$

$$\frac{\partial S}{\partial t} + \nabla \cdot (S\boldsymbol{u}_n) = 0, \tag{2.34}$$

$$\frac{\partial \boldsymbol{u}_s}{\partial t} + \nabla(\mu + \frac{1}{2}\boldsymbol{u}_s^2) = -\nabla\Phi, \tag{2.35}$$

$$\begin{aligned}\frac{\partial \boldsymbol{j}}{\partial t} &+ \nabla P + \rho_s(\boldsymbol{u}_s \cdot \nabla)\boldsymbol{u}_s + \rho_n(\boldsymbol{u}_n \cdot \nabla)\boldsymbol{u}_n \\ &+ \boldsymbol{u}_s[\nabla \cdot (\rho_s \boldsymbol{u}_s)] + \boldsymbol{u}_n[\nabla \cdot (\rho_n \boldsymbol{u}_n)] = -\rho\nabla\Phi.\end{aligned} \tag{2.36}$$

The normal fluid component has density ρ_n, velocity $\boldsymbol{u}_n$, and transports both mass and thermal energy, while the superfluid component has density ρ_s, a velocity field $\boldsymbol{u}_s$, and carries no entropy. The total mass density and momentum is the sum of the two components, $\rho = \rho_n + \rho_s$ and $\boldsymbol{j} = \rho_n \boldsymbol{u}_n + \rho_s \boldsymbol{u}_s$, and the fluid pressure is P, the entropy density S, temperature T, and $\mu = [P + U - ST - \frac{1}{2}\rho_n(\boldsymbol{u}_s - \boldsymbol{u}_n)^2]/\rho$.

The partially independent motion of the superfluid and normal fluid components allows for mass and entropy to move separately. This is best seen if we introduce the net mass velocity $\boldsymbol{v} = \boldsymbol{j}/\rho$, the counterflow velocity $\boldsymbol{w} = \boldsymbol{u}_s - \boldsymbol{u}_n$, and insert into the continuity equations for mass and entropy,

$$\frac{\partial \rho}{\partial t} + \nabla \cdot (\rho \boldsymbol{v}) = 0, \tag{2.37}$$

$$\frac{\partial S}{\partial t} + \nabla \cdot (S\boldsymbol{v}) - \nabla \cdot \left(\frac{S\rho_s}{\rho} \boldsymbol{w} \right) = 0. \tag{2.38}$$

The entropy equation has an extra flux term due to the counterflow of the superfluid and normal fluid, and is therefore known as *thermal* counterflow. There is an additional sound mode associated with counterflow, called second-sound, which propagates entropy and temperature perturbations rather than density perturbations. Furthermore, the equation for the counterflow $\partial \boldsymbol{w}/\partial t$ contains a term $S\boldsymbol{\nabla}T/\rho_n$, driving the counterflow

to be directed towards higher temperatures, making superfluids very efficient at redistributing thermal differences. However, the counterflow cannot become arbitrarily large, because the Landau criterion also applies to the relative motion of the superfluid and normal fluid, where the thermal excitations play the role of obstacles in the superfluid. This effect is not included in the two-fluid hydrodynamic eqs. (2.33)-(2.36), and must be added separately as an additional mutual friction term (see e.g. refs. [49, 36, 128, 129, 31, 131]). The critical velocity for the counterflow is smaller than the sound speed c_s, though for weak interactions and temperatures well below T_c, the difference is small [93].

Chapter 3

Summary and Outlook

This thesis represents an effort to further our understanding of self-interacting scalar field models of DM. Several variants of this kind of DM have been proposed as alternatives to CDM in order to alleviate the small-scale tensions in ΛCDM, and the addition of self-interactions has important consequences for the phenomenology of scalar field DM. As we saw in Chapter 2, self-interactions give rise to a mean-field potential in the NLSE, and a non-thermal pressure in the hydrodynamic formulation, that modifies the central structure of DM halos, creating cores rather than cusps, as well as changing the properties of DM at early times. At finite temperatures, the self-interacting scalar field exhibits superfluidity that can produce very different features than what one would naively expect from standard hydrodynamics. The four papers produced during this PhD deal with these aspects of scalar field DM, and in the following, we give a short summary of these papers.

3.1 Summaries of Papers

Paper I

This paper was motivated by the superfluid DM model presented in ref. [9], which was constructed to give rise to modified Newtonian dynamics (MOND) [84, 82, 83] inside galaxies. The MONDian force, which has been shown to reproduce observed scaling relations in galaxies that are not easily explained in ΛCDM [41], such as the baryonic Tully-Fisher relation [79] that relates the observed asymptotic circular velocity v_c in galaxies with their baryonic mass M_b by $M_b \propto v_c^4$, comes about in this model when DM condenses inside galaxies and the superfluid phonons propagate an extra force between visible matter. The advantage of this realization of MOND is that outside galaxies, where MOND generally fails to reproduce observations, the scalar field DM does not propagate the extra force and behaves as CDM. However, for the superfluid phonons inside galaxies to be stable, ref. [9] assumed that the DM superfluid was at finite temperatures. In Paper I we therefore considered how the growth of structure could be affected by such a finite temperature superfluid by performing 1D simulations of spherically symmetric superfluid overdensities using two-fluid hydrodynamics, eqs. (2.33)-(2.34), starting from tiny initial perturbations and simulating until

the non-linear regime. The models considered in Paper I are not strictly the same as the one proposed in ref. [9], since their MONDian superfluid cannot come from a weakly interacting scalar theory with simple 2-body or 3-body interactions. Instead they serve as simplified prototypes for superfluid DM at finite temperatures. We found that even in the presence of a large thermal pressure, which would significantly slow down the growth of structures in a conventional fluid, the thermal counterflow of the superfluid was able to effectively redistribute the thermal energy during collapse, making the halo centers colder than expected. The superfluid halos could therefore collapse largely unimpeded by the thermal pressure.

Paper II

In this paper we continued to explore the effect of superfluid thermal counterflow in self-interacting scalar field DM, this time for a gravitational drag effect called dynamical friction, generalizing the results of ref. [8] to finite temperatures in the Thomas-Fermi limit. A massive object moving through a background medium, such as a cluster of stars or a gas cloud, creates an overdensity that trails it due to its gravitational interaction with the background, which in turn exerts a net gravitational force on the massive body opposite its direction of motion. The nature of this gravitational drag force depends on how the background medium responds to the initial perturbing body, and is different for e.g. collisionless particles [22, 89, 28, 11], ideal gases [99, 118, 67, 68, 143], relativistic fluids [5, 63], and magnetized fluids [117, 123]. Since DM dominates the matter content in the universe, in particular inside galaxies, dynamical friction can be used as an indirect probe for DM (for instance FDM as was done in ref. [65]), even if DM is completely decoupled from the visible sector, since the dynamical friction only operates via the gravitational force. In Paper II we derived equations for the dynamical friction force on an object moving through a superfluid background medium from linear perturbation theory that we tested against idealized hydrodynamic simulations, which confirmed the linear results. We found once again the thermal counterflow to effectively redistribute the thermal energy in such a way that the DM superfluid could respond to the massive perturbing body moving through it as though it were at zero temperature. The resulting gravitational drag in a superfluid can therefore become several orders of magnitude larger compared to a normal fluid with the same pressure forces. These results were applied to the Fornax dwarf spheroidal's (dSph) globular clusters (GC), under the assumption that the Fornax dSph is dominated by superfluid DM. Scalar field DM with sufficiently strong interactions to support the Fornax dSph's core through the interaction pressure alone results in large decay times for

the GCs' orbits that are consistent with observations. However, if the Fornax dSph core is not entirely supported by self-interactions, either because there is a thermal contribution to the DM hydrostatic pressure, or there is some other mechanism responsible for the core (both of which would suggest a lower value for the DM self-interaction strength), then linear theory suggests that the dynamical friction acting on the GCs due to the background DM superfluid is too large for the GCs' orbits to have survived for as long as they have, even for superfluid DM at finite-temperature where the thermal pressure can be much larger than the interaction pressure.

Paper III

In this paper we shifted our focus to zero-temperature scalar fields with self-interactions—the case usually considered in the literature, and that we refer to as SIBEC-DM—and tested how well large-scale observables constrains the self-interactions of the field. The scalar field was modeled as a perfect fluid with a time-dependent equation of state and sound speed specific to SIBEC-DM, describing the early radiation-like and late non-relativistic eras from refs. [77, 69], i.e. eq. (2.18) (similar to what was done in ref. [57] for an effective FDM equation of state and sound speed). The linear equations from cosmological perturbation theory with this equation of state were implemented into the Boltzmann code CLASS [12], and constraints on the self-interaction obtained with the Markov Chain Monte Carlo code MontePython [4, 17], using CMB temperature and polarization power spectra from the Planck 2018 data release [1], BAO and growth rate measurements from BOSS [2], and the Pantheon compilation of SNIa distances [122]. We found that a self-interaction corresponding to $R_c > 1\text{kpc}$, which is the parameter space generally considered necessary in order to explain the core-cusp problem in ΛCDM, to be ruled out at 2.4σ, or 98.5% confidence. The canonical parameter space for this kind of DM is therefore weakly ruled out by the large scale observables considered in this work, and complements the findings of ref. [124], in which the self-interacting scalar field DM halo mass function (HMF) was compared to observations, suggesting that R_c needs to be as low as 10pc to not overly suppress the observed abundance of halos.

Paper IV

In this paper we investigated the formation of structure in a universe with SIBEC-DM using fully 3D cosmological simulations. We implemented into the cosmological simulation code RAMSES a hydrodynamic approximation of the NLSE that includes the dynamics on the de Broglie

scale as an effective thermal energy, obtained by defining a phase space distribution function of the wavefunction that is smoothed at scales larger than the de Broglie wavelength. This smoothing yields a collisionless Boltzmann equation from which a set of hydrodynamic equations are derived [127, 150], which are computationally easier to solve compared to the full NLSE. This work is therefore a generalization of refs. [33, 124], in which the same approximation was used in spherically symmetric 1D simulations in order to investigate the collapse of SIBEC-DM overdensities and the resulting halos. Artificial initial conditions and parameters were used in Paper IV, since the realistic matter power spectrum from Paper III and ref. [124] requires both very large simulated volumes due to the strong suppression of power in SIBEC-DM, and very high resolution in order to resolve the halo cores. Despite these not-so-realistic initial conditions, the simulations run in Paper IV confirm many of the features expected from hydrostatic equilibrium and that found in ref. [124], such as SIBEC-DM cores that are only weakly dependent on the halo mass, the halo profiles transitioning to NFW envelopes near the core radius R_c, and the domination of effective thermal energy throughout the halos, despite the interaction energy initially being much larger. We also found that halo scaling relations, such as core density and mass versus halo mass, largely agree with simple analytic considerations assuming weak halo mass-scaling of the cores and velocity tracing in the envelope. These SIBEC-DM scaling relations also seem to generally agree better with observations than FDM-only simulations.

3.2 Outlook

The study of ULDM is an active area of research in cosmology, with different realizations and scenarios being developed in an effort to further our understanding of this kind of DM and how they might address shortcomings of the standard ΛCDM model. Although these models can often appear quite simple, with just one or two extra model parameters, they harbour a rich phenomenology that must be explored in detail in order to fully appreciate their effect on galactic and cosmological structures. This is an important endeavor for these models to be reliably tested against observational probes. Small-scale structures are of particular interest as future surveys such as the LSST and Euclid will conduct comprehensive galaxy surveys and provide improved data on e.g. the matter power spectrum on small scales, the distribution of DM in galaxies and clusters of galaxies, and upper limits on DM self-interactions [3, 62], all of which can be used to provide improved constraints on scalar field DM.

Our results in Papers I and II showed that in finite-temperature self-interacting scalar field DM, thermal counterflow can cause the DM superfluid to collapse as well as react to perturbations as though it were close to zero temperatures, thereby "screening" the effect of the thermal component of the DM fluid in some situations, which is very different from what might naively be expected if we use our intuition from conventional hydrodynamics for the self-interacting scalar field DM fluid. However, our calculations and simulations were performed in highly idealized scenarios, and might therefore not hold in more realistic setups. In particular, the thermal counterflow depends crucially on the superfluid critical velocity, which is likely exceeded at effectively lower velocities due to turbulence, which will require fully 3D simulations to resolve.

In Paper III we used large-scale observables to obtain constraints on the self-interaction of scalar field DM, and showed that the self-coupling strength generally found to be needed in order to produce the DM halo cores implied by rotation velocity curves [151, 29] is not compatible with these large-scale observables. This is the same conclusion drawn by other recent work, using the HMF of SIBEC-DM halos [124]. These constraints pose a challenge for SIBEC-DM, hence further study is warranted in order to validate these results and to find even stronger tests. This was the aim of Paper IV, in which we generalized the 1D simulations of refs. [33] and [124] to 3D, and we confirmed many of the halo features found in these works. Intriguingly, we also found SIBEC-DM halo scaling relations that generally fit the data better than FDM-only simulations. However, due to the large computational cost of our simulations, a hydrodynamic approximation of the NLSE was used, as well as relatively small simulated domains and artificial initial conditions that are incompatible with a realistic cosmic history for self-interacting scalar field DM. Further work is therefore needed in this direction in order to produce results that represent realistic cosmological realizations of SIBEC-DM that can be used to reliably test against observables such as the HMF, the Ly-α forest, rotation curves, and weak and strong lensing.

Papers

Paper I

Collapse of spherical overdensities in superfluid models of dark matter

Stian T. H. Hartman, Hans A. Winther, David F. Mota

Published in *Astronomy & Astrophysics*, July 2020, volume 639, A90,
DOI: 10.1051/0004-6361/201937263. arXiv: 1911.11498.

A&A 639, A90 (2020)
https://doi.org/10.1051/0004-6361/201937263

Astronomy & Astrophysics

Collapse of spherical overdensities in superfluid models of dark matter

S. T. H. Hartman, H. A. Winther, and D. F. Mota

Institute of Theoretical Astrophysics, University of Oslo, PO Box 1029, Blindern 0315, Oslo, Norway
e-mail: stian.hartman@gmail.com

Received 5 December 2019 / Accepted 7 May 2020

ABSTRACT

Aims. We intend to understand cosmological structure formation within the framework of superfluid models of dark matter with finite temperatures. Of particular interest is the evolution of small-scale structures where the pressure and superfluid properties of the dark matter fluid are prominent. We compare the growth of structures in these models with the standard cold dark matter paradigm and non-superfluid dark matter.

Methods. The equations for superfluid hydrodynamics were computed numerically in an expanding ΛCDM background with spherical symmetry; the effect of various superfluid fractions, temperatures, interactions, and masses on the collapse of structures was taken into consideration. We derived the linear perturbation of the superfluid equations, giving further insights into the dynamics of the superfluid collapse.

Results. We found that while a conventional dark matter fluid with self-interactions and finite temperatures experiences a suppression in the growth of structures on smaller scales, as expected due to the presence of pressure terms, a superfluid can collapse much more efficiently than was naively expected due to its ability to suppress the growth of entropy perturbations and thus gradients in the thermal pressure. We also found that the cores of the dark matter halos initially become more superfluid during the collapse, but eventually reach a point where the superfluid fraction falls sharply. The formation of superfluid dark matter halos surrounded by a normal fluid dark matter background is therefore disfavored by the present work.

Key words. cosmology: theory – dark matter – large-scale structure of Universe

1. Introduction

A universe with cold dark matter (CDM), a cosmological constant (Λ), and inflationary initial conditions forms the foundation of the standard ΛCDM paradigm that has proven successful at explaining a wide range of observables, such as the expansion history of the universe, the cosmic microwave background, formation of large-scale structure, the matter power spectra, and the abundance of light elements (Tegmark et al. 2004; Planck Collaboration XIII 2016; Cyburt et al. 2016). Nonetheless, it is a phenomenological model that is ignorant of the origin of the cosmological constant and the identity of dark matter (DM), which remain two of the greatest mysteries in fundamental physics today.

A number of challenges to ΛCDM have emerged as both observations and numerical simulations become increasingly more precise, especially on small scales. The cores of DM halos predicted from N-body simulations are denser and more cuspy than observed, and the number of dwarf galaxies in the Local Group is far smaller than expected from pure ΛCDM simulations. These issues are known as the too-big-to-fail, cusp-core, and missing satellite problems (see e.g., Del Popolo & Le Delliou 2017; Bullock & Boylan-Kolchin 2017 and references therein). Another puzzling phenomenology on the scale of galaxies is the empirical baryonic Tully-Fisher relation (BTFR; McGaugh et al. 2000; McGaugh 2005; Lelli et al. 2015). This relates the baryonic mass of galaxies M_b with the asymptotic circular velocity v_c through $M_\mathrm{b} \sim v_\mathrm{c}^4$ and holds for many orders of magnitude with remarkably small scatter. The ΛCDM prediction for this relation is $M \sim v_\mathrm{c}^3$ with the total mass M from both baryons and DM (McGaugh 2012). It is the latter that dominates the gravitational pull in galaxies, which only adds to the strangeness of the BTFR.

Solutions to these problems within the framework of ΛCDM have been proposed by including baryonic physics (Santos-Santos et al. 2015; Sales et al. 2016; Zhu et al. 2016; Sawala et al. 2016), but it is unclear if they can completely cure the ails of ΛCDM. These processes are not yet fully understood and are difficult to model in simulations of galaxy formation, and their stochastic nature makes it even more puzzling as to how they can be responsible for the tight correlation in scaling relations, such as the BTFR.

An alternative possibility is that the mismatch between observations and simulations is an indication of physics beyond the standard model, either through modified theories of gravity, the particle nature of DM, or both. An example of such a model is modified Newtonian dynamics (MOND; Milgrom 1983a,b,c; Famaey & McGaugh 2012), in which the Newtonian law of gravity in low-acceleration regions is modified to explain the rotation curves of galaxies without the need of resorting to DM. One of its most appealing features is that the BTFR and its small scatter is a direct consequence of it. However, MOND and its relativistic extensions face challenges of their own on extragalactic scales where the CDM paradigm is successful (Zuntz et al. 2010; Dodelson 2011; Angus et al. 2013, 2014). This has, somewhat ironically, motivated extended models of DM where MOND is an emergent fifth force on small scales (Berezhiani & Khoury 2015; Khoury 2016). This is achieved by DM undergoing

Bose–Einstein condensation on galactic scales and adding a coupling designed to give a MONDian long-range force between baryons mediated by phonons in the superfluid cores of galaxies. Outside galaxies, the DM fluid ceases to be superfluid, and the extra force disappears, preserving the success of CDM on large scales.

Superfluid dark matter (SFDM) models are also interesting on more general grounds. From condensed matter physics, we know that self-interacting boson gases can become superfluid given sufficiently high densities and low temperatures. In the weakly interacting Bose gas, the critical temperature that marks the onset of superfluidity depends almost solely on the particle mass and number density. We can therefore expect boson DM candidates with self-interactions to exhibit superfluid behavior in certain mass ranges.

Observations of the large-scale structure of the universe strongly favor cold and collisionless DM, but for SFDM this is no longer the case since the transition in and out of the superfluid phase requires both self-interactions and finite temperatures. We must therefore be wary of how structure forms in SFDM. Studies of other DM models with pressure-like terms, such as fuzzy dark matter (Hu et al. 2000; Schive et al. 2014; Schwabe et al. 2016; Mocz et al. 2017) and self-interacting dark matter (Spergel & Steinhardt 2000; Elbert et al. 2015; Tulin & Yu 2018), find they can help remove the surplus of small-scale structure in ΛCDM. So far, there has been little work done on structure formation in SFDM and how it differs from conventional DM fluids. In this paper, we aim to provide preliminary answers to these questions by considering the spherical collapse of SFDM.

The paper is organized as follows: in Sect. 2, the equations for superfluid hydrodynamics used to describe the collapse of SFDM are introduced, as well as the critical temperature and the critical velocity, which are important for the superfluid phenomenology. The linear expansion of the superfluid equations was derived to better understand how superfluidity changes the behavior of the DM fluid. In Sect. 3, the results are presented and discussed, and we draw our conclusions in Sect. 4.

2. Method

2.1. Superfluid hydrodynamics

To describe a finite-temperature superfluid, we employed the superfluid hydrodynamic equations (Taylor & Griffin 2005; Chapman et al. 2014), which in proper coordinates and physical variables are;

$$\frac{\partial \rho}{\partial t} + \boldsymbol{\nabla} \cdot \boldsymbol{j} = 0, \tag{1}$$

$$\frac{\partial S}{\partial t} + \boldsymbol{\nabla} \cdot (S \boldsymbol{u}_{\rm n}) = 0, \tag{2}$$

$$\frac{\partial \boldsymbol{u}_{\rm s}}{\partial t} + \boldsymbol{\nabla}\left(\mu + \frac{1}{2}\boldsymbol{u}_{\rm s}^2\right) = -\boldsymbol{\nabla}\Phi, \tag{3}$$

$$\frac{\partial \boldsymbol{j}}{\partial t} + \boldsymbol{\nabla} P + \rho_{\rm s}(\boldsymbol{u}_{\rm s} \cdot \boldsymbol{\nabla})\boldsymbol{u}_{\rm s} + \rho_{\rm n}(\boldsymbol{u}_{\rm n} \cdot \boldsymbol{\nabla})\boldsymbol{u}_{\rm n} + \boldsymbol{u}_{\rm s}[\boldsymbol{\nabla} \cdot (\rho_{\rm s}\boldsymbol{u}_{\rm s})] + \boldsymbol{u}_{\rm n}[\boldsymbol{\nabla} \cdot (\rho_{\rm n}\boldsymbol{u}_{\rm n})] = -\rho \boldsymbol{\nabla}\Phi, \tag{4}$$

$$\frac{\partial E}{\partial t} + \boldsymbol{\nabla} \cdot \left[\left(U + \frac{1}{2}\rho_{\rm n}u_{\rm n}^2 + P\right)\boldsymbol{u}_{\rm n} + \frac{1}{2}\rho_{\rm s}u_{\rm s}^2\boldsymbol{u}_{\rm s} + \mu\rho_{\rm s}(\boldsymbol{u}_{\rm s} - \boldsymbol{u}_{\rm n})\right] = -\boldsymbol{j} \cdot \boldsymbol{\nabla}\Phi. \tag{5}$$

This set of equations describes the evolution of the fluid mass density ρ, entropy density S, superfluid velocity $\boldsymbol{u}_{\rm s}$, momentum density $\boldsymbol{j}$, and energy density E under the influence of the gravitational potential Φ sourced by matter and a cosmological constant,

$$\nabla^2\Phi = 4\pi G(\rho - 2\rho_\Lambda). \tag{6}$$

Equations (2) and (5) are degenerate in our set of equations if the solution is free of shocks, otherwise entropy is generated. The former is used in this work, but both are given for completeness.

A superfluid differs from a classical fluid in that it consists of two fluid components; the "superfluid" with density $\rho_{\rm s}$ and velocity $\boldsymbol{u}_{\rm s}$, and the "normal fluid" with density $\rho_{\rm n}$ and velocity $\boldsymbol{u}_{\rm n}$. The sum of the two component densities gives the total fluid density $\rho = \rho_{\rm n} + \rho_{\rm s}$, and likewise for momentum, $\boldsymbol{j} = \rho_{\rm n}\boldsymbol{u}_{\rm n} + \rho_{\rm s}\boldsymbol{u}_{\rm s}$. However, only the normal fluid transports entropy and thermal energy, as can be seen from Eqs. (2) and (5), and the superfluid velocity evolves according to its own potential given in Eq. (3), where the chemical potential is $\mu = [P + U - ST - \frac{1}{2}\rho_n(\boldsymbol{u}_{\rm s} - \boldsymbol{u}_{\rm n})^2]/\rho$. Since there are two fluid components with separate velocity fields a superfluid can have two sound modes. One is called first sound and is associated with density perturbations, which we are familiar with from regular hydrodynamics. The other is called second sound and is associated with temperature perturbations. This is made possible by the fact that only the normal component carries entropy, hence the normal and superfluid components can oscillate in such a way that perturbations in temperature, and not density, are propagated through the fluid. As we will see it is this property that is responsible for the difference in collapse of superfluid and non-superfluid DM.

The remaining variables in the above set of equations are pressure P, internal energy density U, and temperature T. In the limit $\rho_{\rm s} = 0$, they reduce to the Euler equations of fluid dynamics.

2.2. Critical temperature and velocity, and equation of state

When a boson gas is cooled below a critical temperature $T_{\rm c}$, the particles begin accumulating in the quantum ground state of the system and form a Bose–Einstein condensate (BEC). In the three-dimensional homogeneous and ideal Bose gas this critical temperature is

$$T_{\rm c} = \frac{2\pi\hbar^2}{m^{5/3}k_{\rm B}}\left(\frac{\rho}{\zeta(3/2)}\right)^{2/3}, \tag{7}$$

where $\zeta(x)$ is the Riemann Zeta-function. This result holds approximately for weakly interacting gases as well (Sharma et al. 2019), apart from a small interaction-dependent shift (Andersen 2004) that we neglect.

The formation of a BEC does not automatically imply a superfluid. A further criterion must be satisfied as realized by Landau (1941). He assumed that if dissipation and heating happens through the creation of elementary excitations in the fluid, and if these excitations can no longer spontaneously appear the fluid will become superfluid. This gives the so-called Landau criterion and requires the relative motion $\boldsymbol{w} = \boldsymbol{u}_{\rm s} - \boldsymbol{u}_{\rm n}$ to be smaller than the critical velocity $v_{\rm c}$,

$$w < v_{\rm c} = \min_{p} \frac{\epsilon(\boldsymbol{p})}{p}, \tag{8}$$

where $\epsilon(\boldsymbol{p})$ is the energy of an elementary excitation with momentum $\boldsymbol{p}$. Clearly, we must have $v_{\rm c} > 0$, otherwise any motion will destroy the superflow, and it no longer makes sense

to refer to it as a superfluid. An ideal Bose gas can therefore not be superfluid since the elementary excitations are $\epsilon(\boldsymbol{p}) = p^2/2m$ so that $v_c = 0$. In an interacting Bose gas, on the other hand, the condensation of the gas makes the energy spectrum phonon-like at small momenta, $\epsilon(\boldsymbol{p}) = c_s p$. The critical velocity is in this case finite, $v_c = c_s$, and we get superfluidity.

As w approaches and exceeds the critical velocity, the superfluid flow begins to decay. This happens because a tangle of superfluid vortices, so-called quantum turbulence, forms and interacts with the excitations that make up the normal fluid, resulting in a dissipative mutual friction between the normal and superfluid components (Skrbek 2011; Skrbek & Sreenivasan 2012; Barenghi et al. 2014). This effect is not included in the equations for superfluid hydrodynamics and must be added through additional terms. However, this would require us to assume the dependence of this force on the fluid variables and specify the extra parameters introduced to our model (for examples of this in numerical studies of superfluid helium, see Doi et al. 2008; Darve et al. 2012; Soulaine et al. 2017). To capture the basic consequence of Landau's criterion relevant for this work, which is that the counterflow w is limited by the critical velocity, we instead assume the mutual friction only takes place once the critical velocity is exceeded, and that the complicated processes taking place happen on time and length scales much shorter than we are considering. The mutual friction is therefore effectively instantaneous, and since it is dissipative, there is a conversion of kinetic energy into internal energy, heating the fluid and generating entropy. Stated more precisely, we enforce the superfluid critical velocity at every position in our numerical scheme by converting kinetic energy of the two fluid components (while conserving the total momentum) into internal energy and generated entropy so that $w < v_c$ is always satisfied. See Appendix B.3 for further details.

We must also specify the equation of state (EOS) that defines how the thermodynamic quantities depend on the temperature and particle density. In superfluids, the EOS is also a function of the counterflow w (Landau & Lifshitz 1987; Khalatnikov 2000), but we neglected this dependence and used the EOS corresponding to the $w = 0$ limit. While this work is motivated by the superfluid DM model presented by Berezhiani & Khoury (2015), it lacks a complete EOS at finite temperatures. We therefore employed the weakly interacting Bose gas with effective repulsive two- and three-body contact interactions as described by Sharma et al. (2019), where the three-body case corresponds most closely to the model by Berezhiani & Khoury (2015). Effective contact interactions can describe the s-wave scattering limit of more complicated interactions through the Born approximation, which makes this class of models a more general description of superfluids (Pethick & Smith 2008). The coupling term between the DM fluid and baryons that gives rise to the emergent fifth force is not included in this work. For computational speed, we approximated the EOS in the sub-T_c regime by an ideal Bose gas with contributions from interactions at zero temperature. Notably, the superfluid fraction is approximated as the fraction of condensed particles in an ideal BEC, $f_s = \rho_s/\rho = 1 - (T/T_c)^{3/2}$. This might appear paradoxical since we already stated that an ideal Bose gas cannot be superfluid, but in the weakly interacting gas these quantities can be seen from Fig. 1 to be closely related. For strong interactions, the superfluid fraction can approach unity while the condensate fraction remains small, which is the case in superfluid ^{4}He (Glyde 2013), but this scenario is outside the scope of this paper. See Appendix A for further details on the EOS.

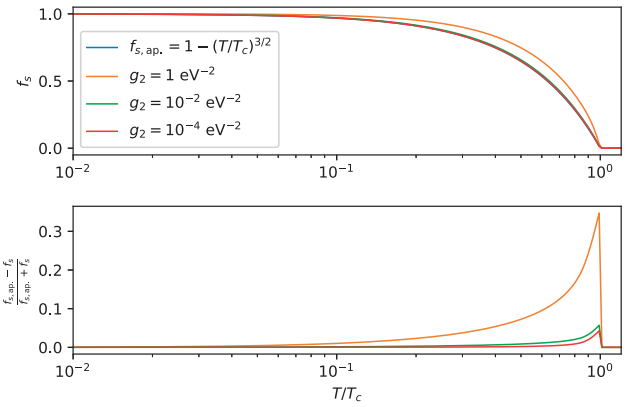

Fig. 1. Superfluid fraction f_s for the two-body interacting Bose gas calculated by Sharma et al. (2019) with $\rho = 10^8 \rho_{c0}$ and $m = 1$ eV compared to the approximation $f_{s,\mathrm{ap.}} = 1 - (T/T_c)^{3/2}$. For sufficiently weak interactions, f_s can be approximated by the condensate fraction in an ideal Bose gas.

2.3. Super-comoving variables

Since we are interested in the evolution of the superfluid in an expanding space, we introduce the peculiar velocity $\boldsymbol{v} = \boldsymbol{u} - H\boldsymbol{r}$ and super-comoving variables (Martel & Shapiro 1998), denoted by a tilde-sign, to rewrite the hydrodynamic equations in a more convenient form[1]:

$$\frac{\partial \tilde{\rho}}{\partial \tilde{t}} + \tilde{\boldsymbol{\nabla}} \cdot \tilde{\boldsymbol{j}} = 0, \tag{9}$$

$$\frac{\partial \tilde{S}}{\partial \tilde{t}} + \tilde{\boldsymbol{\nabla}} \cdot (\tilde{S}\tilde{\boldsymbol{v}}_n) = 0, \tag{10}$$

$$\frac{\partial \tilde{\boldsymbol{v}}_s}{\partial \tilde{t}} + \tilde{\boldsymbol{\nabla}}\left(\tilde{\mu} + \frac{1}{2}\tilde{\boldsymbol{v}}_s^2\right) = -\tilde{\boldsymbol{\nabla}}\tilde{\phi}, \tag{11}$$

$$\begin{aligned}\frac{\partial \tilde{\boldsymbol{j}}}{\partial \tilde{t}} &+ \tilde{\boldsymbol{\nabla}}\tilde{P} + \tilde{\rho}_s(\tilde{\boldsymbol{v}}_s \cdot \tilde{\boldsymbol{\nabla}})\tilde{\boldsymbol{v}}_s + \tilde{\rho}_n(\tilde{\boldsymbol{v}}_n \cdot \tilde{\boldsymbol{\nabla}})\tilde{\boldsymbol{v}}_n \\ &+ \tilde{\boldsymbol{v}}_s[\tilde{\boldsymbol{\nabla}} \cdot (\tilde{\rho}_s\tilde{\boldsymbol{v}}_s)] + \tilde{\boldsymbol{v}}_n[\tilde{\boldsymbol{\nabla}} \cdot (\tilde{\rho}_n\tilde{\boldsymbol{v}}_n)] = -\tilde{\rho}\tilde{\boldsymbol{\nabla}}\tilde{\phi},\end{aligned} \tag{12}$$

$$\begin{aligned}\frac{\partial \tilde{E}}{\partial \tilde{t}} &+ \tilde{\boldsymbol{\nabla}} \cdot \left[\left(\tilde{U} + \frac{1}{2}\tilde{\rho}_n\tilde{v}_n^2 + \tilde{P}\right)\tilde{\boldsymbol{v}}_n + \frac{1}{2}\tilde{\rho}_s\tilde{v}_s^2\tilde{\boldsymbol{v}}_s \right. \\ &\left. + \tilde{\mu}\tilde{\rho}_s(\tilde{\boldsymbol{v}}_s - \tilde{\boldsymbol{v}}_n)\right] = -\tilde{H}(3\tilde{P} - 2\tilde{U}) - \tilde{\boldsymbol{j}} \cdot \tilde{\boldsymbol{\nabla}}\tilde{\phi}.\end{aligned} \tag{13}$$

The super-comoving quantities are re-scaled to reduce the dependence on the scale factor a, with the variables defined as before: $\tilde{\boldsymbol{j}} = \tilde{\rho}_n\tilde{\boldsymbol{v}}_n + \tilde{\rho}_s\tilde{\boldsymbol{v}}_s$ and $\tilde{E} = \tilde{U} + \frac{1}{2}\tilde{\rho}_n\tilde{v}_n^2 + \frac{1}{2}\tilde{\rho}_s\tilde{v}_s^2$. The only real difference is the peculiar gravitational potential $\tilde{\phi}$ that is now given by (in a flat universe with matter and a cosmological constant)

$$\tilde{\nabla}^2\tilde{\phi} = 6a(\tilde{\rho} - 1). \tag{14}$$

$\tilde{H}$ is the super-comoving Hubble parameter.

2.4. Linear perturbation expansion

The superfluid hydrodynamic equations at linear order can tell us a lot about the collapse of a superfluid, in particular how it

[1] The temperature and entropy in super-comoving variables are not given in Martel & Shapiro (1998, MS). We define them here as $\tilde{T} = a^2T/T_*$ and $\tilde{S} = a^3S/S_*$, where T_* is a free parameter, $S_* = \rho_* v_*^2/T_*$, with ρ_* and v_* given in MS.

will differ from CDM and non-superfluid thermal DM. The fluid variables are expanded around their background values, $\tilde{\rho} = \tilde{\rho}_0 + \delta\tilde{\rho}$, $\tilde{S} = \tilde{S}_0 + \delta\tilde{S}$, etc. The peculiar background velocities are zero, so $\tilde{\boldsymbol{v}}_s = \delta\tilde{\boldsymbol{v}}_s$, $\tilde{\boldsymbol{v}}_n = \delta\tilde{\boldsymbol{v}}_n$, and $\tilde{\boldsymbol{j}} = \delta\tilde{\boldsymbol{j}}$. We also have $\tilde{\nabla}^2\delta\tilde{\phi} = 6a\delta\tilde{\rho}$. This gives the following linear equations;

$$\frac{\partial\delta\tilde{\rho}}{\partial\tilde{t}} + \tilde{\boldsymbol{\nabla}}\cdot\delta\tilde{\boldsymbol{j}} = 0, \tag{15}$$

$$\frac{\partial\delta\tilde{S}}{\partial\tilde{t}} + \tilde{S}_0\tilde{\boldsymbol{\nabla}}\cdot\delta\tilde{\boldsymbol{v}}_n = 0, \tag{16}$$

$$\frac{\partial\delta\tilde{\boldsymbol{v}}_s}{\partial\tilde{t}} + \tilde{\boldsymbol{\nabla}}(\delta\tilde{\mu} + \delta\tilde{\phi}) = \boldsymbol{0}, \tag{17}$$

$$\frac{\partial\delta\tilde{\boldsymbol{j}}}{\partial\tilde{t}} + \tilde{\boldsymbol{\nabla}}\delta\tilde{P} + \tilde{\rho}_0\tilde{\boldsymbol{\nabla}}\delta\tilde{\phi} = \boldsymbol{0}. \tag{18}$$

These can be combined into two coupled equations for $\delta\tilde{\rho}$ and $\delta\tilde{S}$ in $\tilde{k}$-space;

$$\frac{\partial^2\delta\tilde{\rho}_{\tilde{k}}}{\partial\tilde{t}^2} + \left[\left(\frac{\partial\tilde{P}}{\partial\tilde{\rho}}\right)_0\tilde{k}^2 - 6a\tilde{\rho}_0\right]\delta\tilde{\rho}_{\tilde{k}} + \left(\frac{\partial\tilde{P}}{\partial\tilde{S}}\right)_0\tilde{k}^2\delta\tilde{S}_{\tilde{k}} = 0, \tag{19}$$

$$\begin{aligned}\frac{\partial^2\delta\tilde{S}_{\tilde{k}}}{\partial\tilde{t}^2} &+ \tilde{S}_0\left[\left\{\frac{1}{\tilde{\rho}_0}\left(\frac{\partial\tilde{P}}{\partial\tilde{\rho}}\right)_0 + \frac{\tilde{S}_0\tilde{\rho}_{s0}}{\tilde{\rho}_0\tilde{\rho}_{n0}}\left(\frac{\partial\tilde{T}}{\partial\tilde{\rho}}\right)_0\right\}\tilde{k}^2 - 6a\right]\delta\tilde{\rho}_{\tilde{k}} \\ &+ \tilde{S}_0\left[\frac{1}{\tilde{\rho}_0}\left(\frac{\partial\tilde{P}}{\partial\tilde{S}}\right)_0 + \frac{\tilde{S}_0\tilde{\rho}_{s0}}{\tilde{\rho}_0\tilde{\rho}_{n0}}\left(\frac{\partial\tilde{T}}{\partial\tilde{S}}\right)_0\right]\tilde{k}^2\delta\tilde{S}_{\tilde{k}} = 0,\end{aligned} \tag{20}$$

where the subscript "0" indicates the background values.

We would like to enforce the critical velocity in the linear approach, though we cannot do it in the same way as for the full hydrodynamic equations. Since the effect of the critical velocity is to essentially restrict the two-fluid nature of the superfluid, forcing the whole fluid to evolve like a normal fluid, we can, as a rough approximation, set $\rho_s = 0$ and $\rho_n = \rho$ once $\tilde{w}_{\tilde{k}} \geq \tilde{v}_c$, where $\tilde{w}_{\tilde{k}}$ is the relative velocity of mode $\tilde{k}$ and evolves at linear order according to

$$\frac{\partial\tilde{w}_{\tilde{k}}}{\partial\tilde{t}} = \tilde{k}\frac{\tilde{S}_0}{\tilde{\rho}_{n0}}\left[\left(\frac{\partial\tilde{T}}{\partial\tilde{\rho}}\right)_0\delta\tilde{\rho}_{\tilde{k}} + \left(\frac{\partial\tilde{T}}{\partial\tilde{S}}\right)_0\delta\tilde{S}_{\tilde{k}}\right]. \tag{21}$$

This approximation is further justified by the fact that the critical velocity decreases with the DM density. Once w reaches v_c, it only becomes smaller in the linear regime, forcing the superfluid to behave even more like a normal fluid.

A few qualitative statements can be made from Eqs. (19) and (20). Both mass density and entropy perturbations grow due to gravity, but this growth is slowed by pressure terms that are scale dependent through the $\tilde{k}^2$ factor, as expected in a self-gravitating fluid with nonzero pressure. In a superfluid, however, there are additional effective pressure terms that suppress the growth of entropy perturbations, and hence thermal pressure, that are absent in conventional fluids. This in turn allows the mass density perturbations to collapse more efficiently, even though the DM fluid may have relatively high temperatures. The reason for this behavior is the superfluid component's attraction to higher temperatures. The normal component tends to transport mass and entropy from hot to cold regions, while the superfluid tends to flow in the opposite direction and balance the mass-loss due to the normal component, resulting in a thermal flux that can be large compared to the net mass flux. This effect, called thermal counterflow, makes superfluids very efficient at conducting heat.

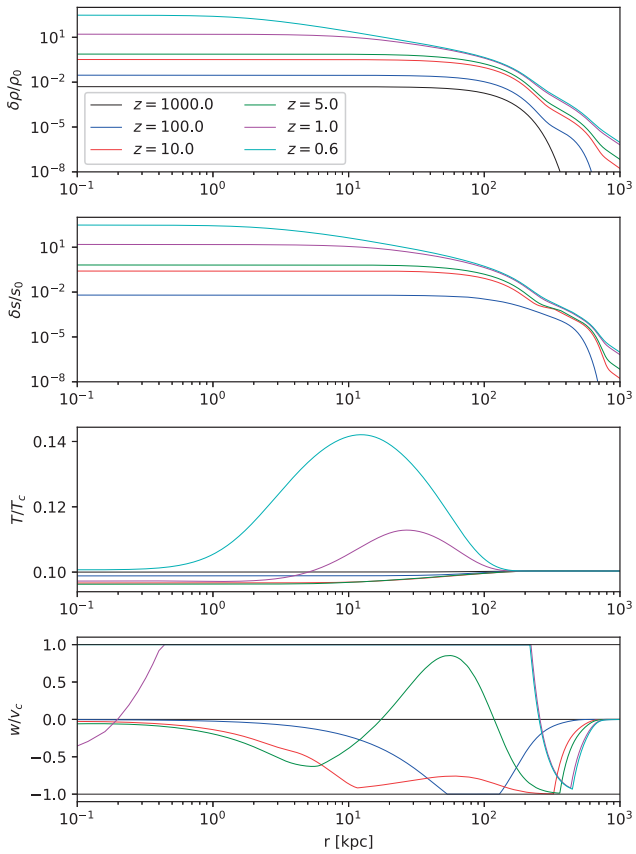

Fig. 2. Profiles of a collapsing SFDM halo with an initial Gaussian density contrast, $m = 30\,\mathrm{eV}$, $g = 10^{-5}\,\mathrm{eV}^{-2}$, $L = 100\,\mathrm{kpc}$, and $T/T_c = 0.1$. A thermal counterflow develops and the growth of entropy perturbations is at first suppressed. This also gives a slight decrease in the ratio T/T_c, and hence the superfluid fraction, since $f_s = \rho_s/\rho = 1-(T/T_c)^{3/2}$. As the critical velocity is reached, entropy is generated, and T/T_c increases.

3. Results and discussion

The hydrodynamic equations were integrated numerically using a modified first-order FORCE scheme (see Toro 2006 and Appendix B for further details) for a spherically symmetric system with an initial density contrast of the form $\delta\tilde{\rho}/\tilde{\rho}_0 = \Delta_0 e^{-(\tilde{r}/\tilde{L})^2}$ and $\delta\tilde{S} = 0$, where $\tilde{L}$ is the size of the overdensity. The initial state is at approximately the same T/T_c, and hence the same mixing fraction of the normal and superfluid components, throughout the system. A flat ΛCDM background cosmology with $\Omega_{m0} = 0.3$, $\Omega_{\Lambda 0} = 0.7$, and $h = 0.7$ was used, and the integration started at redshift $z = 1000$ with $\Delta_0 = 5\times10^{-3}$. An example of a collapsing SFDM halo at various redshifts can be seen in Fig. 2, illustrating that as the halo collapses, a thermal counterflow carrying entropy away from the halo center develops, slowing down the growth of entropy until the critical velocity is reached and the fluid starts heating up.

3.1. Growth of structure

In Figs. 3–5, the redshift when the central density contrast reaches 200 is shown for various parameters for both the superfluid and non-superfluid (a conventional fluid with $\rho_s = 0$, $\rho_n = \rho$, and the same EOS) cases. While the growth of structure is slower compared to CDM, the SFDM halos collapse more efficiently than their non-superfluid counterparts as the interaction

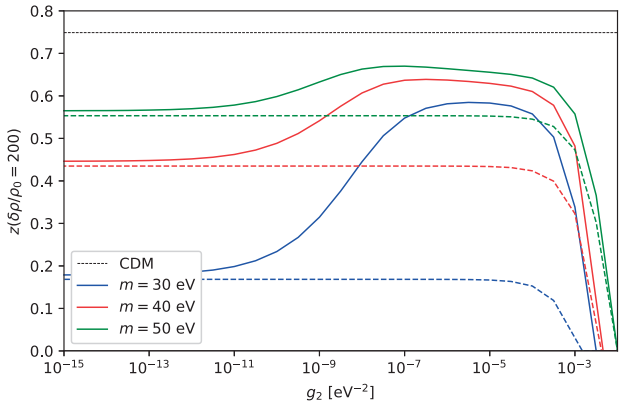

Fig. 3. Comparison of redshifts when the central density contrast reaches 200 as function of the interaction strength for various particle masses, with $T/T_c = 0.1$ and $L = 100$ kpc. Both the superfluid case (solid lines) and the corresponding non-superfluid case (striped lines) are shown. For constant T/T_c, the temperature is increased for decreasing mass, since $T_c \sim m^{-5/3}$. The comparison of the collapse for various masses is therefore not done at the same temperature, but instead at a similar place in the superfluid phase.

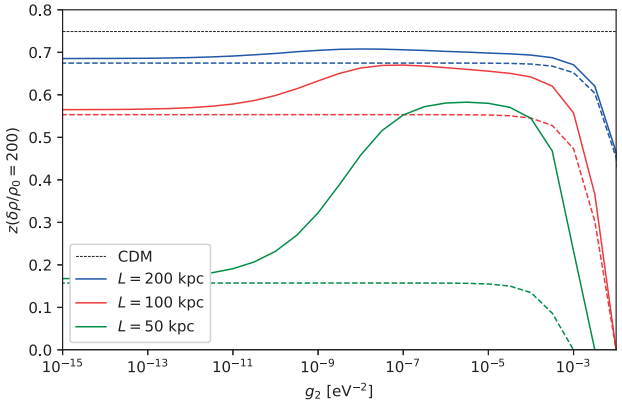

Fig. 4. Comparison of redshifts when the central density contrast reaches 200 as function of the interaction strength for various scales, with $T/T_c = 0.1$ and $m = 50$ eV. Both the superfluid case (solid lines) and the corresponding non-superfluid case (striped lines) are shown.

strength is increased until a maximum is reached, after which the growth of structure in both super-and non-superfluid DM is suppressed. This is counter to what one would intuitively expect, since an increase in interactions also means an increase in pressure. It can, however, be understood as follows: for small interactions, the superfluid behaves nearly the same as a normal fluid because the critical velocity, which scales as $v_c \sim \sqrt{g_i}$, is reached very early. When this happens, the flow of the normal and superfluid components become "locked" to one another, unable to efficiently conduct heat away from the halo core. As the interaction increases, the thermal counterflow can both be larger and last longer, resulting in an increased suppression of thermal gradients and thus allows for a faster collapse. For sufficiently large interactions, the collapse is instead suppressed due to large zero-temperature pressure gradients that the superfluid is unable to wash out.

Most production of entropy due to mutual friction as the Landau criterion is broken takes place away from the center of the halo. The resulting extra thermal pressure acting on the interior causes the central density contrast to grow slightly faster and can best be seen by the gap between collapse times of the superfluid and non-superfluid cases at low g_2. If entropy was not produced, this gap would vanish.

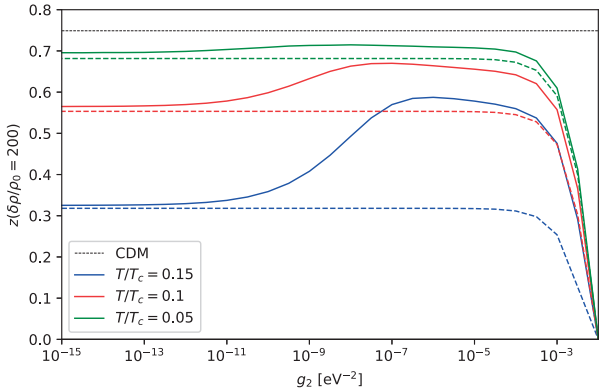

Fig. 5. Comparison of redshifts when the central density contrast reaches 200 as function of the interaction strength for various temperatures, with $m = 50$ eV and $L = 100$ kpc. Both the superfluid case (solid lines) and the corresponding non-superfluid case (striped lines) are shown.

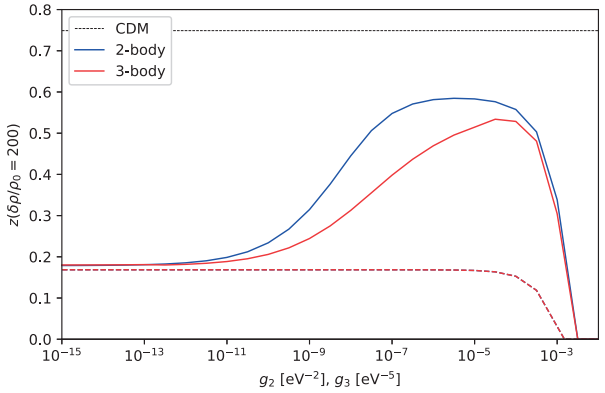

Fig. 6. Comparison of redshifts when the central density contrast reaches 200 for two-body and three-body interactions as function of the interaction strengths g_2 and g_3, respectively, with $m = 30$ eV, $L = 100$ kpc, and $T/T_c = 0.1$. The three-body interaction is multiplied by $\sqrt{10} \times 10^{-4}$ to make the comparison clearer. Both the superfluid case (solid lines) and the non-superfluid (striped lines) are shown.

3.2. Dependence on equation of state

The Bose gas with two-body interactions is compared with three-body interactions in Fig. 6. The same qualitative behavior is present in both cases and is expected to be a general feature regardless of the EOS used, as long as there is superfluidity. In the linear expansion of the superfluid equations, Eqs. (19) and (20), the additional effective pressure terms due to a superfluid component require only the temperature to be dependent on mass density or entropy. Indeed, the approximated two-body and three-body EOS used in this work both have a temperature profile that is independent of mass density for $T < T_c$, so that one of the effective pressure terms in Eq. (20) is absent. For EOS where the temperature is dependent on both the mass density and entropy, the collapse of SFDM may be even more efficient.

3.3. Effect of small-scale and nonradial motion

In this work, we assumed perfect radial infall of DM. The relative velocity w is simply the difference between the radial

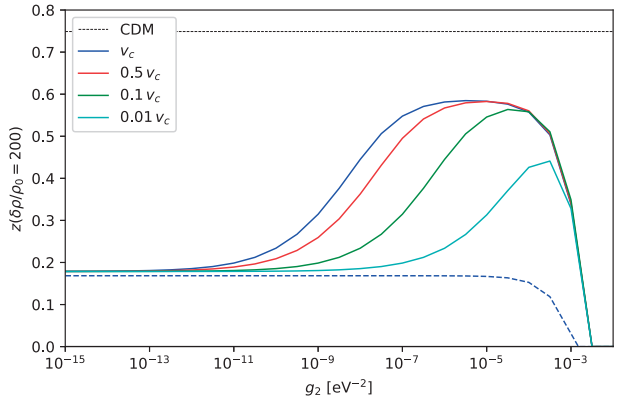

Fig. 7. Comparison of redshifts when the central density contrast reaches 200 for various effective critical velocities as function of the interaction strength, with $m = 30\,\mathrm{eV}$, $T/T_c = 0.1$, and $L = 100\,\mathrm{kpc}$. Both the superfluid case (solid lines) and the non-superfluid (striped line) are shown.

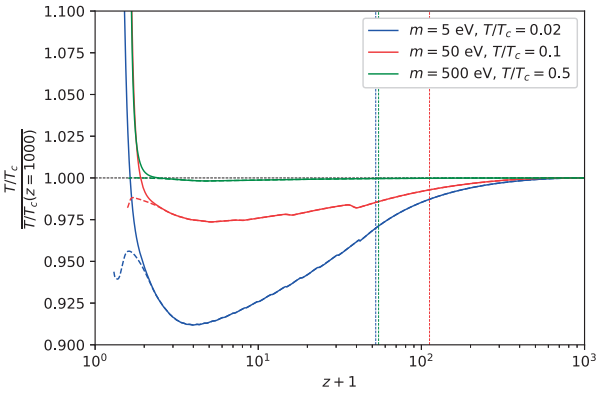

Fig. 8. Evolution of T/T_c in the halo center during collapse for various masses and initial temperatures with $g = 10^{-5}\,\mathrm{eV}^{-2}$ and $L = 100\,\mathrm{kpc}$. Both the evolution with entropy production (solid lines) and without (striped lines) are shown until the overdensity reach 10^5. The two cases differ only in the end stage of the collapse, well after the critical velocity is first reached, indicated by the colored vertical lines.

velocities of the two fluid components. In a real system, there is expected to be additional small-scale motion in all directions, such as turbulence that our simplified model averages over. The superfluid critical velocity may therefore be exceeded on small scales, while the large-scale radial average only appears to have $w < v_c$. In this case, the superfluid would behave like a conventional fluid at much smaller w. In other words, there is an effective superfluid critical velocity $v_c^{\mathrm{eff}} < v_c$ that is a decreasing function of the local turbulence. This leads to a difference in collapse times of halos with different amounts of turbulence, the turbulent ones collapsing at a slower rate, as seen in Fig. 7.

3.4. Evolution of superfluid fraction

In a conventional fluid, the entropy and mass density collapses at the same rate so that the ratio T/T_c is constant. A fluid that is initially in the normal phase will therefore remain so. A collapsing superfluid, on the other hand, experiences an increase in the superfluid fraction due to thermal counterflow until the critical velocity is reached. At this point, entropy is generated causing T/T_c to rise, and thus the superfluid fraction to fall; though it takes time for the full effect of this to propagate to the center of the halo, as shown in Figs. 2 and 8. It may be, however, that Eqs. (1)–(5) do not properly describe super-critical flow, and too much entropy is generated in our numerical scheme for enforcing the critical velocity. The evolution of T/T_c when no entropy is generated is therefore also shown in Fig. 8 as the opposite extreme. This case behaves similarly until near the end of the collapse, where T/T_c rises only modestly. Profiles are shown in Fig. 9, which corresponds to Fig. 2 with no production of entropy.

The decrease in T/T_c during collapse becomes smaller as the temperature approaches T_c, where the superfluid fraction goes to zero and thermal counterflow becomes inefficient. The formation of DM halos with much higher superfluid fractions than the background, as required in the emergent MOND scenario of Berezhiani & Khoury (2015), therefore appears unlikely through collapse alone. Additional cooling mechanisms during or after collapse are necessary.

3.5. Dark matter self-interaction constraints

The distribution of DM, gas, and stellar mass in cluster collisions provides constraints on the cross-section of DM self-

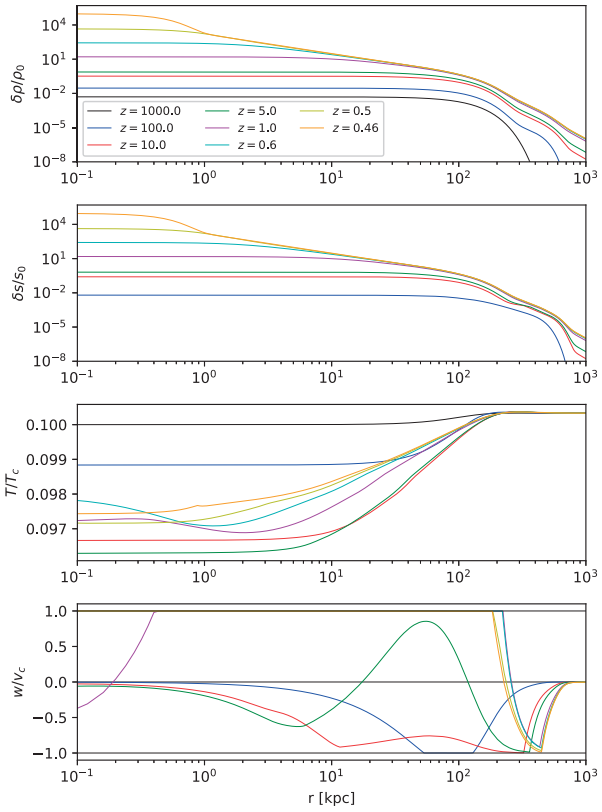

Fig. 9. Profiles of a collapsing SFDM halo where no entropy is produced as $w = v_v$ with an initial Gaussian density contrast, $m = 30\,\mathrm{eV}$, $g = 10^{-5}\,\mathrm{eV}^{-2}$, $L = 100\,\mathrm{kpc}$, and $T/T_c = 0.1$.

interactions, $\sigma/m < 0.5\,\mathrm{cm}^2\,\mathrm{g}^{-1}$ (Harvey et al. 2015). In terms of the two-body interaction strength, this corresponds to (Pitaevskii & Stringari 2016)

$$g_2 = \sqrt{4\pi\sigma}\frac{\hbar^2}{m} < 5\times10^{-12}\left(\frac{1\,\mathrm{eV}}{m}\right)^{1/2}\mathrm{eV}^{-2}. \quad (22)$$

The values of g_2 in the above results do not generally satisfy this constraint, but we chose to relax it since we do not know how it translates to SFDM. In any case, the above features were also

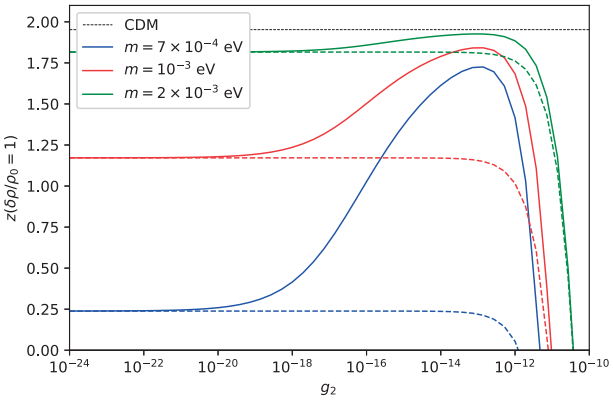

Fig. 10. Redshifts when the linear density contrast for the mode $k = 2/100\,\mathrm{kpc}^{-1}$ with $T/T_c = 2 \times 10^{-6}$ reaches unity for various masses and interaction strengths. Both the superfluid case (solid lines) and the corresponding non-superfluid case (striped lines) are shown, illustrating that the same features can be found for a choice of parameters that satisfy the constraint from cluster collisions on DM mass and self-interaction.

found for smaller g_2 using perturbation theory (while simultaneously lowering m and T/T_c) that do satisfy the constraints, as is exemplified in Fig. 10.

4. Conclusions

When superfluid behavior is included in a finite-temperature DM fluid, the formation of structure is found to be much more efficient in certain regions of parameter space than one would, naively, expect, through it is still slower compared to CDM. The effect of thermal counterflow is most prominent when the thermal suppression is large, such as at small scales and relatively high temperatures. The increased collapse efficiency is also expected to be a general feature of SFDM regardless of the EOS used, though the specific model in question will certainly affect the finer details through the dependence of entropy, pressure, and critical velocity on temperature, mass density, and the model parameters. The toy models used in this work were motivated by condensed matter physics, but suffer some severe limitations at high redshifts. Both are derived under the assumption that the interactions are weak and the number density is not too large, which is invalid at very early times. Furthermore, the zero-temperature pressure depends on the number density through n^2 and n^3, resulting in very high pressures at high redshifts that might wash out the initial perturbations set up by inflation. The generalization of this work to more exotic DM fluids and adding interactions between DM and baryons, which has recently been considered in the literature, is therefore of interest in the further study of SFDM models. It may also be of interest to study the case when thermal equilibrium is not always assumed so that the DM fluid can fall in and out of equilibrium and superfluidity can vanish and reappear.

Superfluid models of DM involve processes that require the superfluid hydrodynamic equations to be properly described. Throughout this work, spherical symmetry was assumed, but nonradial and turbulent motion is expected to have a significant impact on the superfluid dynamics, especially through the critical velocity, which is broken at smaller radial thermal counterflows. It is also important to understand the effect of mergers in SFDM. Large-scale and high-resolution simulations will therefore be essential for the further study of structure formation. The main challenge in this line of inquiry may be developing numerical schemes that are faster and more accurate than the modified first-order FORCE scheme used in this work that can capture the small-scale motion of the superfluid and its effect on structure formation.

Acknowledgements. We thank the Research Council of Norway for their support. We are grateful for the helpful comments and suggestions made by the anonymous referee.

References

Andersen, J. O. 2004, Rev. Mod. Phys., 76, 599
Angus, G., Diaferio, A., Famaey, B., Gentile, G., & van der Heyden, K. 2014, J. Cosmol. Astropart. Phys., 2014, 079
Angus, G. W., Diaferio, A., Famaey, B., & van der Heyden, K. J. 2013, MNRAS, 436, 202
Barenghi, C. F., Skrbek, L., & Sreenivasan, K. R. 2014, Proc. Nat. Acad. Sci., 111, 4647
Berezhiani, L., & Khoury, J. 2015, Phys. Rev. D, 92, 103510
Bullock, J. S., & Boylan-Kolchin, M. 2017, ARA&A, 55, 343
Chapman, S., Hoyos, C., & Oz, Y. 2014, J. High Energy Phys., 2014, 27
Cyburt, R. H., Fields, B. D., Olive, K. A., & Yeh, T.-H. 2016, Rev. Mod. Phys., 88, 015004
Darve, C., Bottura, L., Patankar, N. A., & Van Sciver, S. 2012, AIP Conf. Proc., 1434, 247
Del Popolo, A., & Le Delliou, M. 2017, Galaxies, 5, 17
Dodelson, S. 2011, Int. J. Mod. Phys. D, 20, 2749
Doi, D., Shirai, Y., & Shiotsu, M. 2008, AIP Conf. Proc., 985, 648
Elbert, O. D., Bullock, J. S., Garrison-Kimmel, S., et al. 2015, MNRAS, 453, 29
Famaey, B., & McGaugh, S. S. 2012, Living Rev. Relativ., 15, 10
Glyde, H. R. 2013, J. Low Temp. Phys., 172, 364
Harvey, D., Massey, R., Kitching, T., Taylor, A., & Tittley, E. 2015, Science, 347, 1462
Hu, W., Barkana, R., & Gruzinov, A. 2000, Phys. Rev. Lett., 85, 1158
Khalatnikov, I. M. 2000, An Introduction to the Theory Of Superfluidity, 1st edn. (Boulder, CO: Westview Press)
Khoury, J. 2016, Phys. Rev. D, 93, 103533
Landau, L. 1941, Phys. Rev., 60, 356
Landau, L. D., & Lifshitz, E. M. 1987, Course of Theoretical Physics, 2nd edn. (Oxford, UK: Butterworth-Heinemann), 6
Lelli, F., McGaugh, S. S., & Schombert, J. M. 2015, ApJ, 816, L14
Martel, H., & Shapiro, P. R. 1998, MNRAS, 297, 467
McGaugh, S. S. 2005, ApJ, 632, 859
McGaugh, S. S. 2012, ApJ, 143, 40
McGaugh, S. S., Schombert, J. M., Bothun, G. D., & de Blok, W. J. G. 2000, ApJ, 533, L99
Milgrom, M. 1983a, ApJ, 270, 371
Milgrom, M. 1983b, ApJ, 270, 384
Milgrom, M. 1983c, ApJ, 270, 365
Mocz, P., Vogelsberger,, M., Robles, V. H., et al. 2017, MNRAS, 471, 4559
Pethick, C. J., & Smith, H. 2008, Bose-Einstein Condensation in Dilute Gases, 2nd edn. (Cambridge: Cambridge University Press)
Pitaevskii, L. P., & Stringari, S. 2016, Bose-Einstein Condensation and Superfluidity (Oxford, UK: Oxford University Press)
Planck Collaboration XIII. 2016, A&A, 594, A13
Sales, L. V., Navarro, J. F., Oman, K., et al. 2016, MNRAS, 464, 2419
Santos-Santos, I. M., Brook, C. B., Stinson, G., et al. 2015, MNRAS, 455, 476
Sawala, T., Frenk, C. S., Fattahi, A., et al. 2016, MNRAS, 457, 1931
Schive, H. Y., Chiueh, T., & Broadhurst, T. 2014, Nat. Phys., 10, 496
Schwabe, B., Niemeyer, J. C., & Engels, J. F. 2016, Phys. Rev. D, 94, 043513
Sharma, A., Khoury, J., & Lubensky, T. 2019, J. Cosmol. Astropart. Phys., 2019, 054
Skrbek, L. 2011, J. Phys. Conf. Ser., 318, 012004
Skrbek, L., & Sreenivasan, K. R. 2012, Phys. Fluids, 24, 011301
Soulaine, C., Quintard, M., Baudouy, B., & Van Weelderen, R. 2017, Phys. Rev. Lett., 118, 074506
Spergel, D. N., & Steinhardt, P. J. 2000, Phys. Rev. Lett., 84, 3760
Taylor, E., & Griffin, A. 2005, Phys. Rev. A, 72, 8739
Tegmark, M., Blanton, M. R., Strauss, M. A., et al. 2004, ApJ, 606, 702
Toro, E. 2006, Appl. Numer. Math., 56, 1464
Tulin, S., & Yu, H.-B. 2018, Phys. Rep., 730, 1
Zhu, Q., Marinacci, F., Maji, M., et al. 2016, MNRAS, 458, 1559
Zuntz, J., Zlosnik, T. G., Bourliot, F., Ferreira, P. G., & Starkman, G. D. 2010, Phys. Rev. D, 81, 104015

Appendix A: equation of state

An EOS for a weakly interacting Bose gas valid at all temperatures was recently proposed by Sharma et al. (2019) for two-body and three-body interactions. Since we do not know the true EOS of DM and must resort to toy models, we instead approximated the EOS by using an ideal Bose gas with zero-temperature contributions from weak interactions. At very low temperatures, this approximation breaks down as the interactions become increasingly important, but we generally remain well above this regime.

An important quantity is the critical temperature T_c, above which the fluid behaves as a normal fluid, while below the fluid condenses into a BEC and becomes superfluid;

$$T_c = \frac{2\pi\hbar^2}{mk_B}\left(\frac{n}{\zeta(3/2)}\right)^{2/3} = \frac{2\pi\hbar^2}{m^{5/3}k_B}\left(\frac{\rho}{\zeta(3/2)}\right)^{2/3}, \tag{A.1}$$

where $n = \rho/m$ is the particle number density.

As an estimate for the superfluid fraction $f_s = \rho_s/\rho$ we use the fraction of particles in the BEC in an ideal Bose gas;

$$f_s = \begin{cases} 1 - \left(\frac{T}{T_c}\right)^{3/2}, & T \le T_c \\ 0, & T > T_c. \end{cases} \tag{A.2}$$

For the other thermodynamic quantities, such as pressure, entropy, etc., we must consider them above and below T_c separately. Both two-body and three-body interactions are given, parameterized by g_2 and g_3, respectively.

A.1. $T > T_c$

The pressure is given by

$$P = \begin{cases} g_2n^2 + \frac{\sqrt{2}\Gamma(5/2)(k_BT)^{5/2}m^{3/2}}{3\pi^2\hbar^3}\mathrm{Li}_{5/2}\left(e^{\beta(\mu-2g_2n)}\right), & \text{two-body} \\ 4g_3n^3 + \frac{\sqrt{2}\Gamma(5/2)(k_BT)^{5/2}m^{3/2}}{3\pi^2\hbar^3}\mathrm{Li}_{5/2}\left(e^{\beta(\mu-6g_3n^2)}\right), & \text{three-body,} \end{cases} \tag{A.3}$$

where $\Gamma(x)$ is the gamma function, $\mathrm{Li}_z(x)$ is the polylogarithmic function, $\beta = 1/k_BT$, and the chemical potential μ is determined by the equation for the number density

$$n = \begin{cases} \frac{\sqrt{2}\Gamma(5/2)}{3\pi^2\hbar^3}(k_BT)^{3/2}m^{3/2}\mathrm{Li}_{3/2}\left(e^{\beta(\mu-2g_2n)}\right), & \text{two-body} \\ \frac{\sqrt{2}\Gamma(5/2)}{3\pi^2\hbar^3}(k_BT)^{3/2}m^{3/2}\mathrm{Li}_{3/2}\left(e^{\beta(\mu-6g_3n^2)}\right), & \text{three-body.} \end{cases} \tag{A.4}$$

The entropy is

$$S = \begin{cases} \frac{5}{2}\frac{P}{T} - n\beta(\mu - 2g_2n), & \text{two-body} \\ \frac{5}{2}\frac{P}{T} - n\beta(\mu - 6g_3n^2), & \text{three-body,} \end{cases} \tag{A.5}$$

and the internal energy is

$$U = ST - P + \mu n. \tag{A.6}$$

The sound speed used when determining the time-stepping in the numerical scheme was

$$c_s = \sqrt{\frac{5}{3}\frac{k_BT}{m}}. \tag{A.7}$$

In the limit of very high temperature, these reduce to the classical ideal gas.

A.2. $T \le T_c$

The EOS below the critical temperature is given by the ideal Bose gas plus some zero-temperature contributions due to interactions;

$$P = \begin{cases} \frac{1}{2}g_2n^2 + \zeta(5/2)\left(\frac{m}{2\pi\hbar^2}\right)^{3/2}(k_BT)^{5/2}, & \text{two-body} \\ \frac{2}{3}g_3n^3 + \zeta(5/2)\left(\frac{m}{2\pi\hbar^2}\right)^{3/2}(k_BT)^{5/2}, & \text{three-body,} \end{cases} \tag{A.8}$$

$$S = \frac{5}{2}\zeta(5/2)\left(\frac{m}{2\pi\hbar^2}\right)^{3/2}k_B^{5/2}T^{3/2}, \quad \text{two-and three-body,} \tag{A.9}$$

$$\mu = \begin{cases} g_2n, & \text{two-body} \\ g_3n^2, & \text{three-body,} \end{cases} \tag{A.10}$$

and the internal energy is again given by Eq. (A.6). The fastest sound speed was approximated using

$$c_s = \sqrt{\frac{\zeta(5/2)}{\zeta(3/2)}\frac{5}{3}\frac{k_BT}{m}}, \tag{A.11}$$

and the critical velocity given by

$$v_c = \begin{cases} \sqrt{\frac{g_2n}{m}\left[1 - (T/T_c)^{3/2}\right]}, & \text{two-body} \\ \sqrt{\frac{2g_3n^2}{m}\left[1 - (T/T_c)^{3/2}\right]\left[1 + 2(T/T_c)^{3/2}\right]}, & \text{three-body.} \end{cases} \tag{A.12}$$

There is a small discontinuity at the critical temperature, with $\mu = 2ng_2$ above and $\mu = ng_2$ below for the two-body interaction (and a similar jump in zero-temperature pressure and internal energy). There should be a crossover region as the condensate fraction increases, but during this crossover the thermal contributions dominates and the discontinuity is negligible.

Appendix B: Numerical scheme

In this work, we employed a modified first-order FORCE scheme (Toro 2006) – an incomplete Riemann solver – for the superfluid hydrodynamic equations with source terms due to gravity and from using spherical coordinates. The source terms were evaluated at two stages during each time-step: once before the advection step, and once after, at which point the average of the two evaluations was added to the solution. Gravity was also evaluated with half a time-step when computing fluxes during the advection step. Finally, we enforced the critical velocity, which was done in three stages; once when computing fluxes, once after the fluxes from the advection step were applied, and a final time after the source terms were applied. Further details are presented below.

For spherical collapse, this scheme was found to be sufficient since the solutions are mostly smooth, evolve slowly, and are one-dimensional. For more complex and higher dimensional cases where shock fronts arise and the solutions undergo fast changes, this scheme is expected to perform suboptimally, primarily because it is first-order. There is a well-known way to increase the order and thus accuracy of the scheme through slope reconstruction and slope limiters. However, instabilities arose when the superfluid component was included, and adding further restrictions to the reconstructed slopes with modified slope limiters failed to fix this. Slope reconstruction was therefore not used.

B.1. First-order FORCE scheme

The FORCE scheme is a variant of Godunov's method for solving partial differential equations. In this method, the domain is divided into finite-volume elements, or cells, and the Riemann problem at each cell interface is solved. The Riemann problem is the initial value problem with two piece-wise constant initial regions connected by a discontinuity, then asking how this evolves in time and what the net flux across the interface is. The scheme for computing or approximating this flux is called a Riemann solver and is what characterizes the different ways of implementing Godunov's method.

To see how this works, one can consider the m-component state vector U that obeys the one-dimensional conservative equation

$$\partial_t \boldsymbol{U} + \partial_x \boldsymbol{F}(\boldsymbol{U}) = \boldsymbol{0}, \tag{B.1}$$

where $\boldsymbol{F}$ is the flux. By integrating over the time interval $[t^n, t^{n+1}]$ and cell-volume $[x_{i-1/2}, x_{i+1/2}]$, we get

$$\boldsymbol{U}_i^{n+1} = \boldsymbol{U}_i^n - \frac{\Delta t}{\Delta x}[\boldsymbol{F}_{i-1/2} - \boldsymbol{F}_{i+1/2}], \tag{B.2}$$

where

$$\boldsymbol{U}_i^n = \frac{1}{\Delta x}\int_{x_{i-1/2}}^{x_{i+1/2}} \boldsymbol{U}(x, t^n)\,\mathrm{d}x, \tag{B.3}$$

$$\boldsymbol{F}_{i+1/2} = \frac{1}{\Delta t}\int_{t^n}^{t^{n+1}} \boldsymbol{F}(x_{i+1/2}, t)\,\mathrm{d}t. \tag{B.4}$$

In the first-order Godunov scheme, the state $\boldsymbol{U}$ is assumed to be piece-wise constant in each cell, given by the cell average $\boldsymbol{U}_i^n$. To compute $\boldsymbol{F}_{i+1/2,}$ the states on the left and right sides of the interface is used, $\boldsymbol{U}_{i+1/2,\mathrm{L}} = \boldsymbol{U}_i^n$ and $\boldsymbol{U}_{i+1/2,\mathrm{R}} = \boldsymbol{U}_{i+1}^n$, and the corresponding Riemann problem is solved or approximated. The time-step is chosen so that no signal in the domain travels further than one cell length Δx. This is given by a Courant-Friedrich-Lewy (CFL) type condition

$$\Delta t_\mathrm{s} = C_\mathrm{CFL}^\mathrm{s}\frac{\Delta x}{v_\mathrm{max}}, \tag{B.5}$$

where v_max is the maximum signal speed in the domain, and $C_\mathrm{CFL}^\mathrm{s}$ is a number less than one that controls how far across a cell the fastest signal is allowed to move during each time-step. In simulations with gravity and expansion, additional constraints need to be added to the time-stepping. For gravity, the free-fall distance in each cell, with acceleration g, must be smaller than the cell lengths,

$$\Delta t_\mathrm{ff} = C_\mathrm{CFL}^\mathrm{ff}\sqrt{\frac{2\Delta x}{g}}, \tag{B.6}$$

and for expansion, the relative change in the scale factor is restricted:

$$\Delta t_\mathrm{exp} = C_\mathrm{CFL}^\mathrm{exp}\frac{1}{H}. \tag{B.7}$$

Here, $C_\mathrm{CFL}^\mathrm{ff}$ and $C_\mathrm{CFL}^\mathrm{exp}$ are also numbers less than one. In this work, we used $C_\mathrm{CFL}^\mathrm{s} = 0.5$, $C_\mathrm{CFL}^\mathrm{ff} = 0.5$, and $C_\mathrm{CFL}^\mathrm{exp} = 0.01$. The final value for the time-step is the smallest of the above,

$$\Delta t = \min[\Delta t_\mathrm{s}, \Delta t_\mathrm{ff}, \Delta t_\mathrm{exp}]. \tag{B.8}$$

The FORCE scheme approximates the interface flux $\boldsymbol{F}$ (given the left and right states $\boldsymbol{U}_\mathrm{L}$ and $\boldsymbol{U}_\mathrm{R}$) as the average of the Lax–Friedrichs flux and the two-step Lax–Wendroff flux;

$$\begin{aligned}
\boldsymbol{F}^\mathrm{FORCE} &= \frac{1}{2}[\boldsymbol{F}^\mathrm{LF} + \boldsymbol{F}^\mathrm{LW}],\\
\boldsymbol{F}^\mathrm{LF} &= \frac{1}{2}[\boldsymbol{F}(\boldsymbol{U}_\mathrm{L}) + \boldsymbol{F}(\boldsymbol{U}_\mathrm{R})] - \frac{1}{2}\frac{\Delta x}{\Delta t}[\boldsymbol{U}_\mathrm{R} - \boldsymbol{U}_\mathrm{L}],\\
\boldsymbol{F}^\mathrm{LW} &= \boldsymbol{F}(\boldsymbol{U}^\mathrm{LW}),\\
\boldsymbol{U}^\mathrm{LW} &= \frac{1}{2}[\boldsymbol{U}_\mathrm{L} + \boldsymbol{U}_\mathrm{R}] - \frac{1}{2}\frac{\Delta t}{\Delta x}[\boldsymbol{F}(\boldsymbol{U}_\mathrm{R}) - \boldsymbol{F}(\boldsymbol{U}_\mathrm{L})].
\end{aligned} \tag{B.9}$$

We modified this by enforcing the critical velocity on the intermediate state $\boldsymbol{U}^\mathrm{LW}$ before computing the flux $\boldsymbol{F}^\mathrm{LW}$.

B.2. Sources

Gravity and extra terms when using spherical coordinates and super-comoving variables appear as source terms $\boldsymbol{S}$ in the superfluid equations. Continuing with the above example, we have

$$\partial_t \boldsymbol{U} + \partial_x \boldsymbol{F}(\boldsymbol{U}) = \boldsymbol{S}. \tag{B.10}$$

To modify our Godunov scheme to incorporate the sources in the flux, we did the following: at the beginning of each time-step, we had the states $\boldsymbol{U}_i^n$. To do the advection (the Godunov step), we input the left and right states at each boundary $i + 1/2$; $\boldsymbol{U}_{i+1/2,\mathrm{L}} = \boldsymbol{U}_i$, $\boldsymbol{U}_{i+1/2,\mathrm{R}} = \boldsymbol{U}_{i+1}$. But before we computed the interface flux, we applied half a time-step of the source due to gravity,

$$\begin{aligned}
\boldsymbol{U}^*_{i+1/2,\mathrm{L}} &= \boldsymbol{U}_{i+1/2,\mathrm{L}} + \frac{1}{2}\Delta t\left(\boldsymbol{S}^n_{i+1/2,\mathrm{L}}\right)_\mathrm{grav},\\
\boldsymbol{U}^*_{i+1/2,\mathrm{L}} &= \boldsymbol{U}_{i+1/2,\mathrm{R}} + \frac{1}{2}\Delta t\left(\boldsymbol{S}^n_{i+1/2,\mathrm{R}}\right)_\mathrm{grav},
\end{aligned} \tag{B.11}$$

where $\boldsymbol{S}^n_{i+1/2,\mathrm{L}}$ and $\boldsymbol{S}^n_{i+1/2,\mathrm{R}}$ are the left and right values for the sources. In this work, we computed these using the average gravitational acceleration $(\boldsymbol{\nabla}\Phi)^n_{i+1/2,\mathrm{L/R}} = \frac{1}{2}[(\boldsymbol{\nabla}\Phi)^n_i + (\boldsymbol{\nabla}\Phi)^n_{i+1}]$, and the left and right states $\boldsymbol{U}_{i+1/2,\mathrm{L/R}}$. We then used $\boldsymbol{U}^*_{i+1/2,\mathrm{L}}$ and $\boldsymbol{U}^*_{i+1/2,\mathrm{R}}$ as the input states in the Godunov scheme to get $\boldsymbol{F}_{i+1/2}$, and updated the state vectors from the previous time-step:

$$\boldsymbol{U}_i^{n+1,*} = \boldsymbol{U}_i^n - \frac{\Delta t}{\Delta x}[\boldsymbol{F}_{i-1/2} - \boldsymbol{F}_{i+1/2}]. \tag{B.12}$$

This modification to the Godunov scheme was to include the effect of gravity on the flux, but explicitly adding the sources to the solution remains to be done. For this, we used the average before and after the advection step;

$$\boldsymbol{U}_i^{n+1} = \boldsymbol{U}_i^{n+1,*} + \Delta t\frac{1}{2}[\boldsymbol{S}_i^n + \boldsymbol{S}_i^{n+1,*}]. \tag{B.13}$$

B.3. Enforcing critical velocity

The critical velocity was enforced by iteratively converting kinetic energy into internal energy and generated entropy in all cells until $w < v_\mathrm{c}$. The scheme works as follows: we consider a cell with the state vector $\boldsymbol{U}^l$, where l denotes the current step in the iterative scheme to enforce v_c, and $l = 0$ is the initial state. From this we get the fluid variables of the cell, v_s^l, v_n^l, S^l, etc. If $w^l < v_\mathrm{c}^l$, the Landau criterion is satisfied and we do nothing. If instead $w^l > v_\mathrm{c}^l$, we apply a small change Δv_s^l to v_s^l to update it to $l + 1$ and decrease w,

$$\boldsymbol{v}_s^{l+1} = \boldsymbol{v}_s^l + \Delta\boldsymbol{v}_\mathrm{s}^l. \tag{B.14}$$

By keeping $\boldsymbol{j}$ constant and assuming that the change in the superfluid fraction is negligible compared to the change in velocity, we get

$$\Delta\boldsymbol{v}_\mathrm{n}^l = -\frac{\rho_\mathrm{s}^l}{\rho_\mathrm{n}^l}\Delta\boldsymbol{v}_\mathrm{s}^l. \tag{B.15}$$

Using conservation of energy the change in internal energy is equal to the change in kinetic energy;

$$\begin{aligned}\Delta U^l &= -\Delta E_\mathrm{kin}^l = -\Delta\left(\frac{1}{2}\rho_\mathrm{n}^l|\boldsymbol{v}_\mathrm{n}^l|^2 + \frac{1}{2}\rho_\mathrm{s}^l|\boldsymbol{v}_\mathrm{s}^l|^2\right)\\ &= -\rho_\mathrm{s}^l(\boldsymbol{v}_\mathrm{s}^l - \boldsymbol{v}_\mathrm{n}^l)\cdot\Delta\boldsymbol{v}_\mathrm{s}^l.\end{aligned} \tag{B.16}$$

The change in entropy is $\Delta S^l = \Delta Q^l/T^l$, where ΔQ^l is the heating of the fluid, which in this case is just the change in internal energy:

$$\Delta S^l = \frac{\Delta Q^l}{T^l} = \frac{\Delta U^l}{T^l} = -\frac{\rho_\mathrm{s}^l(\boldsymbol{v}_\mathrm{s}^l - \boldsymbol{v}_\mathrm{n}^l)\cdot\Delta\boldsymbol{v}_\mathrm{s}^l}{T^l}. \tag{B.17}$$

The updated entropy is

$$S^{l+1} = S^l + \Delta S^l. \tag{B.18}$$

We arrive at the state vector $\boldsymbol{U}^{l+1}$ and repeat the above process until $w < v_\mathrm{c}$. The only part that needs to be specified is $\Delta\boldsymbol{v}_\mathrm{s}^l$, which was chosen as

$$\Delta\boldsymbol{v}_\mathrm{s}^l = -C(w^l)\,\hat{\boldsymbol{w}}^l, \tag{B.19}$$

where

$$C(w) = [10^{-2}, 10^{-5}]w. \tag{B.20}$$

The numerical factor in Eq. (B.20) was tuned to give as smooth w-profile as possible while keeping the scheme from becoming too slow.

Paper II

Dynamical friction in Bose-Einstein condensed self-interacting dark matter at finite temperatures, and the Fornax dwarf spheroidal

Stian T. H. Hartman, Hans A. Winther, David F. Mota

Published in *Astronomy & Astrophysics*, March 2021, volume 647, A70,
DOI: 10.1051/0004-6361/202039865. arXiv: 2011.00116.

II

A&A 647, A70 (2021)
https://doi.org/10.1051/0004-6361/202039865

Astronomy & Astrophysics

Dynamical friction in Bose-Einstein condensed self-interacting dark matter at finite temperatures, and the Fornax dwarf spheroidal

S. T. H. Hartman, H. A. Winther, and D. F. Mota

Institute of Theoretical Astrophysics, University of Oslo, PO Box 1029, Blindern 0315, Oslo, Norway
e-mail: stian.hartman@gmail.com

Received 6 November 2020 / Accepted 28 December 2020

ABSTRACT

Aims. The aim of the present work is to better understand the gravitational drag forces, also referred to as dynamical friction, acting on massive objects moving through a self-interacting Bose-Einstein condensate, also known as a superfluid, at finite temperatures. This is relevant for models of dark matter consisting of light scalar particles with weak self-interactions that require nonzero temperatures, or that have been heated inside galaxies.

Methods. We derived expressions for dynamical friction using linear perturbation theory, and compared these to numerical simulations in which nonlinear effects are included. After testing the linear result, it was applied to the Fornax dwarf spheroidal galaxy, and two of its gravitationally bound globular clusters. Dwarf spheroidals are well-suited for indirectly probing properties of dark matter, and so by estimating the rate at which these globular clusters are expected to sink into their host halo due to dynamical friction, we inferred limits on the superfluid dark matter parameter space.

Results. The dynamical friction in a finite-temperature superfluid is found to behave very similarly to the zero-temperature limit, even when the thermal contributions are large. However, when a critical velocity for the superfluid flow is included, the friction force can transition from the zero-temperature value to the value in a conventional thermal fluid. Increasing the mass of the perturbing object induces a similar transition to when lowering the critical velocity. When applied to two of Fornax's globular clusters, we find that the parameter space preferred in the literature for a zero-temperature superfluid yields decay times that are in agreement with observations. However, the present work suggests that increasing the temperature, which is expected to change the preferred parameter space, may lead to very small decay times, and therefore pose a problem for finite-temperature superfluid models of dark matter.

Key words. dark matter – cosmology: theory

1. Introduction

When a massive object moves through a background medium, its gravitational field can cause the background to form an overdensity that trails it, and in turn exerts a gravitational force on the object that produced it. This is known as dynamical friction, and is a purely gravitational phenomenon. It can therefore also arise in systems in which the constituent components otherwise have very weak or no coupling to one another, or behave as collisionless particles, such as dark matter (DM) and stars. Many important processes in the formation of structure, the evolution of galaxies, and the dynamics of astrophysical systems, such as mergers (Jiang et al. 2008; Boylan-Kolchin et al. 2008), the sinking of satellites into their host halos (Colpi et al. 1999; Cowsik et al. 2009; Cole et al. 2012; Tamfal et al. 2020), the decay of orbiting black holes and binaries (Just et al. 2011; Pani 2015; Dosopoulou & Antonini 2017; Gómez & Rueda 2017), and bar–halo interactions in disk galaxies (Weinberg 1985; Debattista & Sellwood 2000; Sellwood 2014), therefore depend on the nature of this drag force.

The first detailed calculation of dynamical friction was carried out by Chandrasekhar (1943) in the context of stellar dynamics. Chandrasekhar considered the varying gravitational forces acting on a star as it moves through its stellar neighborhood, and found that it experiences a net average force opposite to its direction of motion, that is, a gravitational drag force. He treated the background of stars as an infinite homogeneous gas of collisionless particles following a Maxwell-Boltzmann velocity distribution, an approach that can also be used for collisionless DM (Mulder 1983; Colpi et al. 1999; Binney & Tremaine 2008). However, for a collisional medium, pressure forces must be taken into account when computing the dynamical friction, and this has been done both analytically and numerically for various types of gases, such as ideal (Ostriker 1999; Sánchez-Salcedo & Brandenburg 1999; Lee & Stahler 2011, 2014; Thun et al. 2016), relativistic (Barausse 2007; Katz et al. 2019), and magnetized gases (Sánchez-Salcedo 2012; Shadmehri & Khajenabi 2012).

The nature of the dynamical friction due to DM is related to the nature of DM itself. The standard model of the universe, ΛCDM, includes cold and collisionless DM as the predominant matter component, making up about 80% of all matter. While extremely successful at explaining observables such as the microwave background radiation, large-scale structure, the expansion history of the Universe, and important properties of galaxies (Davis et al. 1985; Percival et al. 2001; Tegmark et al. 2004; Trujillo-Gomez et al. 2011; Vogelsberger et al. 2014; Planck Collaboration XIII 2016; Riess et al. 2016), the identity of DM has remained elusive. Furthermore, there are discrepancies between simulations of structure formation at small scales, and observations (for reviews, see e.g., Weinberg et al. 2015; Del Popolo & Le Delliou 2017; Bullock & Boylan-Kolchin 2017). These discrepancies may have their solution within ΛCDM by including more realistic models of baryonic physics in simulations (Santos-Santos et al. 2015; Sales et al. 2016; Zhu et al. 2016;

Sawala et al. 2016), but the solution may also be in alternative models of DM (Hu et al. 2000; Spergel & Steinhardt 2000; Shao et al. 2013; Lovell et al. 2014; Schive et al. 2014; Elbert et al. 2015; Berezhiani & Khoury 2015; Khoury 2016; Schwabe et al. 2016; Mocz et al. 2017; Tulin & Yu 2018; Clesse & García-Bellido 2018; Boldrini et al. 2020). For these reasons, studies have also been carried out on dynamical friction in various DM models, such as fuzzy DM (Hui et al. 2017; Bar-Or et al. 2019; Lancaster et al. 2020), and self-interacting Bose-Einstein condensed (SIBEC) DM (Berezhiani et al. 2019), also known as superfluid DM. A number of studies have considered finite-temperature effects of interacting superfluid DM (Harko & Mocanu 2012; Slepian & Goodman 2012; Harko et al. 2015; Sharma et al. 2019). Of particular note is the one presented by Berezhiani & Khoury (2015), who suggested that superfluid DM, when provided with a special Lagrangian structure and coupling to the visible sector, can give rise to modified Newtonian dynamics (MOND; Milgrom 1983a,b,c; Famaey & McGaugh 2012) between baryons at galactic scales. This MONDian force is mediated by superfluid phonons, which cease to be coherent on scales larger than galaxies, resulting in the vanishing of the extra force and the preservation of the large-scale success of CDM. For the fifth force to be MONDian, the DM particles need exotic three-body self-interactions, and the DM fluid has to be above a certain temperature to be well-behaved. Finite-temperature DM might arise through processes inside galaxies that transfer energy to the DM halo (Goerdt et al. 2010; Pontzen & Governato 2012; Read et al. 2019), possibly heating up the DM fluid.

Because the form of the dynamical friction experienced by visible matter embedded in DM halos depends on the properties of DM, observations of galaxies can be used to constrain DM. Dwarf spheroidal galaxies (dSph) are particularly well-suited for this purpose. Being poor in visible matter, their dynamical behavior is dominated by their DM component and they therefore provide a testing ground for DM models (Battaglia et al. 2013; Walker 2013; Strigari 2018). One such system is the Fornax dSph and its five gravitationally bound globular clusters (GCs; Mackey & Gilmore 2003), with a sixth one recently found to likely be a genuine, albeit dim, GC (Wang et al. 2019a). The orbital decay times of these GCs, in particular the inner two (not counting the recently discovered sixth GC), due to dynamical friction from a CDM background, have been estimated to $\tau_{\rm DF} \lesssim 1\,{\rm Gyr}$ (Oh et al. 2000; Cole et al. 2012; Hui et al. 2017; Arca-Sedda & Capuzzo-Dolcetta 2017), much shorter than the supposed age of the host system, $\tau_{\rm age} \sim 10\,{\rm Gyr}$ (del Pino et al. 2013; Wang et al. 2019b). Furthermore, there is no bright stellar nucleus at the center of Fornax dSph that would suggest the sinking of other GCs in the past. This apparent mismatch between theoretical prediction and observation suggests one of two scenarios; that we are witnessing these GCs just as they are about to fall into their host, implying a fine-tuning of their initial positions, which seems unlikely; or that there is some mechanism, or property of DM that stops the GCs from migrating towards the center of the Fornax dSph. This discrepancy between CDM estimates and observations is the so-called timing-problem, and a number of solutions have been proposed, such as massive black holes heating the system (Oh et al. 2000); assuming the CDM profile of Fornax to be cored instead of cuspy (Goerdt et al. 2006; Cole et al. 2012); inaccurate modeling of the Fornax system and the rate of the orbital decay (Cowsik et al. 2009; Kaur & Sridhar 2018; Boldrini et al. 2019; Leung et al. 2020; Meadows et al. 2020); or some exotic property of DM (Hui et al. 2017; Lancaster et al. 2020).

In this work we extend the analysis of dynamical friction in a zero-temperature superfluid to finite temperatures, where the fluid is in a mixed state of normal fluid–made up of thermal excitations–and superfluid. This type of system has pressure terms coming from both thermal excitations and self-interactions, and can exhibit unique features due to the separate flow of the superfluid and normal fluid components. With an expression for the dynamical friction in SIBEC-DM, we estimate the time it takes for two of the GCs orbiting the Fornax dSph to sink into their host halo due to this gravitational drag, thereby inferring constraints on finite-temperature superfluid DM. The paper is organized as follows: in Sect. 2 the superfluid equations at both zero and finite temperatures are introduced, as well as some basic notions related to superfluidity. In Sects. 3 and 4 these equations are used to derive the dynamical friction at linear order, both in a steady-state and a finite-time scenario. The dynamical friction is also found using numerical simulations of the full superfluid hydrodynamic equations in Sect. 5, which is compared to the linear result in Sect. 6. The tools developed in the preceding sections are used in Sect. 7 to estimate the decay times of two of the GCs orbiting the Fornax dSph, and constraints on SIBEC-DM are inferred. In Sect. 8 a summary of this work and the main results are presented. Natural units are used throughout.

2. Hydrodynamics of finite-temperature superfluids

In the standard treatment, superfluids are often related to Bose-Einstein condensates (BEC), which form when the temperature is sufficiently low and the particle density high enough that the de Broglie wavelengths of identical bosons overlap, creating a coherent state that can be described by a single-particle wave-function. This wave-function is usually associated with the superfluid, and can therefore be regarded as a quantum mechanical effect at macroscopic scales. The wave-function ψ at the mean-field level is governed by the Gross-Pitaevskii equation, a non-linear Schrödinger equation with effective contact interactions parameterized by g;

$$i\frac{\partial\psi}{\partial t} = \left[\frac{-\nabla^2}{2m} + g|\psi|^2 + mV_{\rm ext}\right]\psi. \tag{1}$$

The external potential $V_{\rm ext}$ can be a trapping potential, as is often used in cold atomic experiments, or a gravitational potential. The amplitude of ψ is related to the particle number density by $n = |\psi|^2$, and mass density $\rho = m|\psi|^2$.

By inserting for the wave-function

$$\psi = \sqrt{n}e^{{\rm i}S} = \sqrt{\frac{\rho}{m}}e^{{\rm i}S}, \tag{2}$$

and defining the velocity field $\boldsymbol{v} = \boldsymbol{\nabla}S/m$, the nonlinear Schrödinger equation can be reformulated in a hydrodynamic form. The real and imaginary parts of the Schrödinger equation give the set of equations

$$\frac{\partial\rho}{\partial t} + \boldsymbol{\nabla}\cdot(\rho\boldsymbol{v}) = 0, \tag{3}$$

$$\frac{\partial\boldsymbol{v}}{\partial t} + (\boldsymbol{v}\cdot\boldsymbol{\nabla})\boldsymbol{v} + \nabla\left(\frac{g\rho}{m^2} + Q + V_{\rm ext}\right) = 0. \tag{4}$$

These are the so-called Madelung equations (Madelung 1926). The first is a continuity equation for mass, and the second is a

quantum variant of the momentum equation, with the quantum potential

$$Q = -\frac{1}{2m^2}\frac{\nabla^2\sqrt{\rho}}{\sqrt{\rho}}, \tag{5}$$

coming from the kinetic part of the Schrödinger equation that is present even in the absence of interactions. From the definition of the velocity field, we see that it is irrotational, because the curl of a gradient is zero. However, there can arise defects in the superfluid, around which the circulation is quantized as

$$m\oint \boldsymbol{v}\cdot \mathrm{d}\boldsymbol{l} = 2\pi N, \quad N\in\mathbb{Z}, \tag{6}$$

because the complex wave-function must be single-valued. These special structures in superfluids are called quantum vorticies. Both the Schrödinger and Madelung formulations have been used in cosmology as models for DM in order to explain the absence of small-scale structure that is predicted in N-body simulations of CDM (Schive et al. 2014; Mocz et al. 2017; Nori & Baldi 2018, 2021; Mina et al. 2020a,b).

At finite temperatures, the hydrodynamic formulation of a superfluid must take into account that the fluid is no longer completely superfluid. There is a thermal cloud of excitations in addition to the coherent superfluid state that carries entropy, gives a thermal contribution to the fluid pressure, and can be viscous and rotational. To complicate matters further, as the temperature of the fluid changes, the fraction of the fluid in this thermal cloud changes as well. This property of superfluids, to behave both as a superfluid (in the sense that we usually understand the term, as a fluid with zero viscosity, quantized circulation, and carrying no entropy) and a conventional fluid, has led to the development of a two-fluid picture of superfluids. The hydrodynamic equations for a finite-temperature superfluid are (neglecting the quantum potential; Taylor & Griffin 2005; Chapman et al. 2014):

$$\frac{\partial\rho}{\partial t} + \boldsymbol{\nabla}\cdot\boldsymbol{j} = 0, \tag{7}$$

$$\frac{\partial S}{\partial t} + \boldsymbol{\nabla}\cdot(S\boldsymbol{u}_\mathrm{n}) = 0, \tag{8}$$

$$\frac{\partial \boldsymbol{u}_\mathrm{s}}{\partial t} + \boldsymbol{\nabla}\left(\mu + \frac{1}{2}\boldsymbol{u}_\mathrm{s}^2\right) = -\boldsymbol{\nabla}\Phi, \tag{9}$$

$$\begin{aligned}\frac{\partial \boldsymbol{j}}{\partial t} &+ \boldsymbol{\nabla}P + \rho_\mathrm{s}(\boldsymbol{u}_\mathrm{s}\cdot\boldsymbol{\nabla})\boldsymbol{u}_\mathrm{s} + \rho_\mathrm{n}(\boldsymbol{u}_\mathrm{n}\cdot\boldsymbol{\nabla})\boldsymbol{u}_\mathrm{n}\\ &+ \boldsymbol{u}_\mathrm{s}[\boldsymbol{\nabla}\cdot(\rho_\mathrm{s}\boldsymbol{u}_\mathrm{s})] + \boldsymbol{u}_\mathrm{n}[\boldsymbol{\nabla}\cdot(\rho_\mathrm{n}\boldsymbol{u}_\mathrm{n})] = -\rho\boldsymbol{\nabla}\Phi.\end{aligned} \tag{10}$$

The thermal cloud, which we refer to as the "normal fluid", has density ρ_n, velocity $\boldsymbol{u}_\mathrm{n}$, and transports both mass and thermal energy. The second component is the "superfluid", with density ρ_s, a velocity field $\boldsymbol{u}_\mathrm{s}$, and carries no entropy. The total mass density is the sum of the two components, $\rho = \rho_\mathrm{n} + \rho_\mathrm{s}$, and likewise for momentum, $\boldsymbol{j} = \rho_\mathrm{n}\boldsymbol{u}_\mathrm{n} + \rho_\mathrm{s}\boldsymbol{u}_\mathrm{s}$. The fluid pressure is P, the entropy density S, temperature T, and $\mu = [P + U - ST - \frac{1}{2}\rho_\mathrm{n}(\boldsymbol{u}_\mathrm{s} - \boldsymbol{u}_\mathrm{n})^2]/\rho$.

As previously mentioned, superfluids and BECs are related phenomena, but it is important to stress that they are not equivalent. The formation of a BEC does not automatically imply a superfluid. To see this we must consider the co-called Landau criterion. Landau, in his seminal paper on superfluid liquid helium 4 (Landau 1941), made the following argument: Assume that dissipation and heating in a fluid takes place via the creation of elementary excitations. If these excitations become energetically unfavorable and cannot spontaneously appear, then dissipation and heating ceases, and the fluid becomes superfluid. The criterion for such a condition is for the relative velocity v between the superfluid and a scattering potential, such as an impurity or a container wall, to be smaller than a critical value,

$$v < v_\mathrm{c} = \min_{p}\frac{\epsilon(\boldsymbol{p})}{p}, \tag{11}$$

where $\epsilon(\boldsymbol{p})$ is the energy of an elementary excitation with momentum $\boldsymbol{p}$ (Pitaevskii & Stringari 2016). This criterion shows that an ideal BEC, for which the excitation spectrum is $\epsilon(\boldsymbol{p}) = p^2/2m$, has $v_\mathrm{c} = 0$ and is therefore not a superfluid. On the other hand, a Bose gas with weak interactions has–upon the formation of a BEC–an energy spectrum that is linear at small momentum, $\epsilon(\boldsymbol{p}) = c_\mathrm{s}p$. Hence $v_\mathrm{c} = c_\mathrm{s}$, and weakly interacting BECs are superfluids.

The Landau criterion is usually derived with the velocity relative to an external scatterer in mind, but it also applies to the thermal excitations that make up the normal fluid. The critical value for the relative velocity $\boldsymbol{w} = \boldsymbol{u}_\mathrm{s} - \boldsymbol{u}_\mathrm{n}$ of the normal fluid and superfluid is smaller than the one determined by Eq. (11), but the difference is small at low temperatures and weak self-interactions (Navez & Graham 2006).

The presence of the relative velocity $\boldsymbol{w}$, because of the partially independent motion of the superfluid and normal fluid components in a finite-temperature superfluid, has important consequences for its behavior. The superfluid part does not carry heat, while the normal fluid does, allowing mass and entropy to flow separately. This becomes clear if we define the velocity field for the mass flux, $\boldsymbol{v} = \boldsymbol{j}/\rho$, and express the equations for mass and entropy conservation in terms of $\boldsymbol{w}$ and $\boldsymbol{v}$;

$$\frac{\partial\rho}{\partial t} + \boldsymbol{\nabla}\cdot(\rho\boldsymbol{v}) = 0, \tag{12}$$

$$\frac{\partial S}{\partial t} + \boldsymbol{\nabla}\cdot(S\boldsymbol{v}) - \boldsymbol{\nabla}\cdot\left(\frac{S\rho_\mathrm{s}}{\rho}\boldsymbol{w}\right) = 0. \tag{13}$$

For a finite superfluid fraction, the entropy has an additional flux term, and therefore entropy and mass can have different flow patterns. This property is called thermal counterflow. The equation for $\partial\boldsymbol{w}/\partial t$ contains a driving term $S\boldsymbol{\nabla}T/\rho_\mathrm{n}$, and so the counterflow $\boldsymbol{w}$ tends to be directed towards regions of higher temperature, washing out thermal differences in the superfluid. As we see below, it is this property that makes the dynamical friction in a superfluid different from a corresponding fully normal fluid (i.e., a conventional fluid, $\rho_\mathrm{s} = 0$, with the same pressure forces).

When the Landau criterion is broken, with w approaching and passing the critical velocity, the superfluid flow starts to decay as a tangle of quantum vortices form, and causes a mutual friction between the superfluid and normal fluid components (Skrbek 2011; Skrbek & Sreenivasan 2012; Barenghi et al. 2014). Such a dissipative effect is not present in the superfluid equations, but can be included with additional terms, as has been done in numerical studies of superfluid helium (Doi et al. 2008; Darve et al. 2012; Soulaine et al. 2017). However, to circumvent the need for extra parameters and the need to assume the functional form of the mutual friction, we instead follow the same approach used in a previous work (Hartman et al. 2020); the dissipative processes are assumed to take place instantaneously when the relative velocity w exceeds the critical velocity. The velocity field $\boldsymbol{v}_\mathrm{s}$ is changed in such a way that the fluid momentum is conserved, and that only the magnitude of $\boldsymbol{w}$ is altered, not its direction, bringing it to $w = v_\mathrm{c}$. In other words, we assume the mutual friction to be directed along $\boldsymbol{w}$.

The critical temperature T_c is a central quantity in BEC superfluids. For $T > T_\mathrm{c}$, a gas of identical bosons is a normal

fluid, but for $T < T_c$, the particles begin accumulating in the ground state, forming a BEC, which in turn can form a superfluid. In the three-dimensional, homogeneous, ideal Bose gas, this critical temperature is

$$T_c = \frac{2\pi\hbar^2}{m^{5/3}}\left(\frac{\rho}{\zeta(3/2)}\right)^{2/3}, \tag{14}$$

where $\zeta(x)$ is the Riemann Zeta-function, and holds approximately for weakly interacting gases as well (Andersen 2004; Sharma et al. 2019).

For the thermodynamic quantities of a weakly interacting Bose gas, we again follow the approach used in a previous work (Hartman et al. 2020). The equation of state is approximated by an ideal gas with contributions from two-body interactions,

$$P = \frac{1}{2}\frac{g}{m^2}\rho^2 + \zeta(5/2)\left(\frac{m}{2\pi}\right)^{3/2} T^{5/2}, \tag{15}$$

$$S = \frac{5}{2}\zeta(5/2)\left(\frac{m}{2\pi}\right)^{3/2} T^{3/2}, \tag{16}$$

valid only for $T < T_c$. The fraction of particles in the condensate f_0 and the superfluid $f_s = \rho_s/\rho$ are both taken to be equal to the condensate fraction in the ideal case;

$$f_s = f_0 = 1 - \left(\frac{T}{T_c}\right)^{3/2}. \tag{17}$$

The critical velocity is approximated as

$$v_c = \sqrt{\frac{gnf_0}{m}}. \tag{18}$$

As long as the temperature is not too close to the transition point, and the interactions are sufficiently weak, these approximations work well.

3. Dynamical friction from steady-state linear perturbation theory

The starting point for computing the dynamical friction acting on an object, or a "perturber", moving through the superfluid are Eqs. (7)–(10). The gravitational potential is sourced by both the background mass density ρ, and the mass distribution $\rho_{\rm pert}$ of the perturber:

$$\nabla^2\Phi = 4\pi G[\rho + \rho_{\rm pert}]. \tag{19}$$

The superfluid is assumed to be homogeneous, and so the fluid variables are expanded to linear order, $\rho = \rho_0 + \delta\rho$, $S = S_0 + \delta S$, $\boldsymbol{u}_s = \delta\boldsymbol{u}_s$, and so on. The linear equations are

$$\frac{\partial\delta\rho}{\partial t} + \boldsymbol{\nabla}\cdot\delta\boldsymbol{j} = 0, \tag{20}$$

$$\frac{\partial\delta S}{\partial t} + S_0\boldsymbol{\nabla}\cdot\delta\boldsymbol{u}_n = 0, \tag{21}$$

$$\frac{\partial\delta\boldsymbol{u}_s}{\partial t} + \frac{1}{\rho_0}\boldsymbol{\nabla}\delta P - \frac{S_0}{\rho_0}\boldsymbol{\nabla}\delta T = -\boldsymbol{\nabla}\delta\Phi, \tag{22}$$

$$\frac{\partial\delta\boldsymbol{j}}{\partial t} + \boldsymbol{\nabla}\delta P = -\rho_0\boldsymbol{\nabla}\delta\Phi, \tag{23}$$

$$\delta\boldsymbol{u}_n = \frac{1}{\rho_0}\delta\boldsymbol{j} - \frac{\rho_{s0}}{\rho_0}\delta\boldsymbol{u}_s, \tag{24}$$

$$\nabla^2\delta\Phi = 4\pi G[\delta\rho + \rho_{\rm pert}]. \tag{25}$$

These can be combined into two coupled equations for $\delta\rho$ and δS;

$$\frac{\partial^2\delta\rho}{\partial t^2} - \left[\left(\frac{\partial P}{\partial\rho}\right)_0\nabla^2 + 4\pi G\rho_0\right]\delta\rho - \left(\frac{\partial P}{\partial S}\right)_0\nabla^2\delta S = 4\pi G\rho_0\rho_{\rm pert}, \tag{26}$$

$$\frac{\partial^2\delta S}{\partial t^2} - \frac{S_0}{\rho_0}\left[\left(\frac{\partial P}{\partial\rho}\right)_0\nabla^2 + S_0\frac{\rho_{s0}}{\rho_{n0}}\left(\frac{\partial T}{\partial\rho}\right)_0\nabla^2 + 4\pi G\rho_0\right]\delta\rho - \frac{S_0}{\rho_0}\left[\left(\frac{\partial P}{\partial S}\right)_0\nabla^2 + S_0\frac{\rho_{s0}}{\rho_{n0}}\left(\frac{\partial T}{\partial S}\right)_0\nabla^2\right]\delta S = 4\pi G S_0\rho_{\rm pert}. \tag{27}$$

The "0" subscript indicates that the quantity is evaluated at the background level. As expected, there are scale-dependent pressure terms that inhibit the growth of mass density and entropy perturbations, but in the entropy equation there are additional effective pressure terms that further reduce entropy perturbations. These are due to thermal counterflow and depend on the superfluid fraction, vanishing in the fully normal fluid limit. It must be noted that the critical velocity v_c is not included in the present approach, but the effect of this on linear theory is considered further in Sect. 4, as well as in Sect. 5 using numerical simulations.

Writing $\delta\rho = \alpha\rho_0$, and Fourier transforming into momentum ($\boldsymbol{k}$) and frequency (k_0) space, the solutions of the k-modes α_k are found:

$$\alpha_k = -4\pi G\rho_{{\rm pert},k}\frac{k_0^2 - Ak^2}{\left(k_0^2 - \omega_{k+}^2\right)\left(k_0^2 - \omega_{k-}^2\right)}, \tag{28}$$

where the dispersion relation is

$$\omega_{k\pm}^2 = C_4k^2 - C_2 \pm \sqrt{C_3k^4 - 2C_1C_2k^2 + C_2^2}, \tag{29}$$

and

$$A = \frac{S_0^2}{\rho_0}\frac{\rho_{s0}}{\rho_{n0}}\left(\frac{\partial T}{\partial S}\right)_0, \tag{30}$$

$$C_1 = \frac{1}{2}\left(\frac{\partial P}{\partial\rho}\right)_0 + \frac{S_0}{2\rho_0}\left(\frac{\partial P}{\partial S}\right)_0 - \frac{S_0^2}{2\rho_0}\frac{\rho_{s0}}{\rho_{n0}}\left(\frac{\partial T}{\partial S}\right)_0, \tag{31}$$

$$C_2 = 2\pi G\rho_0, \tag{32}$$

$$C_3 = C_4^2 + \frac{S_0^2}{\rho_0}\frac{\rho_{s0}}{\rho_{n0}}\left[\left(\frac{\partial P}{\partial S}\right)_0\left(\frac{\partial T}{\partial\rho}\right)_0 - \left(\frac{\partial P}{\partial\rho}\right)_0\left(\frac{\partial T}{\partial S}\right)_0\right], \tag{33}$$

$$C_4 = \frac{1}{2}\left(\frac{\partial P}{\partial\rho}\right)_0 + \frac{S_0}{2\rho_0}\left(\frac{\partial P}{\partial S}\right)_0 + \frac{S_0^2}{2\rho_0}\frac{\rho_{s0}}{\rho_{n0}}\left(\frac{\partial T}{\partial S}\right)_0. \tag{34}$$

The dynamical friction is given by the change in the energy of the perturber,

$$F_{\rm DF} = -\frac{M}{V}\frac{\partial\Phi_\alpha}{\partial t}, \tag{35}$$

where M and V are the mass and velocity of the perturber, and Φ_α is the gravitational potential of the background fluid,

$$\nabla^2\Phi_\alpha = 4\pi G\rho_0\alpha. \tag{36}$$

This is readily found in k-space,

$$\Phi_{\alpha,k} = -\frac{4\pi G\rho_0\alpha_k}{k^2}, \tag{37}$$

which can be Fourier transformed back into position-space to give the dynamical friction,

$$F_{\rm DF} = \frac{M}{V}\frac{\partial}{\partial t}\int \frac{{\rm d}k^4}{(2\pi)^4} e^{ik_0 t - i\boldsymbol{k}\cdot\boldsymbol{x}}\Phi_{\alpha,k} = -\frac{4\pi G M^2\rho_0}{V}\int \frac{{\rm d}k^4}{(2\pi)^4}\frac{ik_0}{k^2}e^{ik_0 t - i\boldsymbol{k}\cdot\boldsymbol{x}}\alpha_k. \tag{38}$$

Approximating the perturber as a point particle moving along the z-axis with constant velocity V,

$$\rho_{\rm pert}(\boldsymbol{x}, t) = M\delta(x)\delta(y)\delta(z - Vt), \tag{39}$$

or in k-space

$$\rho_{{\rm pert},k} = 2\pi M\delta(k_0 - Vk_z), \tag{40}$$

yields the expression for the dynamical friction as

$$F_{\rm DF} = \frac{32\pi^3 G^2 M^2\rho}{V}\int \frac{{\rm d}k^4}{(2\pi)^4}\frac{ik_0}{k^2}e^{ik_0 t - i\boldsymbol{k}\cdot\boldsymbol{x}} \times \frac{(k_0^2 - Ak^2)\delta(k_0 - Vk_z)}{(k_0^2 - \omega_{k+}^2)(k_0^2 - \omega_{k-}^2)}. \tag{41}$$

Equation (41) can be tackled by extending the k_0-integral into the complex place and closing it in the upper half plane (assuming $t > 0$), meaning that contour integration can be used. The poles are pushed slightly off the real line by the prescription $\omega_{k\pm} \to \omega_{k\pm} + i\epsilon$, and only the residual of the poles inside the contour contribute to the integral. Taking the limit $\epsilon \to 0^+$ after integrating gives the dynamical friction as

$$F_{\rm DF} = -\frac{16\pi^3 G^2 M^2\rho_0}{V}\int \frac{{\rm d}k^3}{(2\pi)^3}\frac{1}{k^2}\frac{1}{\omega_{k+}^2 - \omega_{k-}^2} \times \Big[e^{i\omega_{k+}t - i\boldsymbol{k}\cdot\boldsymbol{x}}(\omega_{k+}^2 - Ak^2)\delta(\omega_{k+} - Vk_z) - e^{i\omega_{k-}t - i\boldsymbol{k}\cdot\boldsymbol{x}}(\omega_{k-}^2 - Ak^2)\delta(\omega_{k-} - Vk_z)\Big]. \tag{42}$$

Spherical polar coordinates are adopted for the integral over momentum, with the polar angle θ defined as the angle relative to the direction of propagation, the z-axis, and the force is evaluated at the position of the perturber, $\boldsymbol{x} = Vt\hat{\boldsymbol{z}}$. The integrand is independent of the azimuthal angle, but depends on the polar angle through $k_z = k\cos\theta$. Integrating over the azimuthal angle therefore gives a factor 2π, while the polar angle in combination with the δ-function fixes the exponentials to one and places upper limits on the momentum, $k < k_{\rm max}^{*,\pm}$, where $k_{\rm max}^{*,\pm}$ satisfies $kV = \omega_{k\pm}$. Further constraints are placed on k: The remaining k-integral is bounded by the finite sizes of the perturber and the cloud it moves through, $R_{\rm max} = R_{\rm cloud}$ and $R_{\rm min} = R_{\rm pert}$, otherwise both ultraviolet (UV)- and infrared (IR) divergences may be encountered, because the perturber is modeled as a point particle, and the background fluid as infinite and uniform. We must also have $k > k_{\rm min}^{*,\pm}$, where $k_{\rm min}^{*,\pm}$ is the minimum momentum for which $\omega_{k\pm}$ are real. At small k, or, equivalently, large scales, where $\omega_{k\pm}$ become complex or imaginary, the background cloud will be gravitationally unstable and deform. We denote as a general measure the upper limits in k for the two terms in Eq. (42) by $k_{\rm max}^{\pm}$, and the lower limits by $k_{\rm min}^{\pm}$. Inserting the expression for $\omega_{k\pm}$ and using that $C_4 - A = C_1$, the dynamical friction becomes

$$F_{\rm DF} = -\frac{4\pi G^2 M^2\rho_0}{V^2}\Bigg[\int_{k_{\rm min}^+}^{k_{\rm max}^+}\frac{{\rm d}k}{2k}\left(\frac{C_1k^2 - C_2}{\sqrt{C_3k^4 - 2C_1C_2k^2 + C_2^2}} + 1\right) - \int_{k_{\rm min}^-}^{k_{\rm max}^-}\frac{{\rm d}k}{2k}\left(\frac{C_1k^2 - C_2}{\sqrt{C_3k^4 - 2C_1C_2k^2 + C_2^2}} - 1\right)\Bigg]. \tag{43}$$

There is an implicit criterion that $k_{\rm max}^{\pm} > k_{\rm min}^{\pm} > 0$, otherwise the integral is zero.

Equation (43) can be solved analytically, but its expression is not particularly enlightening. Instead, we focus on a few limiting cases for which the force reduces to a simplified form; zero temperature, the fully normal fluid, small velocities, and no self-gravitation.

3.1. Zero-temperature limit

Taking the limit $T \to 0$ (under the assumption that terms such as $S^2\rho_{\rm s}/\rho_{\rm n}$ go to zero as well) yields one band for the dispersion relation,

$$\omega_k^2 = c_{T=0}^2k^2 - 4\pi G\rho_0, \tag{44}$$

where the sound speed at zero temperature is

$$c_{T=0}^2 = \left(\frac{\partial P}{\partial\rho}\right)_0. \tag{45}$$

The dynamical friction becomes

$$F_{\rm DF} = -\frac{4\pi G^2M^2\rho_0}{V^2}\ln\left(\frac{k_{\rm max}}{k_{\rm min}}\right), \tag{46}$$

with

$$k_{\rm max} = \min\left(2\pi R_{\rm min}^{-1}, \sqrt{\frac{4\pi G\rho_0}{c_{T=0}^2 - V^2}}\right), \tag{47}$$

$$k_{\rm min} = \max\left(2\pi R_{\rm max}^{-1}, \sqrt{\frac{4\pi G\rho_0}{c_{T=0}^2}}\right). \tag{48}$$

3.2. Normal fluid limit

Taking the fully normal fluid limit $\rho_{\rm s} \to 0$ also gives one band for the dispersion relation,

$$\omega_k^2 = c_{\rm n}^2k^2 - 4\pi G\rho_0, \tag{49}$$

with the sound speed in the fully normal fluid

$$c_{\rm n}^2 = \left(\frac{\partial P}{\partial\rho}\right)_0 + \frac{S_0}{\rho_0}\left(\frac{\partial P}{\partial S}\right)_0. \tag{50}$$

The dynamical friction is again given by Eq. (46), but with

$$k_{\rm max} = \min\left(2\pi R_{\rm max}^{-1}, \sqrt{\frac{4\pi G\rho_0}{c_{\rm n}^2 - V^2}}\right), \tag{51}$$

$$k_{\rm min} = \max\left(2\pi R_{\rm min}^{-1}, \sqrt{\frac{4\pi G\rho_0}{c_{\rm n}^2}}\right). \tag{52}$$

This is the same as the zero-temperature case, but with a different sound speed.

3.3. Small-velocity limit

At sufficiently small velocities, $V^2 \ll C_4 - \sqrt{C_3}$, assuming that the finite sizes of the background cloud and perturber do not set the integral limits in Eq. (43), the dynamical friction becomes

$$F_{\rm DF} = -\frac{2\pi G^2 M^2 \rho_0}{c_{T=0}^2}. \tag{53}$$

This is equal to the friction force at $T = 0$ in the same limit, as opposed to when $\rho_{\rm s} = 0$;

$$F_{\rm DF} = -\frac{2\pi G^2 M^2 \rho_0}{c_{\rm n}^2}. \tag{54}$$

The dynamical friction of a superfluid therefore approaches the zero-temperature limit even when there is a significant thermal contribution. This happens because counterflow in the superfluid conspires against thermal perturbations, allowing the mass overdensity to behave similarly to a zero-temperature fluid. With only the interaction pressure that is present at zero temperature effectively damping density perturbations, the density contrast of the superfluid can grow larger (compared to a normal fluid at the same temperature) and hence produce a stronger net gravitational force acting on the perturber. However, we recall that this result does not include the effect of the critical velocity which would limit this thermal counterflow. In Sect. 4 we propose a scheme to include the critical velocity in linear perturbation theory, and then test the scheme using hydrodynamic simulations in Sect. 6.

3.4. Neglecting self-gravitation

The numerical results presented in Sect. 6, as well as the decay times of globular clusters in Sect. 7, are obtained when self-gravitation is neglected. It is therefore of interest to see what the steady-state linear theory predicts in this case as well.

Neglecting self-gravitation amounts to setting $C_2 = 0$. The dispersion relation becomes

$$\omega_{k\pm}^2 = (C_4 \pm \sqrt{C_3})k^2 = c_\pm^2 k^2. \tag{55}$$

For the equation of state used throughout this work, and $T/T_{\rm c} \lesssim 0.2$, the above superfluid sound speeds can be accurately approximated by

$$c_+ = \sqrt{\frac{c_{\rm n}^2 - c_{T=0}^2}{f_{\rm n}}}, \tag{56}$$

$$c_- = c_{T=0}. \tag{57}$$

We note that for $c_{\rm n} \gg c_{T=0}$, we have $c_+ \approx c_{\rm n}/\sqrt{f_{\rm n}} \gg c_{\rm n}$. The dynamical friction takes the form

$$F_{\rm DF} = -\frac{4\pi G^2 M^2 \rho_0}{V^2} \ln\left(\frac{R_{\rm max}}{R_{\rm min}}\right) \times \frac{1}{2}\left[\left(1 - \frac{C_1}{\sqrt{C_3}}\right)\theta(V - c_-) + \left(1 + \frac{C_1}{\sqrt{C_3}}\right)\theta(V - c_+)\right]. \tag{58}$$

One feature that is clear in this limit is that $F_{\rm DF}$ jumps from zero as V becomes larger than c_-, and jumps again as it crosses c_+. It seems odd that the force should change value so dramatically when the velocity of the perturber crosses these thresholds, and indeed we find in the numerical simulations in Sect. 5 that it does not. The problem is that in the steady-state case, as considered in this section, the linear over-density is symmetric upstream and downstream when the perturber moves at subsonic speeds, resulting in a zero net gravitational force at the position of the perturber. This is not an issue at supersonic speeds because the perturber moves faster than the background fluid can respond to the perturbation, which is at the speed of sound, resulting in a clear cone trailing the perturber (Ostriker 1999). At subsonic speeds, on the other hand, the fluid reacts faster than the perturber moves, and with an infinite amount of time to propagate this response, the first-order perturbation of the background becomes symmetric. In order to overcome this shortcoming of steady-state linear perturbation theory, other studies have broken this symmetry by switching on the perturber for a finite time (Ostriker 1999; Sánchez-Salcedo 2012), or by going to second-order perturbations (Lee & Stahler 2011; Shadmehri & Khajenabi 2012). In the following section, the finite-time approach is employed for a superfluid.

4. Dynamical friction from finite-time linear perturbation theory

For the finite-time calculation, Eqs. (26) and (27) are used without self-gravitation, and an approach very similar to the one used by Ostriker (1999) is followed.

The equations can be written in matrix form as

$$\frac{\partial^2 Y}{\partial t^2} + A\nabla^2 Y = F\rho_{\rm pert}, \tag{59}$$

where

$$Y = \begin{pmatrix} \delta\rho \\ \delta S \end{pmatrix}, \tag{60}$$

$$A = \begin{pmatrix} \left(\frac{\partial P}{\partial \rho}\right)_0 & \left(\frac{\partial P}{\partial S}\right)_0 \\ \frac{S_0}{\rho_0}\left(\frac{\partial P}{\partial \rho}\right)_0 + \frac{S_0^2}{\rho_0}\frac{\rho_{s0}}{\rho_{n0}}\left(\frac{\partial T}{\partial \rho}\right)_0 & \frac{S_0}{\rho_0}\left(\frac{\partial P}{\partial S}\right)_0 + \frac{S_0^2}{\rho_0}\frac{\rho_{s0}}{\rho_{n0}}\left(\frac{\partial T}{\partial S}\right)_0 \end{pmatrix}, \tag{61}$$

and

$$F = \begin{pmatrix} 4\pi G\rho_0 \\ 4\pi G S_0 \end{pmatrix}. \tag{62}$$

By diagonalizing matrix A, the coupled set of equations can be transformed into two decoupled wave equations of the form

$$\frac{\partial^2 \chi_i}{\partial t^2} - c_i^2 \nabla^2 \chi_i = f_i, \tag{63}$$

which are solved using the retarded Green's function for the wave equation in three dimensions:

$$\chi_i(\boldsymbol{x}, t) = \int {\rm d}^3 x' \int {\rm d}t' \, \frac{\delta(t' - (t - |\boldsymbol{x} - \boldsymbol{x}'|/c_i)) f_i(\boldsymbol{x}', t')}{4\pi c_i^2 |\boldsymbol{x} - \boldsymbol{x}'|}. \tag{64}$$

For a point source switched on at the origin at $t = 0$ and moving at speed $\boldsymbol{V} = V\hat{\boldsymbol{z}}$,

$$f_i(\boldsymbol{x}, t) = K_i \delta(x)\delta(y)\delta(z - Vt)H(t), \tag{65}$$

where $H(x)$ is the Heaviside function, the solution of χ becomes, upon defining $s = z - Vt$, $\mathcal{M}_i = V/c_i$, and $R^2 = x^2 + y^2$,

$$\chi_i(\boldsymbol{x}, t) = \frac{K_i}{4\pi c_i^2 \sqrt{s^2 + R^2(1 - \mathcal{M}_i^2)}} \mathcal{H}_i, \tag{66}$$

$$\mathcal{H}_i = \begin{cases} 1 & \text{for } R^2 + z^2 < (c_i t)^2, \\ 2 & \text{for } \mathcal{M}_i > 1, R^2 + z^2 > (c_i t)^2, \\ & s/R < -\sqrt{\mathcal{M}_i^2 - 1}, \text{ and } z > c_i t/\mathcal{M}_i, \\ 0 & \text{otherwise.} \end{cases} \tag{67}$$

The resulting overdensity $\delta\rho$ is a weighted sum of χ_+ and χ_-, and the dynamical friction is obtained by integrating the gravitational force due to the overdensity over the whole volume, that is,

$$F_{\rm DF} = 2\pi GM \int \mathrm{d}s \int \mathrm{d}R \, \frac{sR\delta\rho}{(s^2+R^2)^{3/2}}. \tag{68}$$

In spherical polar coordinates, $s = r\cos\theta = rx$ and $R = r\sin\theta = r\sqrt{1-x^2}$, we get

$$F_{\rm DF} = -\frac{4\pi G^2 M^2 \rho_0}{V^2}(\mathcal{I}_+ + \mathcal{I}_-), \tag{69}$$

$$\mathcal{I}_i = -D_i \int_{R_{\rm min}}^{R_{\rm max}} \frac{\mathrm{d}r}{2r} \int_{-1}^{1} \mathrm{d}x \, \frac{x\mathcal{M}_i^2\mathcal{H}_i}{\sqrt{1-\mathcal{M}_i^2+x^2\mathcal{M}_i^2}}, \tag{70}$$

where we have again introduced an upper and lower cutoff of scales in the integral to avoid UV- and IR divergences. The sound speeds c_+ and c_- are the same as the ones given in Eq. (55), and

$$D_+ = -\frac{S_0\left(\frac{\partial P}{\partial S}\right)_0\left[S_0\frac{\rho_{s0}}{\rho_{n0}}\left(\frac{\partial T}{\partial \rho}\right)_0 + c_+^2\right]}{\rho_0(c_+^2-c_-^2)\left[\left(\frac{\partial P}{\partial \rho}\right)_0 - c_+^2\right]}, \tag{71}$$

$$D_- = \frac{S_0\left(\frac{\partial P}{\partial S}\right)_0\left[S_0\frac{\rho_{s0}}{\rho_{n0}}\left(\frac{\partial T}{\partial \rho}\right)_0 + c_-^2\right]}{\rho_0(c_+^2-c_-^2)\left[\left(\frac{\partial P}{\partial \rho}\right)_0 - c_-^2\right]}. \tag{72}$$

The dynamical friction from the finite-time calculation is compared to the steady-state result in Fig. 1. The discontinuities have been removed, with the force increasing with velocity V until it reaches a maximum near the sound speed, after which the perturber becomes supersonic and the friction force decreases with the same $1/V^2$ dependence as in the steady-state result. As time passes, the finite-time result approaches the steady-state result, as expected.

Both approaches predict $F_{\rm DF}$ in the superfluid phase to be very close to the zero-temperature value, even when thermal pressure dominates over the contribution from self-interactions. However, we must recall again that the Landau criterion is not included in linear perturbation theory, which will limit the thermal counterflow of the superfluid, making it behave more like a normal fluid, thus decreasing the dynamical friction as thermal pressure forces inhibit the growth of density perturbations. Let us therefore construct an ad hoc scheme to include the critical velocity in the linear theory.

The critical velocity is expected to have an effect when the relative velocity is of the order of the critical velocity and larger. Therefore, let us consider the linearized equation for the relative velocity,

$$\frac{\partial \boldsymbol{w}}{\partial t} = \frac{S_0}{\rho_{n0}}\boldsymbol{\nabla}\delta T = \frac{S_0}{\rho_{n0}}\left[\left(\frac{\partial T}{\partial S}\right)_0 \boldsymbol{\nabla}\delta S + \left(\frac{\partial T}{\partial \rho}\right)_0 \boldsymbol{\nabla}\delta\rho\right]. \tag{73}$$

The amplitude of $\delta\rho$ and δS, and hence δT, increases with M, driving w up to the critical value faster, causing the effect of the critical velocity on the system to be more prominent. Increasing M should therefore have a similar effect as lowering $v_{\rm c}$ in transitioning the superfluid dynamical friction from the $T = 0$ value to the fully normal fluid value.

We now assume that for an estimate of the characteristic counterflow $\bar{w}$ of the system, there is an interpolating function $f(\bar{w}, v_{\rm c})$ with $f(\bar{w} \ll v_{\rm c}) \to 1$, $f(\bar{w} \gg v_{\rm c}) \to 0$, and a transitional region around $\bar{w} \sim v_{\rm c}$, such that

$$F_{\rm DF} = f(\bar{w}, v_{\rm c})F_{\rm DF}^{\rm sf} + [1 - f(\bar{w}, v_{\rm c})]F_{\rm DF}^{\rm nf}, \tag{74}$$

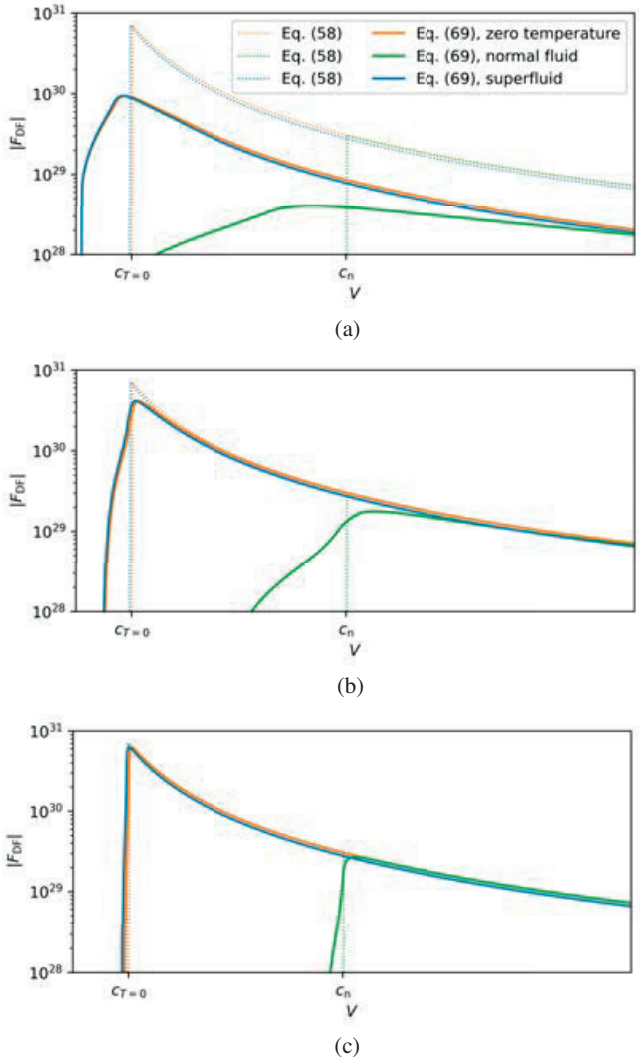

Fig. 1. Dynamical friction from linear perturbation theory using the finite-time approach (solid lines) and the steady-state approach (dotted lines) as a function of V. As time passes, the finite-time result, Eq. (69), approaches the steady-state result, Eq. (58). In the zero-temperature limit, we have $T = 0$, while in the normal fluid case we have $\rho_{\rm s} = 0$. (*a*) $t = 0.1R_{\rm max}/V$. (*b*) $t = R_{\rm max}/V$. (*c*) $t = 10R_{\rm max}/V$.

where $F_{\rm DF}^{\rm sf}$ and $F_{\rm DF}^{\rm nf}$ is the dynamical friction from linear theory for the superfluid and fully normal fluid, respectively. Using Eq. (73) we can write

$$\bar{w} = \frac{S_0}{\rho_{n0}}\frac{\delta T(0)}{L}\Delta t = \frac{S_0}{\rho_{n0}}\left[\left(\frac{\partial T}{\partial S}\right)_0 \frac{\delta S(0)}{L} + \left(\frac{\partial T}{\partial \rho}\right)_0 \frac{\delta\rho(0)}{L}\right]\Delta t. \tag{75}$$

The length L and time Δt are characteristic scales over which the fluid attains the mass and entropy overdensity at the origin, $\delta\rho(0)$ and $\delta S(0)$. The timescale can be estimated as $\Delta t = L/v$, where v is some characteristic velocity in the problem. The largest superfluid sound speed, c_+, which is essentially the fastest speed with which the superfluid can respond to disturbances, was found to work.

For the δ-function perturbation, the central values for the mass and entropy overdensities diverge in the linear theory, meaning that $\delta\rho(0)$ and $\delta S(0)$ are not well-defined. Instead, these

should be evaluated at some point near the origin, as was done for dynamical friction. With the equation of state used in this work, an estimate of the linear entropy contrast at $R_{\rm min}/2$ is

$$\delta S\,(R_{\rm min}/2) \approx \frac{2S_0 GM}{c_+^2 R_{\rm min}}. \tag{76}$$

The rough estimate of the counterflow is therefore

$$\bar{w} = \frac{S_0^2}{\rho_{n0}}\left(\frac{\partial T}{\partial S}\right)_0 \frac{2GM}{c_+^3 R_{\rm min}}. \tag{77}$$

Only the form of the interpolating function $f(\bar{w}, v_{\rm c})$ remains to be specified. The simple but rather arbitrary choice,

$$f(\bar{w}, v_{\rm c}) = \frac{v_{\rm c}}{v_{\rm c} + \bar{w}} = \left[1 + \frac{S_0^2}{\rho_{n0}}\left(\frac{\partial T}{\partial S}\right)_0 \frac{2G}{c_+^3 R_{\rm min}}\frac{M}{v_{\rm c}}\right]^{-1}, \tag{78}$$

was found to work well, as we see in Sect. 6.

5. Numerical simulation of dynamical friction

To test the calculations from linear perturbation theory, the full superfluid equations are integrated numerically. We use the frame comoving with the perturber, meaning that its gravitational field is static and centered at the origin, while the background fluid is moving. We take the perturber to be a sphere with uniform mass density $\rho_{\rm pert} = 3M/4\pi R_{\rm pert}^3$. The system has rotational symmetry, and so cylindrical coordinates are employed; the axial distance is z, the distance along the axis of rotational symmetry, and the radial distance is r, the distance from the axis. The simulation volume is therefore a cylinder, and we take its domain to be $-L < z < L$ and $0 < r < L$.

The superfluid is initialized as a uniform fluid moving with velocity $\boldsymbol{V} = -V\hat{z}$. More fluid is injected into the simulation volume with the same velocity at the $z = +L$ boundary. The $z = -L$ and $r = L$ boundaries are taken to have zero gradients, while the inner boundary $r = 0$ has a reflecting boundary condition.

To numerically integrate the superfluid equations, a Godunov scheme similar to the one described in Hartman et al. (2020) is used. In the present work, the generation of entropy when the Landau criterion is broken is not included. Also, as we evolve the entropy instead of the energy, and we do not include any viscosity, the numerical scheme dissipates kinetic energy at shock fronts that is not converted into internal energy. In the absence of this shock heating, the total energy is not strictly conserved. Nevertheless, we have found that this inaccuracy is by and large negligible for the scenarios we consider here because the solutions are mostly in or near the linear regime.

The self-gravitation of the superfluid is neglected. The gravitational field it produces is computed only to find the resulting force on the perturber, that is, the dynamical friction. The initial fluid parameters are $\rho = 2 \times 10^7\, M_\odot\,{\rm kpc}^{-3}$, $T = 0.2T_{\rm c}$, $m = 500\,{\rm eV}$, and $g = 2 \times 10^{-3}\,{\rm eV}^{-2}$. These parameters are chosen only to illustrate the basic features of dynamical friction in superfluids while keeping the simulation run-times reasonably short. Unless stated otherwise, the size of the perturber is taken to be $R_{\rm pert} = 2\,{\rm pc}$ with mass $M = 0.1\,M_\odot$, while the simulation size is $L = 150\,{\rm pc}$. The simulation is run until $t = 10\,{\rm pc}/V$, that is, until the background has moved 10 pc. This is small compared to the full simulated length, but is necessary for preventing boundary effects from interfering with the results. $R_{\rm min}$ is taken to be the size of the perturber, $R_{\rm min} = 2\,{\rm pc}$, and $R_{\rm max}$ the radius of the cylindrical simulation volume, $R_{\rm max} = 150\,{\rm pc}$, when compared to linear perturbation theory. The resolution of the simulated volume is 4096×2048 cells, in the z and r directions, respectively, for the superfluid case. In the zero-temperature and normal fluid limits, for which the numerical scheme was made second-order in time and space using a MinMod slope-limited MUSCL-Hancock scheme (Toro 2006) without stability issues, a lower resolution of 2048×1024 is used.

An effective critical velocity $v_{\rm c}^{\rm eff}$, which is just $v_{\rm c}$ multiplied by some factor, is used in the simulations to show the effect of varying $v_{\rm c}$ without actually changing other parameters such as the particle mass and self-interaction.

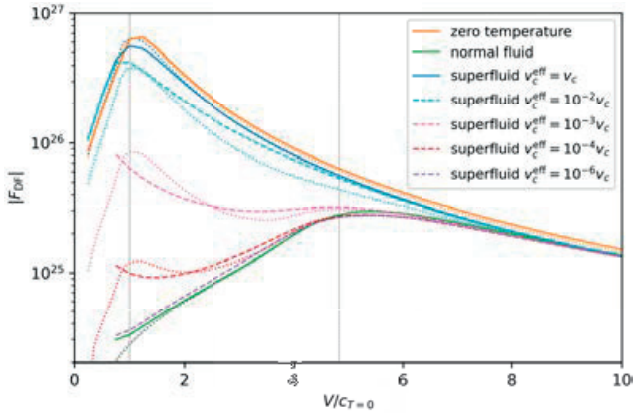

Fig. 2. Dynamical friction against velocity for the superfluid with varying $v_{\rm c}^{\rm eff}$, and for the zero temperature and the fully normal fluid limits. The results from finite-time linear perturbation theory are shown with dotted lines of the same colors. Even with the critical velocity included, the superfluid case gives a dynamical friction force of the same magnitude as the zero temperature limit. When $v_{\rm c}^{\rm eff}$ is decreased, the superfluid approaches the fully normal fluid limit as thermal counterflow is increasingly limited. The sound speeds $c_{T=0}$ and $c_{\rm n}$ are indicated by the vertical dotted lines.

6. Comparison of perturbation theory and numerical simulation

In Fig. 2 the dynamical friction from the numerical simulations is compared to the linear result with the effect of the critical velocity included, Eqs. (69), (74), and (78). Even with the Landau criterion, given by Eq. (18), the dynamical friction in the superfluid can be very similar to the zero-temperature limit, as was shown in the linear theory. This similarity can also be seen in the mass density profile shown in Fig. 3. At $T = 0$, for which the pertuber is supersonic with $V = 1.5c_{T=0}$, there is a well-defined supersonic cone that trails the pertuber, and the density contrast reaches about 4.5. The finite-temperature superfluid has a similar density contrast and supersonic cone, though not as well-defined, illustrating that the superfluid behaves like the $T = 0$ limit as thermal counterflow suppresses thermal perturbations. In the fully normal fluid case, the density contrast is much smaller, around 0.17, and the perturber is instead moving at subsonic speeds, because $V = 1.5c_{T=0} < c_{\rm n}$, hence there is no sonic cone. As $v_{\rm c}^{\rm eff}$ is decreased, the relative velocity becomes increasingly limited and the thermal counterflow inefficient, causing the superfluid density profile to approach the fully normal fluid limit. The dynamical friction changes accordingly, as shown in Fig. 4. Furthermore, Fig. 5 shows the friction force as a function of the mass of the perturber M, confirming the expectation that

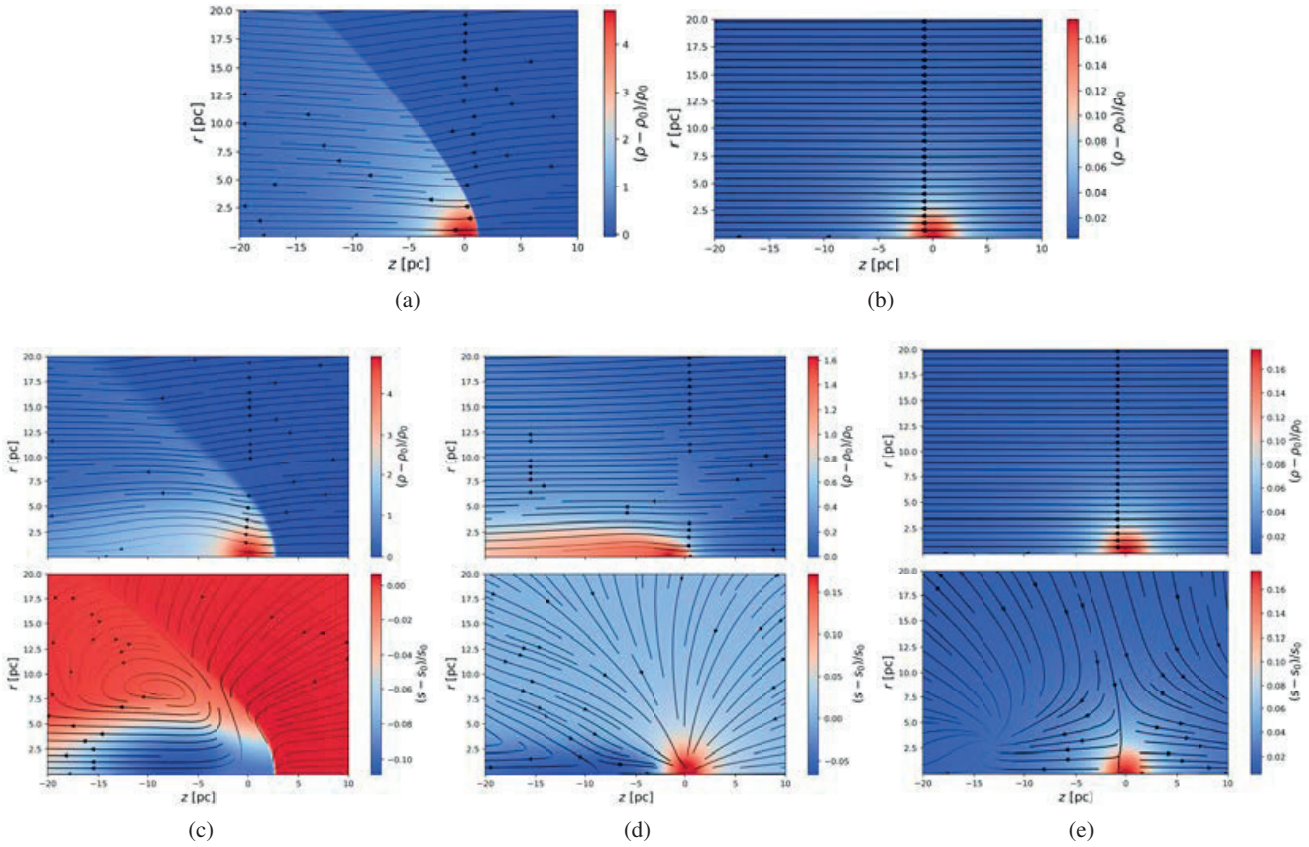

Fig. 3. Density profiles and streamlines for $V = 1.5c_{T=0}$. The mass density profiles are superimposed by the net mass density velocity, $\boldsymbol{v} = \boldsymbol{j}/\rho$, while the entropy density is superimposed by the relative velocity $\boldsymbol{w} = \boldsymbol{v}_s - \boldsymbol{v}_n$. The perturber has mass $M = 5\,M_\odot$, the simulation volume is $L = 75$ pc, and the time is $t = 50\,\mathrm{pc}/V$. (*a*) $T = 0$ limit. (*b*) $\rho_s = 0$ limit. (*c*) $v_c^{\mathrm{eff}} = v_c$. (*d*) $v_c^{\mathrm{eff}} = 10^{-1}v_c$. (*e*) $v_c^{\mathrm{eff}} = 10^{-5}v_c$.

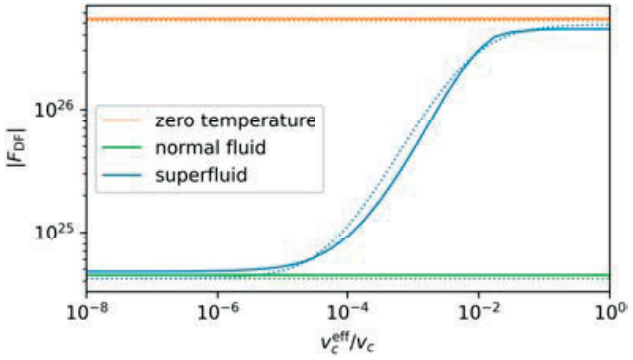

Fig. 4. Dynamical friction against the effective critical velocity v_c^{eff}, for $V = 1.5c_{T=0}$, with the results from finite-time linear perturbation theory included with dotted lines of the same colors. As v_c^{eff} is lowered, the dynamical friction goes from about the same value as the zero temperature limit to the value in the fully normal fluid limit, changing by about two orders of magnitude.

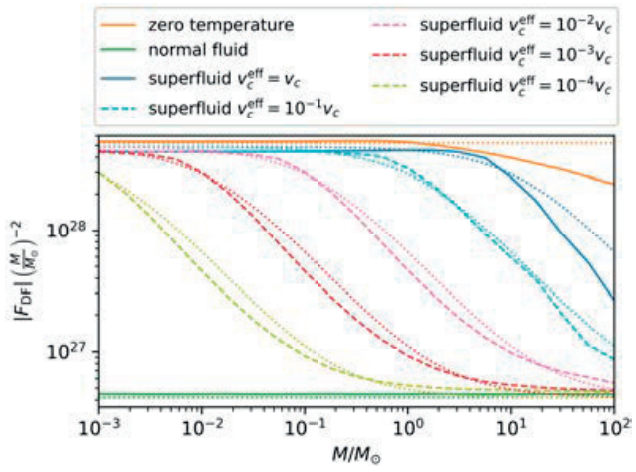

Fig. 5. Dynamical friction against the perturber mass M, for $V = 1.5c_{T=0}$, with the results from finite-time linear perturbation theory included with dotted lines of the same colors. The departure from perturbation theory for the zero-temperature case at high M is due to nonlinear effects. Increasing the mass of the perturber causes the superfluid to behave increasingly like a normal fluid, similarly to the effect of decreasing v_c^{eff}.

increasing M causes a transition from superfluid to normal fluid behavior in a similar manner to decreasing v_c.

The numerical results of Figs. 2, 4, and 5 show that the scheme to include v_c in the linear theory (Eqs. (74) and (78)) successfully captures the basic dependence on the perturber mass and critical velocity, though it fails at low velocities, $V < c_{T=0} \approx c_-$, suggesting that other factors might come into play at those speeds. However, as we see in the following section, this does not cause any problems when applied to the Fornax dSph, as in the relevant parameter space we have $\bar{w} \ll v_c$, which is far away from the transition between the superfluid and normal

Table 1. Halo mass profile parameters, using Eq. (80), with values from Cole et al. (2012).

Model	Name	γ_0	γ_∞	η	r_s [kpc]	M (1.8 kpc) [$10^8\,M_\odot$]	$\bar{\rho}$ [$10^8\,M_\odot\,\mathrm{kpc}^{-3}$]
LC	Large core	0.07	4.65	3.7	1.4	4.12	0.35
WC	Weak cusp	0.08	4.65	2.77	0.62	1.03	0.71

Notes. The density parameter $\bar{\rho}$ is computed from the mass enclosed within 1.8 kpc.

fluid phase, and therefore no interpolation is needed. No further attempt was therefore made to improve the scheme.

7. Application to the Fornax system

So far, only the physics of dynamical friction in superfluids has been discussed, with little reference to the real world. Now, armed with the expressions derived and tested in the previous sections, the parameter space of superfluid DM–the particle mass, self-interaction, and temperature–can be explored by estimating the orbital decay time of GCs in the Fornax dSph, and checking whether the timing problem is alleviated for SIBEC-DM, or exacerbated.

The decay time can be defined as the time $\tau_{\rm DF}$ it takes dynamical friction to reduce the angular momentum L of the GCs to zero;

$$\tau_{\rm DF} = \frac{L}{r|F_{\rm DF}|} = \frac{MV}{|F_{\rm DF}|}, \tag{79}$$

where M, V, and r are the mass, circular orbital velocity, and the orbital radius of the GCs. The density profile of the Fornax dSph is modeled in the same way as in Cole et al. (2012), using a spherical double-power-law profile[1] of the form

$$\rho(r) = \bar{\rho}\left(\frac{r}{r_s}\right)^{-\gamma_0}\left[1+\left(\frac{r}{r_s}\right)^{\eta}\right]^{\frac{\gamma_0-\gamma_\infty}{\eta}}. \tag{80}$$

The profile parameters, still following Cole et al. (2012), are listed in Table 1, and correspond to different models for the shape of the Fornax dSph. As SIBEC-DM, like many alternative theories for DM, is in part motivated by typically having a cored profile, we only focus on the Large core (LC) and Weak cusp (WC) models from Cole et al. (2012). It should also be noted that the density profile Eq. (80) models the total mass density, that is, both stellar and DM, but as DM is the dominant component, we use it as a pure DM profile. As illustrated in Fig. 6, subtracting a subdominant portion of the density $\rho_0 = \rho(r)$ in the computation of the SIBEC-DM dynamical friction in order to account for the presence of stellar mass does not significantly alter the value of the orbital decay time.

Estimates of the masses, projected orbital radii $r_\perp$, and core radii r_c of the GCs, which we use as $R_{\rm min}$ in perturbation theory, are listed in Table 2. As in Lancaster et al. (2020) and Hui et al. (2017), $r = 2r_\perp/\sqrt{3}$ is used as the "true" radial distance from the Fornax center. This larger radial distance leads to a longer estimate of the decay time $\tau_{\rm DF}$, as illustrated in Fig. 6. The orbital velocities of the GCs are assumed to be circular, determined by the total halo mass enclosed by their orbits, $M_{\rm encl}$,

$$V = \sqrt{\frac{GM_{\rm encl}}{r}}. \tag{81}$$

[1] There appears to be a sign error in Eq. (1) in Cole et al. (2012) when comparing the resulting profiles to their own figures, as well as compared to other works that use the same type of profile (Zhao 1996; Walker et al. 2009; Hague & Wilkinson 2013).

Table 2. Projected radial distances, masses, and core radii of the GCs (not including the sixth found by Wang et al. 2019b) in the Fornax dSph, taken from Mackey & Gilmore (2003).

GC label	Projected radial distance $r_\perp$ [kpc]	GC core radius r_c [pc]	Mass M [$10^5\,M_\odot$]
GC1	1.6	10.03	0.37
GC2	1.05	5.81	1.82
GC3	0.43	1.60	3.63
GC4	0.24	1.75	1.32
GC5	1.43	1.38	1.78

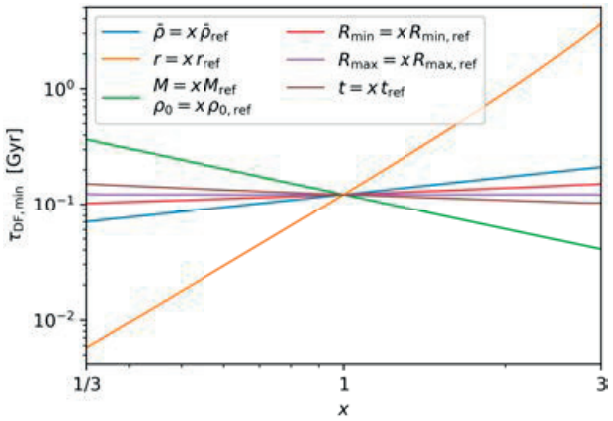

Fig. 6. Change in the orbital decay time as parameters related to the modeling of the Fornax dSph, the GCs, and the dynamical friction are varied. The reference values, which are for GC3 in the LC model, are labeled with the subscript "ref".

Inside r_s the density profile of the Fornax dSph is approximately constant and cored for the LC and WC models. Hence, we use r_s as the "core size" of the Fornax, R_c, and the upper length scale when we use perturbation theory, $R_{\rm max}$. The DM density is determined at the position of the GCs using Eq. (80).

There is a limited region of parameter space that is both physically relevant, and may provide a reasonable estimate of $\tau_{\rm DF}$. This region should satisfy the following:

- The core radius of the halo obtained from hydrostatic equilibrium should not exceed the core radius of the dSph as modeled by Eq. (80).
- The DM mass and self-interaction should satisfy constraints from observations of the deceleration of DM in cluster collisions (Harvey et al. 2015).
- The relaxation rate of DM should be higher than the rate of dynamical changes in the dSph, so that the system can thermalize and form a superfluid.
- Perturbation theory is only properly valid for $\delta\rho/\rho \ll 1$.

– The ad hoc scheme to include the critical velocity introduced at the end of Sect. 4 failed to reproduce the numerical results of Sect. 6 for velocities $V < c_-$. Therefore, we cannot trust the dynamical friction obtained from linear perturbation theory for these velocities. However, this should only be a problem near the transition $\bar{w} \sim v_c$, where the form of interpolation between the superfluid and normal fluid result is important.

While this list is not exhaustive, it provides a minimum set of criteria that should be fulfilled. Due to our ignorance of the general behavior of superfluid DM in a number of situations, we enforce relaxed variants of the above constraints.

As seen in the previous sections, and shown in an earlier work (Hartman et al. 2020), counterflow can effectively redistribute thermal energy in a superfluid. Therefore, the shape of the temperature profile of a realistic superfluid DM halo is unknown. The least constraining assumption is therefore made; that the counterflow has washed out any significant thermal differences, so that only the interaction part of the pressure (the only pressure present at $T = 0$) determines the hydrostatic profile. Demanding that the core radius of the halo be larger than the core radius obtained from hydrostatic equilibrium, which we define as $\rho(R_c) \approx \rho(0)/2$, gives

$$g \lesssim \pi G R_c^2 m^2. \tag{82}$$

This relaxed constraint is only possible if it is physically feasible for the counterflow to transport a significant portion of the thermal energy away from the halo core. A supplementary criterion can be derived by demanding that the total entropy flux due to thermal counterflow at the core edge R_c, with $w = v_c$, be of the same order as the total entropy enclosed in R_c. This leads to

$$g \gtrsim \frac{m^2}{9\rho}\frac{R_c^2}{\Delta t^2}, \tag{83}$$

where Δt should be smaller than the age of the dSph, for example $\Delta t \sim 1$ Gyr. As shown in Fig. 7, the difference between the $T = 0$ and the finite temperature treatment of the hydrostatic halo size can be very large, and we do not expect a realistic superfluid halo to be able to completely remove thermal differences, even if upper estimates of the thermal counterflow suggest it could. A realistic superfluid core radius is therefore expected to be larger than the zero-temperature estimate used to derive Eq. (82).

By measuring the spatial offset of stars, gas, and DM in colliding galaxy clusters, a constraint on the self-interaction cross section of DM, σ, can be established (Harvey et al. 2015). The lack of deceleration of DM and its proximity to the collisionless stars in these collisions places an upper limit of $\sigma/m \lesssim 0.5\,\mathrm{cm^{-2}\,g^{-1}}$. In terms of the self-interaction parameter g, this constraint reads (Pitaevskii & Stringari 2016)

$$g = \frac{\sqrt{4\pi\sigma}}{m} \lesssim 5 \times 10^{-12}\left(\frac{1\,\mathrm{eV}}{m}\right)^{1/2} \mathrm{eV}^{-2}. \tag{84}$$

While the above places upper limits on g, there is also a lower limit that must be considered given by the criterion that the DM superfluid should be thermalized across much of the halo core. For this we require the relaxation rate of DM, Γ_{DM}, to be higher than the rate of dynamical changes in the halo core, $\Gamma_{\mathrm{grav}} \sim \sqrt{G\rho}$. For two-body interactions, the relaxation rate is $\Gamma \sim n\sigma\delta v$, where σ is the scattering cross-section and δv the velocity dispersion of the particles. In terms of g, as above, the cross-section is $\sigma = m^2 g^2/4\pi$. However, for a condensed Bose gas, the relaxation rate is enhanced, that is, $\Gamma \sim \mathcal{N} n\sigma\delta v$, where

$$\mathcal{N} = n\frac{(2\pi)^3}{\frac{4\pi}{3}(m\delta v)^3}, \tag{85}$$

because of the high occupation number of the ground state (Sikivie & Yang 2009). Using $\delta v \sim V$, that is, that the DM velocity dispersion is of the same order as the GC orbital velocity, the criterion $\Gamma_{\mathrm{DM}} > \Gamma_{\mathrm{grav}}$ becomes

$$g \gtrsim \sqrt{\frac{2}{3\pi}}\frac{m^{3/2}G^{1/4}V}{\rho^{3/4}}. \tag{86}$$

It should be noted that the enhancement factor is included in this criterion, but not in the constraint from cluster collisions. This is another example of a relaxed constraint due to our ignorance of how the superfluid properties might change in the various situations. The characteristic speeds of cluster collisions are usually much higher than inside halos, which might result in a much larger disruption of the DM BEC. Furthermore, the DM fluid may not even be condensed throughout most of the cluster, only inside dense structures. We therefore choose the least restrictive constraint by including $\mathcal{N}$ inside the dSph DM halo, but not outside.

The remaining constraints due to $\delta\rho/\rho \ll 1$ and $V < c_-$ are readily obtained from perturbation theory and Eq. (57). The result from the finite-time approach, Eq. (69), with our proposed scheme for including the critical velocity, Eqs. (74) and (78), is used to compute the dynamical friction. The characteristic timescale $t = r/V$ is used as the finite time the perturber has

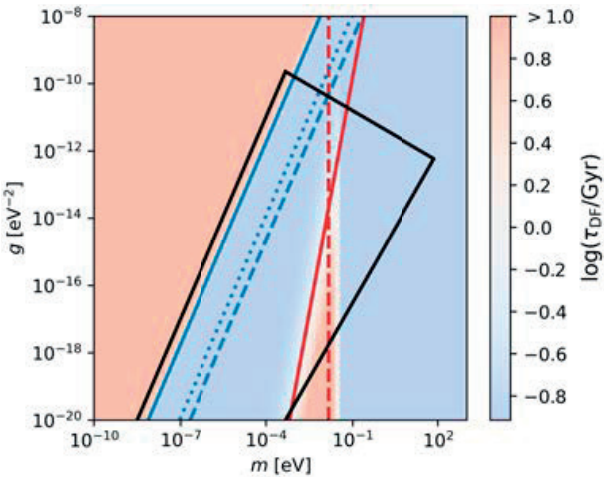

Fig. 7. Criteria listed in the text, and the orbital decay timescale for GC3 at $T/T_c = 10^{-4}$ in the LC model for reference (solid black line). Permitted parameter space; the left side is from the constraint on the halo core radius in hydrostatic equilibrium, Eq. (82); the upper right side from the constraint from galaxy cluster collisions, Eq. (84); and the lower right side from the minimum relaxation rate needed to thermalize the fluid across the halo, Eq. (86) (solid blue line). $V = c_-$, with $V < c_-$ on the left side (dotted blue line). Criterion for linear perturbation theory to be properly valid, with $\delta\rho/\rho_0 < 1$ satisfied on the left side (dashed blue line). Supplementary criterion for the $T = 0$ treatment of the hydrostatic halo size, with Eq. (83) satisfied on the left side (solid red line). $\bar{w} = v_c$, where the superfluid dynamical friction transitions from superfluid on the left side, to normal fluid on the right (dashed red line). Constraint on the halo core radius in hydrostatic equilibrium with thermal pressure included, with halo cores smaller than the core as modeled by Eq. (80) on the right side.

been active, though the results are not sensitive to this choice. A deficiency of the finite-time formalism is the lack of self-gravitation in the background fluid, and it might seem that a better choice is to instead use the steady-state expression, Eq. (43), which includes this property. However, that result assumes the perturber has acted on an otherwise static background for an infinite amount time, and does not take into account that the background can be rotationally supported, and therefore resist the large-scale gravitational collapse induced by the perturber. Furthermore, numerical studies of dynamical friction in realistic halos show that linear theory can provide reasonable estimates of the gravitational drag force even with self-gravitation neglected if the mass of the perturber is significantly smaller than the mass of the host halo (Fujii et al. 2006; Aceves & Colosimo 2007; Binney & Tremaine 2008; Chapon et al. 2013; Antonini & Merritt 2011; Tamfal et al. 2020), as is the case here. However, because linear perturbation theory assumes a uniform background with an upper cutoff of scales to take into account the finite extent of the background, we focus on the GCs located inside r_s, where the density profile of the LC and WC models are approximately flat, which are GC3 and GC4. These are also the ones that the timing-problem usually applies too (Cole et al. 2012; Hui et al. 2017; Arca-Sedda & Capuzzo-Dolcetta 2017).

The criteria on the parameter space listed above are illustrated in Fig. 7 for GC3 in the LC profile, with the estimated orbital decay time for reference. Some features that also hold for the other cases shown in Fig. 8 are worth pointing out. First, the transition point between superfluid and normal fluid behavior, $\bar{w} = v_c$, lies far away from the region $\delta\rho/\rho_0 < 1$ where perturbation theory is valid, meaning that we do not need to worry about the accuracy of the interpolation scheme described in Sect. 4. Second, the decay time becomes very large for $V < c_-$, because, as we have seen in the previous sections, the dynamical friction vanishes quickly for velocities below the lowest sound speed.

The orbital decay time for a wide range of parameters is shown in Fig. 8 for the two GCs inside the core radius of the Fornax dSph, GC3 and GC4, in the two density profiles considered. τ_{DF} generally either attains a minimum value, $\tau_{DF,min}$, or approaches infinity. The minimum values in the region $V > c_-$ and $\delta\rho/\rho_0 < 1$ are summarized in Table 3, with τ_{DF} in the range 67 Myr−197 Myr. These timescales are considerably smaller than the CDM result assuming the same density profiles, 515 Myr−1327 Myr, with the dynamical friction given by Binney & Tremaine (2008)

$$F_{DF,CDM} = -\frac{4\pi M^2 G^2 \rho_0 \ln\Lambda}{V^2}\left[\mathrm{erf}(X) - \frac{2X}{\sqrt{\pi}}e^{-X^2}\right], \tag{87}$$

where $\Lambda \approx r\delta v^2/GM$, $X = V/\sqrt{2}\delta v$, δv is the velocity dispersion of CDM particles, taken to be $\delta v \approx V$, and erf is the error function.

The decay time remains small even if parameters used to model the Fornax dSph, the GCs, and the dynamical friction are varied, as illustrated in Fig. 6. A notable exception is the position of the GC, for which τ_{DF} is considerably shorter when closer to the halo center, and likewise longer when further away. This implies that the value for τ_{DF} obtained from Eq. (79) overestimates the time it takes the GC to fully decay from its current position, but it also implies that the migration towards the halo center was slower in the past when the GCs were at larger radial distances. Indeed, estimates of $\tau_{DF,min}$ for GC1, GC2, and GC5, all of which are located at $r \gtrsim 1$ kpc, give decay times in excess of 4 Gyr. In the CDM case, the decay times for these GCs are even longer: 17 Gyr and more. These estimates do not suggest a timing problem for the outer GCs, even if their decay times are considerably shorter for SIBEC-DM compared to CDM. However, we note that these GCs are near or outside the radius r_s, where the density profile of the dSph falls sharply, and therefore we do not expect the result for the dynamical friction, nor Eq. (79), to necessarily provide a reasonable estimate of τ_{DF}. Nonetheless, the present results show that for a large region of the relevant parameter space of the SIBEC-DM model considered here, GC3 and GC4 are currently racing towards the center of their host halo in a SIBEC-DM universe.

Let us now consider τ_{DF} in light of constraints on the SIBEC-DM model from the literature. By fitting rotation curves of slowly rotating SIBEC-DM halos in hydrostatic equilibrium in 173 nearby galaxies from the *Spitzer* Photomery & Accurate Rotation Curves (SPARC) data (Lelli et al. 2016), Crăciun & Harko (2020) estimated the properties of SIBEC-DM halos at $T = 0$, and found the best fit values for g/m^2 to be between $2.7\times10^{-4}\,\mathrm{eV}^{-4}$ and $5.0\times10^{-2}\,\mathrm{eV}^{-4}$. For reference, the estimated limit from hydrostatic equilibrium using Eq. (82) gives g/m^2 of less than about $2\times10^{-4}\,\mathrm{eV}^{-4}$ or $10^{-3}\,\mathrm{eV}^{-4}$, depending on the profile used for the dSph. As the preferred values obtained by Crăciun & Harko (2020) for zero-temperature SIBEC-DM satisfy $V < c_-$ for the GCs and dSph profiles considered, leading to a vanishing dynamical friction, the $T = 0$ case does not have a timing-problem, a result that could also have been found using heuristic arguments; if the halo is largely supported by hydrostatic pressure, that is, its Jeans' length $R_J \sim c_s/\sqrt{G\rho}$ is of the order of the DM halo core radius R_c, then density perturbations on smaller scales inside the halo will be highly suppressed, resulting in very weak dynamical friction, and therefore long decay times.

In a finite-temperature SIBEC-DM halo–for which we expect the preferred values for g/m^2 obtained from fitting rotation curves to be lowered, as it provides additional pressure forces to support DM halos–the present results instead suggest that overly large orbital decay rates due to strong dynamical friction may arise. This is the opposite of what one would naively expect if the superfluid had been treated as a conventional thermal fluid, because an increased pressure generally leads to a smaller maximum dynamical friction. Instead, the superfluid essentially ignores the thermal contribution, and responds to a perturber as if it were at $T = 0$, which can yield a much stronger friction force.

8. Conclusion

We investigated the dynamical friction acting on an object due to a superfluid background, starting with steady-state linear perturbation theory. The well-known issue of discontinuities in the friction force as the perturber's velocity crosses the fluid sound speed was encountered. We therefore also employed a finite-time formalism, which removed these discontinuities, agreeing with previous studies that the dynamical friction increases with the velocity of the perturber until the sound speed is reached, after which the force decreases with the same V^{-2} dependence as the steady-state result. Both approaches predict the force in the superfluid phase to be very similar to the $T = 0$ limit, even when there are large thermal contributions, yielding a much stronger friction force than one might naively expect when compared to a conventional fluid at the same temperature. This happens because counterflow conspires against thermal perturbations, allowing the superfluid to respond to a perturbation as if it were at zero temperatures. However, the counterflow is only effective as long as it does not exceed the critical velocity v_c,

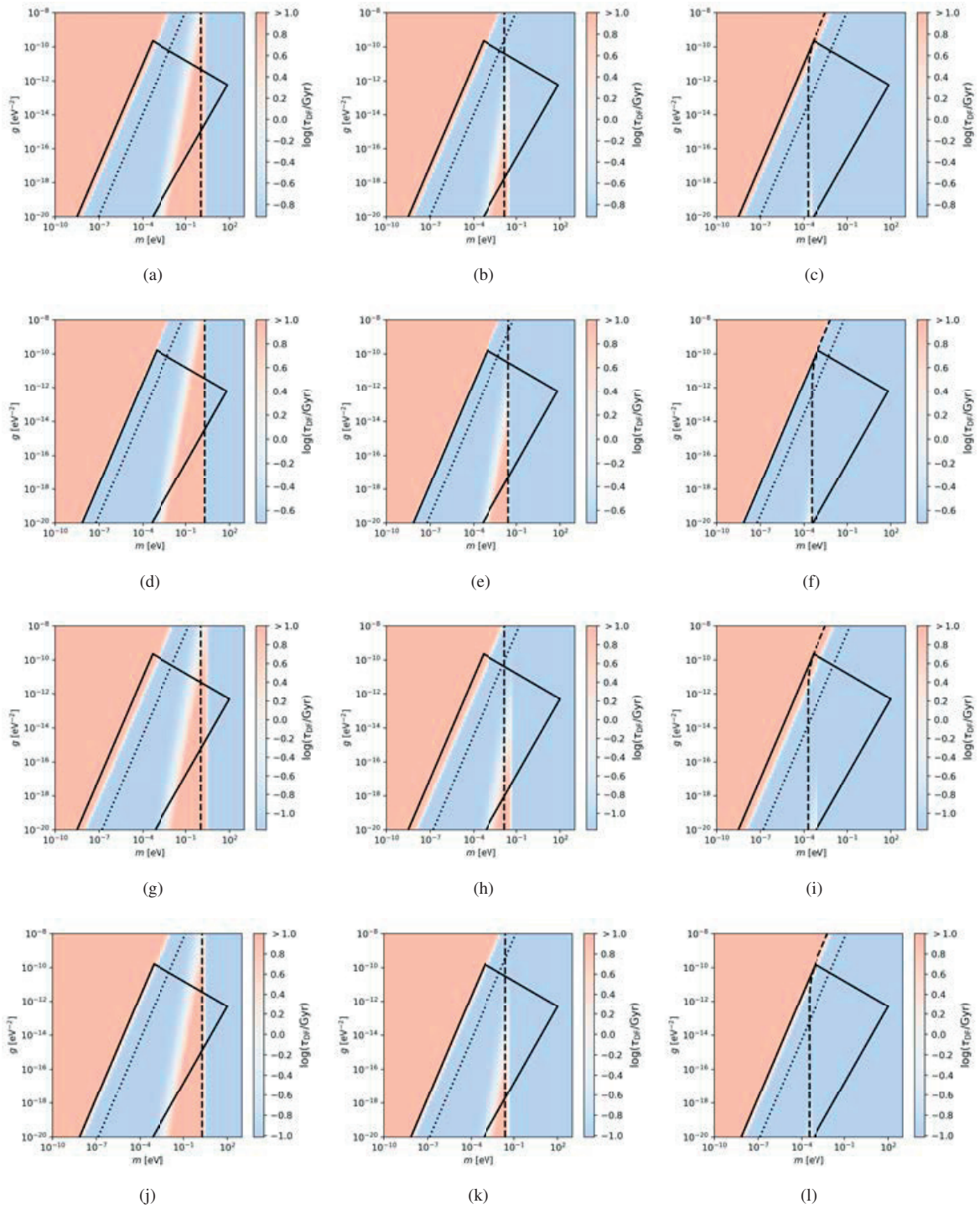

Fig. 8. Decay time of GC3 and GC4, as listed in Table 2, in the LC and WC models for the Fornax dSph density profile from Table 1 (solid line). Permitted parameter space; the *left side* is from the constraint on the halo core radius in hydrostatic equilibrium, Eq. (82); the *upper right side* from the constraint from galaxy cluster collisions, Eq. (84); and the *lower right side* from the minimum relaxation rate needed to thermalize the fluid across the halo, Eq. (86) (dotted line). Criterion for linear perturbation theory to be properly valid, with $\delta\rho/\rho_0 < 1$ satisfied on left side (dashed line). Limit due to a hydrostatic halo with thermal pressure included, with resulting core radii smaller than the core of the Fornax dSph as modeled by Eq. (80) to the right. Changing the temperature only changes the decay time of the normal fluid phase, as well as the crossover from superfluid to normal fluid. However, for the temperatures shown and lower, the normal phase is well outside the parameter space where perturbation theory is valid. (*a*) GC3 LC, $T/T_c = 10^{-2}$. (*b*) GC3 LC, $T/T_c = 10^{-4}$. (*c*) GC3 LC, $T/T_c = 10^{-6}$. (*d*) GC3 WC, $T/T_c = 10^{-2}$. (*e*) GC3 WC, $T/T_c = 10^{-4}$. (*f*) GC3 WC, $T/T_c = 10^{-6}$. (*g*) GC4 LC, $T/T_c = 10^{-2}$. (*h*) GC4 LC, $T/T_c = 10^{-4}$. (*i*) GC4 LC, $T/T_c = 10^{-6}$. (*j*) GC4 WC, $T/T_c = 10^{-2}$. (*k*) GC4 WC, $T/T_c = 10^{-4}$. (*l*) GC4 WC, $T/T_c = 10^{-6}$.

Table 3. Minimum orbital decay time $\tau_{\rm DF,min}$ of GC3 and GC4 in the LC and WC models for the Fornax dSph, found in the region $V > c_-$ and $\delta\rho/\rho_0 < 1$ (for which perturbation theory is properly valid), with the CDM result given by Eq. (87) for comparison.

GC label and model	$\tau_{\rm DF,min}$ [Myr]	$\tau_{\rm DF,CDM}$ [Myr]	$V > c_-$	$\delta\rho/\rho_0 < 1$	Equation (82)
GC3 & LC	122	883	$g/m^2 < 1.8 \times 10^{-4}$	$g/m^2 > 1.2 \times 10^{-6}$	$g/m^2 < 1.0 \times 10^{-3}$
GC3 & WC	197	1327	$g/m^2 < 2.5 \times 10^{-4}$	$g/m^2 > 2.7 \times 10^{-6}$	$g/m^2 < 2.0 \times 10^{-4}$
GC4 & LC	67	515	$g/m^2 < 5.4 \times 10^{-5}$	$g/m^2 > 4.0 \times 10^{-7}$	$g/m^2 < 1.0 \times 10^{-3}$
GC4 & WC	97	635	$g/m^2 < 2.5 \times 10^{-4}$	$g/m^2 > 5.5 \times 10^{-7}$	$g/m^2 < 2.0 \times 10^{-4}$

Notes. The listed values are essentially constant for all temperatures for which the assumptions made are valid, $T/T_{\rm c} \lesssim 0.1$. For $V < c_-$, perturbation theory instead predicts the dynamical friction to quickly vanish, causing $\tau_{\rm DF}$ to become infinite. The criterion on g/m^2 due to the hydrostatic core radius, Eq. (82), is also listed. The values for g/m^2 are given in units of eV^{-4}.

which acts as an upper limit. For flows where the counterflow would normally exceed, but is limited by, the critical velocity, the superfluid instead behaves as a normal fluid. Therefore, decreasing $v_{\rm c}$ essentially causes a transition from a superfluid to a normal fluid, interpolating the dynamical friction from about the value at $T = 0$ to the value of the normal fluid, which can differ by several orders of magnitude. Numerical simulations were also used to investigate dynamical friction, confirming the general dependence of the force on the critical velocity and the mass of the perturber, which was found using linear perturbation theory. However, the linear theory failed to reproduce the shape of the superfluid-normal fluid transition for velocities smaller than the smallest sound speed, $V < c_-$.

Finally, the superfluid dynamical friction was applied to the Fornax dSph and two of its GCs. It was found that the relevant parameter space in which, among other things, perturbation theory is valid gives orbital decay times for these GCs that are much smaller than the age of the dSph, except in the region preferred in the literature (Crăciun & Harko 2020). The present work therefore suggests that there is no timing problem for Fornax GCs in the SIBEC-DM model for the values of g/m^2 obtained by Crăciun & Harko (2020) by fitting rotation curves at $T = 0$. For a finite-temperature SIBEC-DM, on the other hand, for which the preferred parameter space of g/m^2 is likely lowered, very large decay rates of Fornax GCs pose a problem.

The use of linear perturbation theory made it possible to probe a large region of parameter space that is difficult to explore with numerical simulations. The main limitations of the numerical scheme used in this work are the low order of the Godunov scheme used; the absence of entropy production, both when the critical velocity was enforced and in shock waves, which leads to the total energy not being strictly conserved; and the large difference between the superfluid sound speeds and dynamics, which results in very small time-stepping and hence excessive diffusion of the numerical solution. All of these limit the parameters for which we can be confident that the numerical solution is correct, and therefore limits the range within which perturbation theory can be tested. Ideally, superfluid dynamical friction would have also been explored using simulations with realistic models for both the DM halo and perturber, as has been done for galaxies with standard CDM and gas (Chapon et al. 2013; Tamfal et al. 2020), but such a study requires an improved scheme for solving the superfluid hydrodynamics equations.

Acknowledgements. We thank the Research Council of Norway for their support, and Benjamin Elder for the discussions that initiated this work. We also thank the anonymous referee for their helpful comments and suggestions that greatly improved this manuscript.

References

Aceves, H., & Colosimo, M. 2007, Am. J. Phys., 75, 139
Andersen, J. O. 2004, Rev. Mod. Phys., 76, 599
Antonini, F., & Merritt, D. 2011, ApJ, 745, 83
Arca-Sedda, M., & Capuzzo-Dolcetta, R. 2017, MNRAS, 464, 3060
Bar-Or, B., Fouvry, J.-B., & Tremaine, S. 2019, ApJ, 871, 28
Barausse, E. 2007, MNRAS, 382, 826
Barenghi, C. F., Skrbek, L., & Sreenivasan, K. R. 2014, Proc. Natl. Acad. Sci., 111, 4647
Battaglia, G., Helmi, A., & Breddels, M. 2013, New Astron. Rev., 57, 52
Berezhiani, L., & Khoury, J. 2015, Phys. Rev. D, 92, 103510
Berezhiani, L., Elder, B., & Khoury, J. 2019, JCAP, 2019, 074
Binney, J., & Tremaine, S. 2008, Galactic Dynamics: Second Edition (Princeton: Princeton University Press)
Boldrini, P., Mohayaee, R., & Silk, J. 2019, MNRAS, 485, 2546
Boldrini, P., Miki, Y., Wagner, A. Y., et al. 2020, MNRAS, 492, 5218
Boylan-Kolchin, M., Ma, C.-P., & Quataert, E. 2008, MNRAS, 383, 93
Bullock, J. S., & Boylan-Kolchin, M. 2017, ARA&A, 55, 343
Chandrasekhar, S. 1943, ApJ, 97, 255
Chapman, S., Hoyos, C., & Oz, Y. 2014, J. High Energy Phys., 2014, 27
Chapon, D., Mayer, L., & Teyssier, R. 2013, MNRAS, 429, 3114
Clesse, S., & García-Bellido, J. 2018, Phys. Dark Univ., 22, 137
Cole, D. R., Dehnen, W., Read, J. I., & Wilkinson, M. I. 2012, MNRAS, 426, 601
Colpi, M., Mayer, L., & Governato, F. 1999, ApJ, 525, 720
Cowsik, R., Wagoner, K., Berti, E., & Sircar, A. 2009, ApJ, 699, 1389
Crăciun, M., & Harko, T. 2020, Eur. Phys. J. C, 80, 735
Darve, C., Bottura, L., Patankar, N. A., & Van Sciver, S. 2012, AIP Conf. Proc., 1434, 247
Davis, M., Efstathiou, G., Frenk, C. S., & White, S. D. M. 1985, ApJ, 292, 371
Debattista, V. P., & Sellwood, J. A. 2000, ApJ, 543, 704
del Pino, A., Hidalgo, S. L., Aparicio, A., et al. 2013, MNRAS, 433, 1505
Del Popolo, A., & Le Delliou, M. 2017, Galaxies, 5, 17
Doi, D., Shirai, Y., & Shiotsu, M. 2008, AIP Conf. Proc., 985, 648
Dosopoulou, F., & Antonini, F. 2017, ApJ, 840, 31
Elbert, O. D., Bullock, J. S., Garrison-Kimmel, S., et al. 2015, MNRAS, 453, 29
Famaey, B., & McGaugh, S. S. 2012, Liv. Rev. Relativ., 15, 10
Fujii, M., Funato, Y., & Makino, J. 2006, PASJ, 58, 743
Goerdt, T., Moore, B., Read, J. I., Stadel, J., & Zemp, M. 2006, MNRAS, 368, 1073
Goerdt, T., Moore, B., Read, J. I., & Stadel, J. 2010, ApJ, 725, 1707
Gómez, L. G., & Rueda, J. 2017, Phys. Rev. D, 96, 063001
Hague, P. R., & Wilkinson, M. I. 2013, MNRAS, 433, 2314
Harko, T., & Mocanu, G. 2012, Phys. Rev. D, 85, 084012
Harko, T., Liang, P., Liang, S.-D., & Mocanu, G. 2015, JCAP, 2015, 027
Hartman, S. T. H., Winther, H. A., & Mota, D. F. 2020, A&A, 639, A90
Harvey, D., Massey, R., Kitching, T., Taylor, A., & Tittley, E. 2015, Science, 347, 1462
Hu, W., Barkana, R., & Gruzinov, A. 2000, Phys. Rev. Lett., 85, 1158
Hui, L., Ostriker, J. P., Tremaine, S., & Witten, E. 2017, Phys. Rev. D, 95, 043541
Jiang, C. Y., Jing, Y. P., Faltenbacher, A., Lin, W. P., & Li, C. 2008, ApJ, 675, 1095
Just, A., Khan, F. M., Berczik, P., Ernst, A., & Spurzem, R. 2011, MNRAS, 411, 653
Katz, A., Kurkela, A., & Soloviev, A. 2019, JCAP, 2019, 017
Kaur, K., & Sridhar, S. 2018, ApJ, 868, 134
Khoury, J. 2016, Phys. Rev. D, 93, 103533

Lancaster, L., Giovanetti, C., Mocz, P., et al. 2020, JCAP, 2020, 001
Landau, L. 1941, Phys. Rev., 60, 356
Lee, A. T., & Stahler, S. W. 2011, MNRAS, 416, 3177
Lee, A. T., & Stahler, S. W. 2014, A&A, 561, A84
Lelli, F., McGaugh, S. S., & Schombert, J. M. 2016, AJ, 152, 157
Leung, G. Y. C., Leaman, R., van de Ven, G., & Battaglia, G. 2020, MNRAS, 493, 320
Lovell, M. R., Frenk, C. S., Eke, V. R., et al. 2014, MNRAS, 439, 300
Mackey, A. D., & Gilmore, G. F. 2003, MNRAS, 340, 175
Madelung, E. 1926, Naturwissenschaften, 14, 1004
Meadows, N., Navarro, J. F., Santos-Santos, I., Benítez-Llambay, A., & Frenk, C. 2020, MNRAS, 491, 3336
Milgrom, M. 1983a, ApJ, 270, 384
Milgrom, M. 1983b, ApJ, 270, 365
Milgrom, M. 1983c, ApJ, 270, 371
Mina, M., Mota, D. F., & Winther, H. A. 2020a, A&A, 641, A107
Mina, M., Mota, D. F., & Winther, H. A. 2020b, ArXiv e-prints [arXiv:2007.04119]
Mocz, P., Vogelsberger, M., Robles, V. H., et al. 2017, MNRAS, 471, 4559
Mulder, W. A. 1983, A&A, 117, 9
Navez, P., & Graham, R. 2006, Phys. Rev. A, 73, 043612
Nori, M., & Baldi, M. 2018, MNRAS, 478, 3935
Nori, M., & Baldi, M. 2021, MNRAS, 501, 1539
Oh, K. S., Lin, D. N. C., & Richer, H. B. 2000, ApJ, 531, 727
Ostriker, E. C. 1999, ApJ, 513, 252
Pani, P. 2015, Phys. Rev. D, 92, 123530
Percival, W. J., Baugh, C. M., Bland-Hawthorn, J., et al. 2001, MNRAS, 327, 1297
Pitaevskii, L. P., & Stringari, S. 2016, Bose-Einstein Condensation and Superfluidity (Oxford: Oxford University Press)
Planck Collaboration XIII. 2016, A&A, 594, A13
Pontzen, A., & Governato, F. 2012, MNRAS, 421, 3464
Read, J. I., Walker, M. G., & Steger, P. 2019, MNRAS, 484, 1401
Riess, A. G., Macri, L. M., Hoffmann, S. L., et al. 2016, ApJ, 826, 56
Sales, L. V., Navarro, J. F., Oman, K., et al. 2016, MNRAS, 464, 2419
Sánchez-Salcedo, F. J. 2012, ApJ, 745, 135
Sánchez-Salcedo, F. J., & Brandenburg, A. 1999, ApJ, 522, L35
Santos-Santos, I. M., Brook, C. B., Stinson, G., et al. 2015, MNRAS, 455, 476
Sawala, T., Frenk, C. S., Fattahi, A., et al. 2016, MNRAS, 457, 1931
Schive, H.-Y., Chiueh, T., & Broadhurst, T. 2014, Nat. Phys., 10, 496
Schwabe, B., Niemeyer, J. C., & Engels, J. F. 2016, Phys. Rev. D, 94, 043513
Sellwood, J. A. 2014, Rev. Mod. Phys., 86, 1
Shadmehri, M., & Khajenabi, F. 2012, MNRAS, 424, 919
Shao, S., Gao, L., Theuns, T., & Frenk, C. S. 2013, MNRAS, 430, 2346
Sharma, A., Khoury, J., & Lubensky, T. 2019, JCAP, 2019, 054
Sikivie, P., & Yang, Q. 2009, Phys. Rev. Lett., 103, 111301
Skrbek, L. 2011, J. Phys.: Conf. Ser., 318, 012004
Skrbek, L., & Sreenivasan, K. R. 2012, Phys. Fluids, 24, 011301
Slepian, Z., & Goodman, J. 2012, MNRAS, 427, 839
Soulaine, C., Quintard, M., Baudouy, B., & Van Weelderen, R. 2017, Phys. Rev. Lett., 118, 074506
Spergel, D. N., & Steinhardt, P. J. 2000, Phys. Rev. Lett., 84, 3760
Strigari, L. E. 2018, Rep. Progr. Phys., 81, 056901
Tamfal, T., Mayer, L., Quinn, T. R., et al. 2020, ApJ, submitted [arXiv:2007.13763]
Taylor, E., & Griffin, A. 2005, Phys. Rev. A, 72, 8739
Tegmark, M., Blanton, M. R., Strauss, M. A., et al. 2004, ApJ, 606, 702
Thun, D., Kuiper, R., Schmidt, F., & Kley, W. 2016, A&A, 589, A10
Toro, E. 2006, Appl. Numer. Math., 56, 1464
Trujillo-Gomez, S., Klypin, A., Primack, J., & Romanowsky, A. J. 2011, ApJ, 742, 16
Tulin, S., & Yu, H.-B. 2018, Phys. Rep., 730, 1
Vogelsberger, M., Genel, S., Springel, V., et al. 2014, Nature, 509, 177
Walker, M. 2013, in Planets, Stars and Stellar Systems: Volume 5: Galactic Structure and Stellar Populations, eds. T. D. Oswalt, & G. Gilmore (Dordrecht: Springer), 1039
Walker, M. G., Mateo, M., Olszewski, E. W., et al. 2009, ApJ, 704, 1274
Wang, M. Y., Boer, T. D., Pieres, A., et al. 2019a, ApJ, 881, 118
Wang, M. Y., Koposov, S., Drlica-Wagner, A., et al. 2019b, ApJ, 875, L13
Weinberg, M. D. 1985, MNRAS, 213, 451
Weinberg, D. H., Bullock, J. S., Governato, F., Naray, R. K. D., & Peter, A. H. G. 2015, Proc. Natl. Acad. Sci., 112, 12249
Zhao, H. 1996, MNRAS, 278, 488
Zhu, Q., Marinacci, F., Maji, M., et al. 2016, MNRAS, 458, 1559